# Thin-Film Polar-Oxides for Heterogeneous Catalysis

Adam Martin Kerrigan

Doctor of Philosophy

University of York

Physics

January, 2021

*"God does not care about our mathematical difficulties; He integrates empirically." — Albert Einstein*

# Thin-Film Polar-Oxides for Heterogeneous Catalysis

**Adam Martin Kerrigan**

Submitted for the degree of Doctor of Philosophy in Physics
January, 2021

## Abstract

The search for green energy production is a vital part of humanity's commitment and responsibility to future generations. Heterogeneous catalysis can provide many avenues to realising this goal, from the production of environmentally benign fuel sources via photocatalytic water-splitting to increasing the performance of chemical energy production through hydrogen fuel cells. Polar-oxide films are viable candidates for use as heterogeneous catalysts. Due to the polar catastrophe, the surfaces of these oxides are highly unstable requiring geometric and electronic reconstructions to stabilise. A consequence of the geometric reconstructions is often low coordination of surface sites, making the surface more catalytically active. The focus of this thesis is the growth of polar-oxide films, their characterisation and suitability as a catalyst for the water-gas shift reaction. The successful growth of NiO (111) films via molecular beam epitaxy is shown to produce rough surfaces with a dual domain structure. Through *ex-situ* annealing, the thin film surfaces are smoothed and second domains expunged. This is verified through reflection high-energy electron diffraction and atomic force microscopy; the formation of the second domain is studied using density functional theory (DFT). The surfaces of NiO (111) and MgO (111) surfaces are shown to form $\{100\}$ facets via either the growth process or through irradiation by an electron beam in a scanning transmission electron microscope. These faceted surfaces are characterised theoretically via vibrational spectroscopy of CO molecules adsorbed at the inequivalent surface sites. NiO (111) is considered as a catalyst for the water-gas shift reaction with environmental transmission electron microscopy images revealing the surface is reduced in the presence of CO. X-ray photoelectron spectroscopy is used to confirm the surface is reduced to nickel metal. The mechanism for reduction and re-oxidation, via dissociative water adsorption, is studied using DFT and complemented by further environmental microscopy and spectra.

# CONTENTS

**Title page** **i**

**Abstract** **v**

**Table of contents** **vii**

**Acknowledgements** **xvii**

**Declaration** **xix**

**1 Introduction** **1**

1.1 Motivation . . . . . 2

1.2 Overview of Thesis . . . . . 2

1.3 Polar Surfaces . . . . . 4

1.4 Surface Reconstructions of NiO and MgO . . . . . 6

1.4.1 Octopolar Reconstruction . . . . . 7

1.4.2 Hydroxylated Surface . . . . . 9

1.4.3 Other Notable Surface Reconstructions . . . . . 9

1.5 The Water-Gas Shift Reaction . . . . . 10

**2 Experimental Techniques** **13**

2.1 Ultra-High Vacuum Systems . . . . . 14

2.1.1 Vacuum Pumps . . . . . 14

2.1.2 Molecular Beam Epitaxy . . . . . 17

2.1.3 Reflection High-Energy Electron Diffraction . . . . . 21

2.2 Electron Microscopy . . . . . 22

2.2.1 Electron Lenses . . . . . 23

2.2.2 Transmission Electron Microscopy . . . . . 24

2.2.3 Scanning Transmission Electron Microscopy . . . . . . . . . . . . 27
2.2.4 Sample Preparation . . . . . . . . . . . . . . . . . . . . . . . . . . . 29
2.3 Atomic Force Microscopy . . . . . . . . . . . . . . . . . . . . . . . . . . 32

**3 Computational Theory and Methodology 35**
3.1 Density-Functional Theory . . . . . . . . . . . . . . . . . . . . . . . . . . 36
3.1.1 The Many-body Problem . . . . . . . . . . . . . . . . . . . . . . . 36
3.1.2 Born-Oppenhiemer Approximation . . . . . . . . . . . . . . . . . 36
3.1.3 Hohenberg-Kohn Theorem . . . . . . . . . . . . . . . . . . . . . . 38
3.1.4 Kohn-Sham Density-Functional Theory . . . . . . . . . . . . . . . 39
3.1.5 Exchange-Correlation Functionals . . . . . . . . . . . . . . . . . . 41
3.1.6 Spin Channels . . . . . . . . . . . . . . . . . . . . . . . . . . . . . 42
3.1.7 Bloch's Theorem . . . . . . . . . . . . . . . . . . . . . . . . . . . . 42
3.1.8 Brillouin Zone Sampling . . . . . . . . . . . . . . . . . . . . . . . 44
3.2 Density-Functional Theory Extensions . . . . . . . . . . . . . . . . . . . 45
3.2.1 Hubbard-like Correction . . . . . . . . . . . . . . . . . . . . . . . 45
3.3 Computational Implementation of DFT . . . . . . . . . . . . . . . . . . 48
3.3.1 Plane-wave Basis . . . . . . . . . . . . . . . . . . . . . . . . . . . 48
3.3.2 Pseudo-Potentials . . . . . . . . . . . . . . . . . . . . . . . . . . . 49
3.3.3 Geometry Optimisation . . . . . . . . . . . . . . . . . . . . . . . . 50
3.3.4 Surface Calculations . . . . . . . . . . . . . . . . . . . . . . . . . 51
3.3.5 Vibrational Modes . . . . . . . . . . . . . . . . . . . . . . . . . . . 52

**4 Preparation of Polar Nickel Oxide Thin Films via Molecular Beam Epitaxy 55**
4.1 Introduction . . . . . . . . . . . . . . . . . . . . . . . . . . . . . . . . . 56
4.2 Methods . . . . . . . . . . . . . . . . . . . . . . . . . . . . . . . . . . . 56
4.2.1 Substrate Preparation . . . . . . . . . . . . . . . . . . . . . . . . . 56
4.2.2 Film Growth . . . . . . . . . . . . . . . . . . . . . . . . . . . . . . 57
4.2.3 Annealing . . . . . . . . . . . . . . . . . . . . . . . . . . . . . . . 57
4.2.4 Atomic Force Microscopy . . . . . . . . . . . . . . . . . . . . . . . 57
4.2.5 Density Functional Theory . . . . . . . . . . . . . . . . . . . . . . 58
4.3 Film Growth . . . . . . . . . . . . . . . . . . . . . . . . . . . . . . . . . 59
4.3.1 Reflection High-Energy Electron Diffraction . . . . . . . . . . . . 59
4.3.2 Density Functional Theory . . . . . . . . . . . . . . . . . . . . . . 60
4.4 Annealed Films . . . . . . . . . . . . . . . . . . . . . . . . . . . . . . . 64

- 4.4.1 Surface Structure . . . 64
- 4.4.2 Crystal Structure . . . 67
- 4.5 Conclusions . . . 70

**5 Characterisation of the (111) Surface on Polar Oxides 71**

- 5.1 Introduction . . . 72
- 5.2 Methods . . . 72
  - 5.2.1 Sample Information . . . 72
  - 5.2.2 Computational Details . . . 73
- 5.3 Transmission Electron Microscopy Evidence . . . 75
- 5.4 Surface Structures and Characterisation . . . 79
  - 5.4.1 (100) Surface . . . 79
  - 5.4.2 (111) Surface . . . 83
  - 5.4.3 Bader Charge Distribution . . . 87
  - 5.4.4 Surface Characterisation via Vibrational Spectroscopy . . . 89
- 5.5 Conclusions . . . 91

**6 NiO as a Catalyst for the Water-Gas Shift Reaction 93**

- 6.1 Introduction . . . 94
- 6.2 Methods . . . 94
  - 6.2.1 Transmission Electron Microscopy . . . 94
  - 6.2.2 XPS . . . 95
  - 6.2.3 Formation Enthalpy . . . 95
  - 6.2.4 Gibbs Free Energy . . . 96
- 6.3 Formation Enthalpy . . . 97
- 6.4 Carbon Monoxide Induced Reduction . . . 97
  - 6.4.1 Environmental TEM . . . 97
  - 6.4.2 Environmental XPS . . . 98
  - 6.4.3 Density Functional Theory . . . 100
- 6.5 Re-oxidation via Exposure to Water Vapour . . . 103
  - 6.5.1 Transmission Electron Microscopy . . . 103
  - 6.5.2 Environmental XPS . . . 103
  - 6.5.3 Density Functional Theory . . . 104
- 6.6 Water-Gas Shift Reaction . . . 107
- 6.7 Conclusions . . . 109

7 Conclusions 111
7.1 Future Work . . . . . . . . . . . . . . . . . . . . . . . . . . . . . . . . . . 113
A Bader Charge Partitioning I
B Convergence Testing V
Abbreviations IX
Bibliography XIII

# LIST OF TABLES

2.1 Vacuum Levels . . . . . . . . . . . . . . . . . . . . . . . . . . . . . 14

3.1 The available centring types for the 7 lattice system in 3D space. . . . . . 43

4.1 Interface energies for the symmetrically inequivalent stacking of the two domains. The cation mirrored structures for the mixed configurations were not calculated due to the higher energy cost in both the MgO | NiO and NiO | NiO interfaces. . . . . . . . . . . . . . . . . . . . . 62

5.1 Calculated properties of NiO using DFT+$U$. . . . . . . . . . . . . . . . . 74
5.2 Lattice Strain and Bader Charge Transfer of (100) Surfaces . . . . . . . . 79
5.3 Adsorption Energy, Bond Length and Vibrational Frequency of CO on NiO and MgO (100) surfaces . . . . . . . . . . . . . . . . . . . . . . . . 82
5.4 Surface Energy of Increasing Facet Sizes . . . . . . . . . . . . . . . . . . . 85
5.5 Bader Verification of Polar Catastrophe Healing . . . . . . . . . . . . . . . 87
5.6 Bader Charge Transfer of Sites within the Faceted (111) Surface . . . . . 88
5.7 CO Adsorption Energies and Vibrational Frequency on the Faceted (111) Surface . . . . . . . . . . . . . . . . . . . . . . . . . . . . . . . . 91

6.1 Formation Enthalpy of NiO, MgO, $CO_2$ and $H_2O$ . . . . . . . . . . . . . . . 97
6.2 Oxidation Energy of Reduced NiO Surfaces via $H_2O$. . . . . . . . . . . . 105
6.3 Comparison of the Gibbs Free Energy of the WGSR . . . . . . . . . . . . 109

# LIST OF FIGURES

1.1 Tasker Surfaces . . . . . . . . . . . . . . . . . . . . . . . . . . . . 4
1.2 Electrostatic Potential of Polar surfaces . . . . . . . . . . . . . . . . . . . 5
1.3 Unit Cell of Rock-Salt Structure . . . . . . . . . . . . . . . . . . . . . . 7
1.4 Octopolar Reconstruction . . . . . . . . . . . . . . . . . . . . . . . . 8
1.5 OH Termination . . . . . . . . . . . . . . . . . . . . . . . . . . . . 9
1.6 Equilibrium Constant for the Water-Gas Shift Reaction . . . . . . . . . . 11

2.1 Rotary Pump Diagram . . . . . . . . . . . . . . . . . . . . . . . . . 15
2.2 Turbomolecular Pump Diagram . . . . . . . . . . . . . . . . . . . . . 16
2.3 MBE Chamber . . . . . . . . . . . . . . . . . . . . . . . . . . . . . 18
2.4 TEM Lens and Aperture Schematic Diagram . . . . . . . . . . . . . . . . 25
2.5 TEM Operational Mode Schematics . . . . . . . . . . . . . . . . . . . . 27
2.6 TEM Lens and Aperture Schematic Diagram . . . . . . . . . . . . . . . . 28
2.7 Cross-Sectional Sample Preparation . . . . . . . . . . . . . . . . . . . . 30
2.8 Diagram of PIPS Operation . . . . . . . . . . . . . . . . . . . . . . . 31
2.9 PIPS Coloured Fringes . . . . . . . . . . . . . . . . . . . . . . . . . 32

3.1 Projected $d$-orbitals surrounding a Ni atom from a VASP calculation on bulk NiO. The left image shows the orbitals from a standard DFT calculation whilst the right is a DFT+$U$ calculation with a $U_{eff}$ of 5.3 eV. Both images are produced using the same isosurface value for the charge density. . . . . . . . . . . . . . . . . . . . . . . . . . . . . . . . 46
3.2 Weighted Bader Charge Partitioning . . . . . . . . . . . . . . . . . . . 47
3.3 Surface Slab Model . . . . . . . . . . . . . . . . . . . . . . . . . . . 51

4.1 Reflection High-Energy Electron Diffraction pre-anneal . . . . . . . . . . 59

4.2 Reflection High-Energy Electron Diffraction multiple domains . . . . . . 60
4.3 Interface Structures . . . . . . . . . . . . . . . . . . . . . . . . . . . . 61
4.4 Interface Spin . . . . . . . . . . . . . . . . . . . . . . . . . . . . . . . 63
4.5 HAADF mixed NiO/MgO interface . . . . . . . . . . . . . . . . . . . . 64
4.6 Reflection High-Energy Electron Diffraction annealing series . . . . . . . 65
4.7 Atomic Force Microscopy images of the annealing series . . . . . . . . . 66
4.8 Environmental Transmission Electron Microscope image of grain evolution . . . . . . . . . . . . . . . . . . . . . . . . . . . . . . . . . . . 67
4.9 Moiré pattern from grain overlap . . . . . . . . . . . . . . . . . . . . . 68
4.10 Bright-Field and High-Angle Annular Dark-Field Scanning Transmission Electron Microscopy Images of NiO (111) . . . . . . . . . . . . . . 69

5.1 MgO Pyramidal Growth . . . . . . . . . . . . . . . . . . . . . . . . . . 75
5.2 NiO Pyramidal Growth . . . . . . . . . . . . . . . . . . . . . . . . . . 76
5.3 RHEED of NiO (111) | MgO (111) . . . . . . . . . . . . . . . . . . . . 77
5.4 NiO (111) Before and After Interaction with Electron Beam . . . . . . . . 78
5.5 NiO (111) Beam Induced Pyramids . . . . . . . . . . . . . . . . . . . . . 78
5.6 (100) Surface PDOS . . . . . . . . . . . . . . . . . . . . . . . . . . . . 80
5.7 NiO (100) Orbital PDOS . . . . . . . . . . . . . . . . . . . . . . . . . 81
5.8 (100) CO Adsorption Diagram . . . . . . . . . . . . . . . . . . . . . . . 81
5.9 (111) Faceted Surface Simulation Cell . . . . . . . . . . . . . . . . . . . 84
5.10 Surface Energy With Respect To $H_2O$ Chemical Potential . . . . . . . . . 85
5.11 (111) Surface Groups . . . . . . . . . . . . . . . . . . . . . . . . . . . 86
5.12 (111) Facet Relaxed Saddle Point Geometry . . . . . . . . . . . . . . . . 88
5.13 (111) CO Adsorption Geometries . . . . . . . . . . . . . . . . . . . . . 89
5.14 (111) CO Adsorption Energies . . . . . . . . . . . . . . . . . . . . . . . 90

6.1 TEM Evolution of NiO (111) in CO . . . . . . . . . . . . . . . . . . . . 98
6.2 XPS Temperature Evolution of NiO (111) in CO . . . . . . . . . . . . . . 99
6.3 XPS Time Evolution of NiO (111) in CO . . . . . . . . . . . . . . . . . 100
6.4 Oxygen Vacancy NiO (100) . . . . . . . . . . . . . . . . . . . . . . . . 101
6.5 Oxygen Vacancies on faceted NiO (111) . . . . . . . . . . . . . . . . . . 102
6.6 re-crystallisation of NiO (111) in $H_2O$ . . . . . . . . . . . . . . . . . . 104
6.7 XPS Temperature Evolution of NiO (111) in $H_2O$ . . . . . . . . . . . . . 105
6.8 $H_2O$ Re-oxidation of Reduced NiO (111) . . . . . . . . . . . . . . . . . 106

6.9 TEM Evolution of NiO (111) in CO and $H_2O$ . . . . . . . . . . . . . . . . . . 108

B.1 Energy Convergence with respect to planewaves. The dotted grey line represents 3 meV energy difference to the last value. Both NiO and MgO are below this value after 450 eV planewave cut-off. . . . . . . . . . VI

B.2 Energy Convergence with respect to k-point spacing. The dotted grey lines represents 3 meV and -3 meV energy difference to the last value. Both NiO and MgO are between this value after a k-point spacing of 0.05 $1/\text{Å}^3$. . . . . . . . . . . . . . . . . . . . . . . . . . . . . . . . . . . . VI

B.3 Energy Convergence with respect to vacuum gap for the (111) surface of MgO and an isolated $H_2O$ molecule. $H_2O$ is plotted against the right hand y-axis whilst the (111) surface is plotted against the left. The scale and relative position of them both are the same. . . . . . . . . . . . . . . . VII

# ACKNOWLEDGEMENTS

### Formal acknowledgements

I would like to thank both my supervisors, Prof. Keith McKenna and Prof. Vlado Lazarov, for their support and guidance during the time I have spent working on this project. The insight you have both offered has been invaluable. I would like to also thank the many members of both groups that have been a help during my time at York. The discussions we have had have been of a great help to me for both my work and sanity during the four years.

### Informal acknowledgements

From the groups in which I have worked I would like to single out Dr. Barat Achinuq for his incredible patience when teaching me how to operate the many new instruments during the first years of my PhD study, your kindness was extremely appreciated and your enthusiasm was inspiring. I would also like to thank Dr. Razak Elmaslmane and Mr. James Quirk for the many times you either answered one of my numerous stupid questions or asked one yourself that helped me feel like I might not be the least intelligent person in the room after all. Whilst, like family, the choice of fellow group members is often beyond your own control I could not have asked for two better friends. Outside of the department I consider myself very fortunate to have a family that supports and cares for me. I'd like to thank my grandparents for their unwavering pride in me, your belief often spurred me on and I am incredibly grateful. My parents, for the immeasurable times you have put me before yourselves and I will forever be indebted and cannot thank you both enough. To my sister, it must be hard being the second favourite child when without doubt you are the far better person. I could not have finished this without all of your help and I love dearly. Finally I'd like to thank my partner and best friend, I know these years have been hard and frustrating for you, especially as I morphed into a nocturnal husk during the final stretch of my write up. I have not taken for granted all the sacrifices you have made and support you have offered and I am eternally grateful. I love you and look forward to repaying your kindness and generosity in the many years to come.

# DECLARATION

I declare that the work presented in this thesis is based on research carried out in the Department of Physics, University of York, England. No part of this thesis has been submitted elsewhere for any other degree or qualification and it is all my own work unless the contrary is stated in the text. All sources are acknowledged as References.

## CHAPTER 1

# INTRODUCTION

The motivation for this thesis and the structure therein are presented in this chapter. With political and social pressures driving the pursuit of advanced technologies of energy production, alongside the pursuit of knowledge, heterogeneous catalysis is again at the forefront of research for reactions like water-splitting and the water-gas shift reaction. A brief introduction to polarity in crystals and how this can drive catalytic activity is discussed along with the surface structure of model polar-oxide systems, NiO and MgO. The link between the surface reconstructions, present in the literature, and the polarity of the film is highlighted and the doubts over the true reconstructions considered. Finally, a brief introduction to the water-gas shift reaction is presented.

## 1.1 Motivation

With government commitments to carbon neutrality and the time in which action can meaningfully reduce the effects of climate change drawing ever closer, the need for renewable resources is pressing. The solution to these problems is multi-faceted, as the pursuit of advanced technologies should not focus entirely on a single environmentally benign source of energy but instead the most suitable technology for the application. An important factor of several of these advanced technologies, such as water-splitting for release of stored hydrogen or carbon monoxide oxidation for reducing contaminants within hydrogen fuel cells, is metal-oxide heterogeneous catalysts.

It is well established that the imperfect surface is often more catalytic than clean surface cleaves.[1–3] As such, a subclass of metal-oxide surfaces, polar-oxide surfaces, are prime candidates for use in heterogeneous catalysis. These surfaces have a classically divergent surface potential, with respect to film thickness, that can create low coordinated surface sites in an attempt to redistribute the charge density at the surface of the material.

NiO and MgO are two such materials that are often used as prototypical systems by which to study polar-oxide surfaces. As rock-salt structures the (111) surface of NiO and MgO is polar, whilst the relative stability of the (100) surface causes MgO (111) surfaces to reconstruct exposing {100} facets.[4] Due to the lower formation enthalpy of NiO, it is proposed that the under coordinated sites exposed, if the surface reconstructs similarly to MgO, will produce a more active surface for Reduction-Oxidation (redox) reactions. A further advantage of polar-oxides, such as NiO and MgO, are their relatively cheap constituent cost and lack of toxic or rare-earth elements. This is particularly useful as a catalyst for the Water-Gas Shift Reaction (WGSR) where current catalysts are either unsafe for consumer application or require rare-earth materials, such as cerium, to operate with enough activity at low temperatures.

## 1.2 Overview of Thesis

This thesis contains seven chapters. Chapter 1, the current chapter, provides a brief introduction to the field of polar-oxides and their applications in heterogeneous catalysis as well as the motivations behind the work presented in the thesis. The divergent electric field causing high instability at polar surfaces of these materials will be explained and stabilisation mechanisms discussed. One such passivation, the geometric reconstruction of the surface, will be used to explain how these polar surfaces are able to produce more catalytically active sites on the surface due to their lower atomic coordination. The history of these reconstructions will be discussed with respect to two prototypical materials, MgO and NiO. Finally, the WGSR will be discussed and the different mechanisms for catalysing the reaction, alongside the impact of temperature, will be presented.

Chapters 2 & 3 explain the methods, both experimental and theoretical, used for the collection of data presented in this thesis work. Chapter 2 focuses on the experimental techniques I have personally employed within the thesis, from sample growth to characterisational analysis. It discusses the theory behind the methods and provides information on how they are to be used throughout the thesis. Chapter 3 contains the theory behind the theoretical calculations performed, as well as discussion of scientific code written as part of the thesis.

Chapter 4 presents NiO thin film growth via Molecular Beam Epitaxy (MBE) and the study of their surfaces. The films were subjected to *ex-situ* annealing in an open atmosphere and the effects of the post-growth treatment on surface sharpness and crystallinity of the sample are studied. Density-Functional Theory (DFT) is used to explore the formation of twin-boundaries, along (111) planes in the sample, that lead to the production of two competing electron diffraction patterns visible in Reflection High-Energy Electron Diffraction (RHEED) images of the surface.

In Chapter 5 the surface structure of NiO and MgO films are explored and different methods for the production of large scale faceted reconstructions examined. This reconstruction is confirmed by Transmission Electron Microscope (TEM) and Scanning Transmission Electron Microscope (STEM) images of NiO and MgO films. The formation of the reconstruction is considered within a DFT framework and compared to other, theoretically, low energy surface terminations. The surface and its two terminations for both NiO and MgO are then characterised using vibrational analysis of an adsorbed CO molecule and compared to, the much more stable, (100) surface as well as the $p(2 \times 2)$ octopolar surface.

In Chapter 6 the viability of the (111) surface of NiO is assessed for use as a redox catalyst in the WGSR. The two separate reactions, CO induced reduction of the surface and $H_2O$ re-oxidation, are studied in an environmental STEM where the effects of each on the surface of the NiO (111) film are clearly visible. This structural evidence is supported by X-ray photoelectron spectroscopy (XPS) of NiO (111) undergoing the same reactions as in the STEM. The energetics of the redox reactions are studied using DFT and compared to the (100) surface which is considered to be a less active catalyst. A pathway for re-oxidation using $H_2O$ is considered for both surfaces exploring the effect of dissociative adsorption of the water molecule.

Finally, in Chapter 7 the thesis is summarised and conclusions from the work presented are drawn. Potential future work and how the outcomes of the thesis can be used as a platform for new investigations are also explored.

Two appendices are included, Appendix A & B, which show code snippets from software developed through the thesis as well as commentary on sections of the code and convergence graphs respectively.

## 1.3 Polar Surfaces

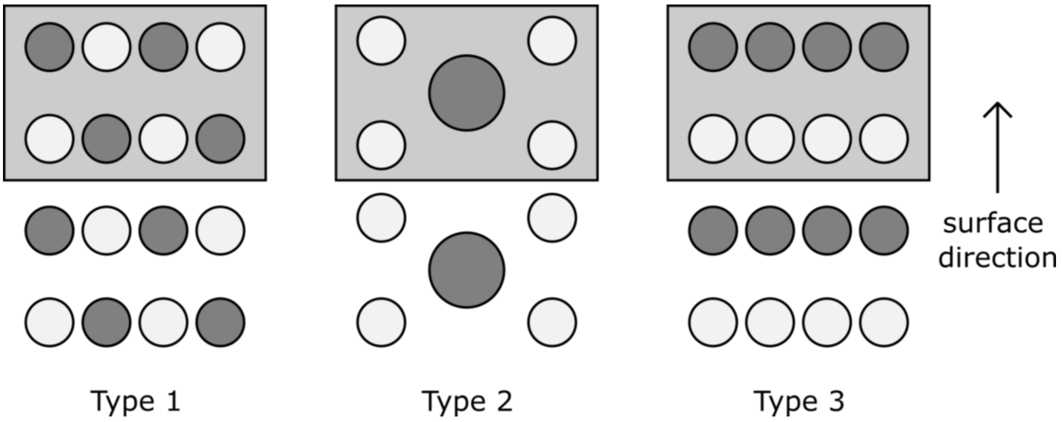

**Figure 1.1:** The three types of Tasker surface.[5] The darker circles represent cations and the lighter circles are anions, whilst the grey box highlights the repeating unit for the surface. In type 1 it is clear that the repeat unit is uncharged with no dipole moment. The type 2 surface has a non zero charge associated with each atomic plane yet, like the type 1 surface, no overall dipole moment. Finally the type 3 surface also has a non zero charge associated with each layer however in this case the repeating unit does contain a dipole.

The stability of compound crystal surfaces, identified by the Miller index[6] of the exposed crystallographic plane, can be assessed by the properties of the collection of layers that form a repeatable unit. Different forms of this unit were characterised by Tasker, in 1979,[5] into three types of surfaces. These unitary collections of planes are shown in Fig.1.1. The three surfaces considered two properties of the material within the unit cell of the surface; the charge and the dipole moment. A type 1 surface has zero net charge within the atomic planes that make up the unit cell and consequently no dipole moment. The second surface type is arranged such that the atomic planes carry a net charge but the dipole moment remains zero. This leaves a third surface, the polar surface, which has both a net charge within its atomic planes and a dipole moment. Thus, with increasing layers added to the structure, the dipole moment increases leading to a divergent potential surface energy. This infinite surface potential is known as the polar instability or, more strongly as the polar catastrophe.

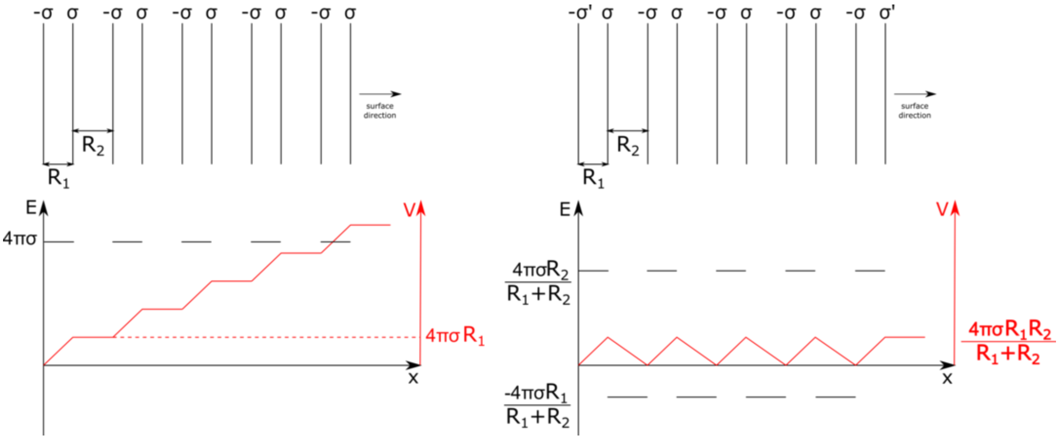

**Figure 1.2:** The energy and potential for Tasker type 3 materials as a function of position. The left-hand figure shows a diverging potential as more bi-layers are added to the system, with the material represented as planes of charge density $\pm\sigma$ separated by distances of $R_1$ and $R_2$ above the figure. The right-hand figure shows the potential of a charge modified Tasker 3 surface and how this can stabilise the divergent potential. Again a schematic of the system is shown as planes of charge density above the figure.

An example of the effect of stacking alternately charged atomic planes is given in 1.2a. Here the material is shown schematically as opposed charge density planes of equal magnitude, $\sigma$. The planes are separated by distances of $R_1$ and $R_2$ and are stacked in the direction of the polar surface. Considering the atomic layers as infinite, charged planes it is trivial to show that each bi-layer in the structure increments the potential, V, by

$$\delta V = \frac{\sigma R_1}{\epsilon_0} \tag{1.1}$$

where $\epsilon_0$ is the permittivity of free space. For a film of N bi-layers this leads to an electrostatic energy of

$$E_{\text{static}} = \frac{N R_1 \sigma^2}{\epsilon_0} \tag{1.2}$$

and total dipole moment

$$M = N R_1 \sigma \tag{1.3}$$

For ionic materials like both NiO and MgO these values are incredibly high for even just a few bi-layers.[1]

As shown polar surfaces are inherently unstable yet, displayed via schematic representation in Fig. 1.2b, surface charge modifications can be employed to counter this instability. For the model system shown the modified charge density is

$$\sigma' = \frac{\sigma R_2}{R_1 + R_2} \tag{1.4}$$

Using this modified charge density the total dipole moment is now independent of the number of bi-layers

$$M = \frac{\sigma R_1 R_2}{R_1 + R_2}. \tag{1.5}$$

Moreover, the potential of the surface no longer tends to infinity as the number of bi-layers increases. The expression for calculating the charge modification required to stabilise the polar catastrophe states that for $m$ modified surfaces layers

$$\sum_{j=1}^{m} \sigma_j = \frac{\sigma_{m+1}}{2} \left( (-1)^{m+1} - \frac{R_1 - R_2}{R_1 + R_2} \right). \tag{1.6}$$

For NiO and MgO, where the inter-planar spacings $R_1$ & $R_2$ are equal, this simplifies to

$$\sum_{j=1}^{m} \sigma_j = \frac{\sigma_{m+1}}{2} \cdot (-1)^{m+1}. \tag{1.7}$$

There are many methods of achieving the charge density modification and stabilising the surface. The most common being a surface reconstruction, in which the outer layers have differing stoichiometry to the bulk of the material, and adsorbates such as hydrogen or hydroxyls that provide charge compensation.

The necessity for healing mechanisms for polar surfaces is why they are of so much interest the catalyst community.[2,7] The geometric reconstruction required to satisfy Eqn. 1.6 leads to lower coordinated sites being exposed as active sites for heterogeneous catalysis. These provide more interactive electronic configurations for adsorbed molecules and even more accessible material for redox reactions.

## 1.4 Surface Reconstructions of NiO and MgO

Both NiO and MgO are metal-oxides that have a rock-salt structure and crystallise in the cubic $Fm\bar{3}m$ space-group. Their structure consists of two face-centred cubic lattices, one for each ion, offset from each other by half a lattice constant along a basis direction. The unit cell for each material consists of eight atoms evenly split between metal and oxygen. $Ni^{2+}$ and $Mg^{2+}$ ions are coordinated with six $O^{2-}$ forming octahedra joined along edges and at vertices. The unit cell for both structures is shown in Fig. 1.3. MgO is a non-magnetic material with a lattice constant of 4.242Å and a high formation enthalpy of -602kJ/mol. NiO is a magnetic material with anti-ferromagnetic ordering across the (111) planes of the compound, where each Ni atom has a magnetic moment of $\pm 1.69\mu_B$. It has a lattice constant of 4.175Å and, in comparison to MgO, a lower formation enthalpy of -244kJ/mol.

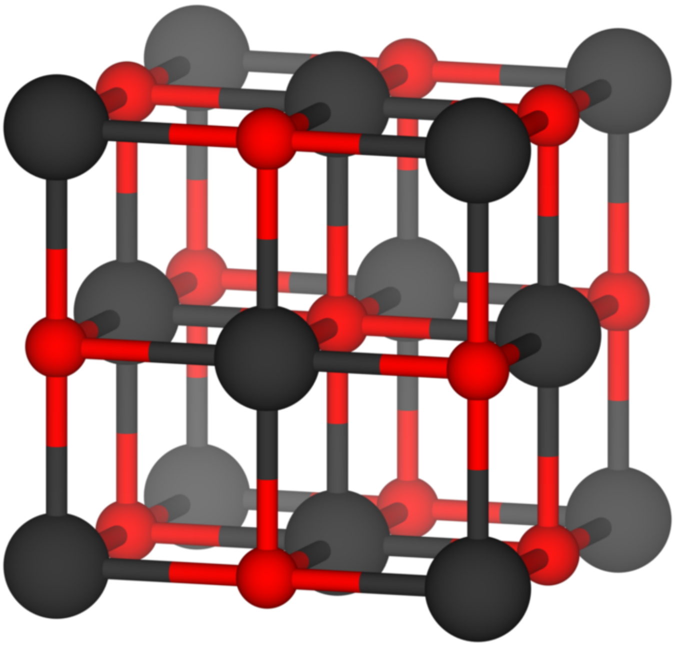

**Figure 1.3:** The unit cell of the $Fm\bar{3}m$ space-group. The cation is represented in black whilst oxygen is red. For NiO and MgO the lattice constants are 4.175Å and 4.242Å respectively.

Both materials are categorised as type-3 Tasker materials[5] in the (111) direction as each {222} plane contains alternating atomic species. This leads to highly unstable (111) surfaces due to the previously discussed polar catastrophe.

### 1.4.1 Octopolar Reconstruction

The most common termination, studied and reported, for the polar (111) surface in NiO and MgO is the $p(2 \times 2)$ octopolar reconstruction. Originally a theoretical prediction by Wolf,[8] as a potential reconstruction that could stabilise the polar catastrophe, the surface has been shown repeatedly to be the lowest energy surface reconstruction across multiple levels of theory.[9,10] The reconstruction, shown for the oxygen termination in Fig. 1.4, consists of removing 3/4 of the atoms in the first surface layer and

1/4 from the second surface layer. From a purely electrostatic standpoint, it is clear how the octopolar reconstruction stabilises the polar catastrophe with the sum of the two layers involved in the reconstructions giving

$$\frac{\sigma}{4} + \frac{-3\sigma}{4} = \frac{-\sigma}{2} \tag{1.8}$$

which satisfies Eqn. 1.7.

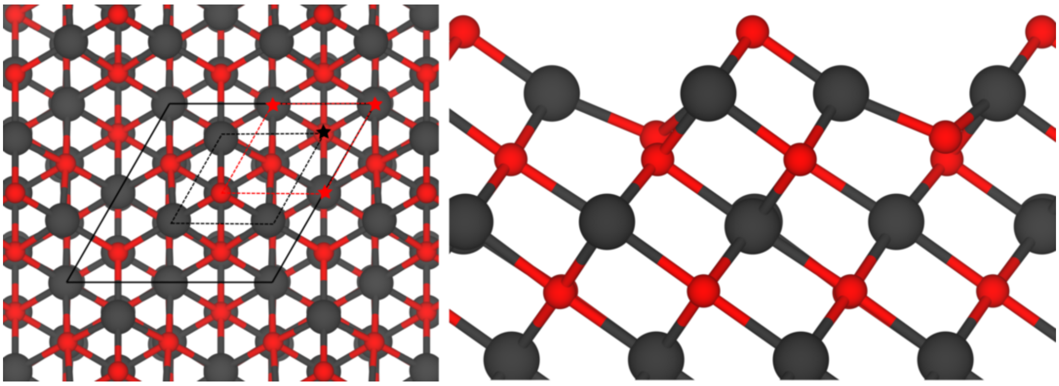

**Figure 1.4:** The octopolar reconstruction for the (111) surface of rock-salt structured metal-oxides. Here oxygen is shown in red whilst the cation is shown in black. The image on the left shows the reconstruction from above with the p(2×2) cell shown in a solid black line. The dashed lines show the primitive cell on the surface layer of the ion they are colour coded with, at the point where an atom has been removed a star is shown. The right-hand image is the reconstruction viewed down the $[1\bar{1}0]$ lattice direction and shows the characteristic saw-tooth pattern of the reconstruction.

Common methods of preparation of the octopolar reconstruction are oxidation and reduction. For NiO oxidation methods often expose Ni metal to an oxidising atmosphere until NiO is formed. As the oxygen terminated, lower energy termination, octopolar reconstruction is oxygen-deficient, thus the kinetic path to forming this reconstruction is available. Another method for producing films displaying a $p(2 \times 2)$ reconstruction attributed to the octopolar surface is to heat a $p(1 \times 1)$ OH terminated sample until it transforms at 400K. The desorption of the hydroxyls provides an environmental change sufficient for the surface to reconstruct into a $p(2 \times 2)$ ordered reconstruction, often characterised as the octopolar reconstruction. However, as these surfaces are often characterised simply by the periodicity of the surface rather than by direct measurement of atomic position, there is some doubt over the validity of assigning this $p(2 \times 2)$ reconstruction to the octopolar reconstruction in both MgO and NiO.[9,11] Moreover, the surface termination in NiO is controversial as samples said to be an oxygen terminated octopolar surface have also been classified as a nickel terminated vacancy structure, from the exact same data.

### 1.4.2 Hydroxylated Surface

Another common, in the literature, termination of the (111) surface for NiO and MgO is an OH terminated surface. This surface again can be shown to stabilise the polar catastrophe by considering a simple electrostatic picture as the outer OH layer carries half the charge of the oxygen planes in the bulk. There has been much work on the study and growth of these hydroxylated surfaces.[12–16] As the bulk terminated surface is so unstable, due to its polar nature, the OH terminated surface is often referred to as the $p(1 \times 1)$ reconstruction.

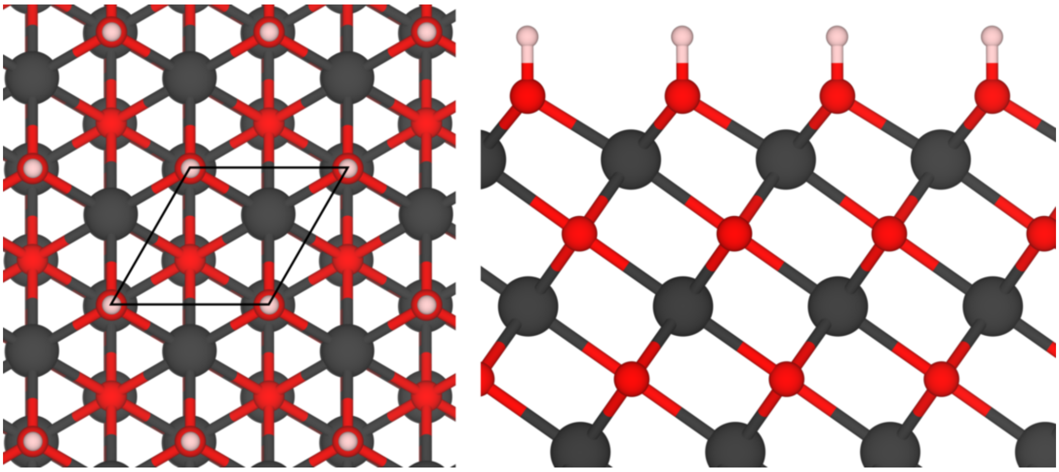

**Figure 1.5:** An OH terminated (111) surface of rock-salt structured metal-oxides. Here oxygen is shown in red and hydrogen in pink whilst the cation is shown in black. The image on the left shows the reconstruction from above with the $p(1\times1)$ cell shown in a solid black line. The right-hand image is the reconstruction viewed down the $[1\bar{1}0]$ lattice direction.

The formation of this surface has been proposed to grow from OH terminated substrates. As individual layers of atomic species are deposited the hydrogen atom continuously re-positions itself above the current top layer.[17] This means hydrogen can be introduced at the start of the growth and doesn't need to be supplied for the duration.

### 1.4.3 Other Notable Surface Reconstructions

Other surfaces mentioned in the literature include a $\left(\sqrt{3} \times \sqrt{3}\right)$R30° whereby 1/3 of the oxygen from the outer layer is removed and an OH molecule replaces another 1/3. At chemical potentials of $H_2O$ at which this surface termination is more favourable than OH termination it has been shown that the octopolar surface is still much more favourable than the $\left(\sqrt{3} \times \sqrt{3}\right)$R30° reconstructed surface.

$\{100\}$ facets formed on the (111) surface of NiO and MgO have been previously reported in the literature.[18–20] However, for MgO, these were shown to be not {100} facets but actually {110} facets caused by acid etching.[21]

Recently a bulk terminated surface for NiO was reported along with a subsurface tetrahedral reconstruction.[10] Strangely these results are reported with no formation energies for the DFT calculations performed or information on how the sample was grown. However, as these have both been studied before and found to be high energy surfaces it can be surmised that these are not untreated samples.[15]

## 1.5 The Water-Gas Shift Reaction

The WGSR is an exothermic, reversible, reaction converting carbon monoxide and water vapour into carbon dioxide and hydrogen gas.

$$\mathrm{CO}\ (\mathrm{g}) + \mathrm{H_2O}\ (\mathrm{g}) \rightleftharpoons \mathrm{CO_2}\ (\mathrm{g}) + \mathrm{H_2}\ (\mathrm{g}) \tag{1.9}$$

First discovered in 1780 by Italian physicist Felice Fontana the importance of the reaction wasn't appreciated until much later when the production of hydrogen for ammonia became more important.[22] Due to its ability to not only produce hydrogen but also oxidise carbon monoxide, cleaning toxic exhausts, the WGSR has managed to stay relevant in industrial application. More recently, as the demand for more sustainable energy production rises the WGSR is being studied for use in increasing hydrogen yield and lowering poisonous carbon monoxide levels in Proton-Exchange Membrane (PEM) hydrogen fuel cells.[23]

The reaction has a free enthalpy of -41.2kJ/mol at standard pressure and room temperature. Using *JANAF* thermochemistry tables[24] it can be shown that as the temperature increases the Gibbs free energy also increases, by considering the change in enthalpy and entropy of the reactants and products, with the reaction becoming endothermic around 1100K. The equilibrium constant, defined as the ratio between partial pressures of the reactants and products, is dependant upon the Gibbs free energy change

$$K = \frac{p_{\mathrm{CO_2}} p_{\mathrm{H_2}}}{p_{\mathrm{CO}} p_{\mathrm{H_2O}}} \tag{1.10}$$

$$K = \exp\left(\frac{-\Delta G}{RT}\right). \tag{1.11}$$

Where $p_{\mathrm{X}}$ is the partial pressure of molecule X, $R$ is the gas constant, T is the tempera-

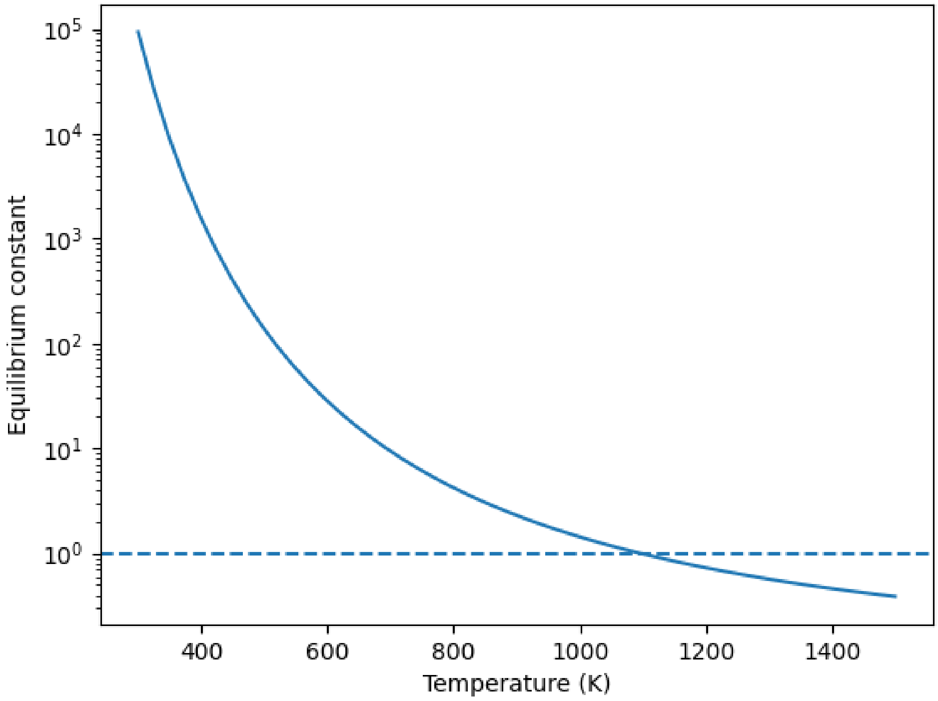

**Figure 1.6:** The equilibrium constant for the WGSR plotted as a function of temperature. The point at which the reaction is no longer energetically favourable, $\Delta G = 0$, is shown when the constant is equal to 1, at roughly 1100K. This is also the temperature at which the Gibbs free energy reverses its sign, becoming an endothermic reaction.

ture and $\Delta G$ is the Gibbs free energy. This limits the rate of the reaction as temperature increases, as seen when the equilibrium constant is plotted as a function of in Fig. 1.6. This shows that for better performance in oxidising CO and producing $H_2$ the WGSR should be operated at low temperatures.

Despite this current implementations of the WGSR often perform two shifts, first at high temperature and then again at a lower temperature, operating in the energy ranges 650K-900K and 450K-600K respectively. Metal-oxides, mainly $Fe_2O_3$, are often used as high-temperature redox catalysts due to their stability.[25] They have to be used in high temperatures due to their poor performance of oxidising CO when operating at low temperatures. This is due to the energy cost of reducing the catalyst. The low-temperature catalysts, often copper-based, promote an associative mechanism for the WGSR. However, they are less stable than their redox counterparts being susceptible to sintering which destroys the performance of the catalyst. Moreover, the catalysts are pyrophoric making them unsuitable for consumer applications. With the cost of heating and cooling between the two reactors, as well as the limitations of the catalysts for each reaction, a search for new catalyst materials is at the forefront of research in this area.[26]

One such base material is $CeO_2$, which is able to operate as a redox catalyst at 170K-900K making it an option to replace both high and low-temperature catalysts.[27,28] However, these catalysts are not just reliant on Ce but other rare-earth materials to reach adequate activity. As such the search for a catalyst for the WGSR is pressing, with criteria of low temperature stable, non-pyrophoric, non-rare-earth materials. By following the example set by ceria based catalysts and reducing the energetic cost of the CO oxidation with respect to iron-based high-temperature catalysts, a non-rare earth catalyst could operate with greater stability in the higher equilibrium constant regime. Due to the surface properties of polar-oxides, already discussed in this chapter, they have the possibility to fulfil these criteria.

# CHAPTER 2

# EXPERIMENTAL TECHNIQUES

The individual components, and how they operate, of the techniques used throughout this thesis are discussed in this chapter. Starting with molecular beam epitaxy, the generation of vacuum and preparation required to reach ultra-high vacuum is explored as well as a description of the chamber used for growth of the NiO and MgO samples in this project. The equipment attached to the chamber is also discussed, both in how it was used to grow or characterise samples and the theory behind the equipment. Following the use of vacuum generating equipment, transmission electron microscopy is considered. A basic diagram of the lenses is presented with description of the different modes of imaging for both scanning and standard transmission electron microscopes. The procedure for generating specimens for use in transmission electron microscopes is presented before a brief introduction to atomic force microscopy.

## 2.1 Ultra-High Vacuum Systems

The growth and characterisation of thin films often require low pressures, and the high mean free path afforded to atoms, x-rays and electrons by this, to ensure low contamination and high accuracy of measurements. This is done to achieve control over the quality of grown samples and produce a benign atmosphere for the propagation of electron and molecular beams without unintended interactions with the environment. Different techniques require differing levels of vacuum, defined in Table 2.1, however this thesis focuses on the Ultra High Vacuum (UHV) required for MBE, RHEED and other pressure sensitive techniques.[29]

| Vacuum Level | Pressure Range (mbar) | Mean Free Path of Air |
|---|---|---|
| Rough Vacuum | $1 \times 10^{0} - 1 \times 10^{-3}$ | 0.1mm - 100mm |
| Low Vacuum | $1 \times 10^{-3} - 1 \times 10^{-6}$ | 0.1m - 100m |
| High Vacuum | $1 \times 10^{-6} - 1 \times 10^{-9}$ | 0.1km - 100km |
| Ultra High Vacuum | $< 1 \times 10^{-9}$ | $>$ 100km |

**Table 2.1:** Classification of different vacuum levels.

As shown by Table 2.1 the pressure directly affects the mean free path of the molecule, by an inverse relation. Already at low vacuum levels the mean free path exceeds the length of the chamber, such that the only collision is either with the target or the chamber wall. For UHV conditions the mean free path is much further and it is clear how this can reduce contamination and improve sensitivity of surface techniques, like RHEED, by reducing scattering. Even with UHV conditions films will develop a monolayer of contamination from foreign substances within eight hours. Whilst this is ample time to perform growth and *in-situ* techniques at these incredibly low pressures, raising the pressure to even the lowest limit of a high vacuum system reduces this time window to less than an hour.

### 2.1.1 Vacuum Pumps

Acquiring and maintaining the low pressures of a UHV can be extremely challenging and may only be achieved through a mixture of several vacuum pumps. Types of vacuum pumps can be, for the most part, separated into two categories, gas-transfer and entrapment. Entrapment pumps function by either condensing the gas or by causing an interaction between the inner surfaces of the chamber and the gas, chemically binding the two. This often allows for the contaminant to be released back into the chamber, if required, via heating where it can then be treated by the gas-transfer pumps. Gas-transfer pumps use compression stages to permanently remove gas molecules from the chamber and deposit them in the ambient atmosphere. Both of these types of pumps have several implementations and are, more often than not, used in tandem to achieve the low pressures required for UHV conditions. Here only the pumps used throughout the span of the thesis will be explained as they are sufficient to maintain a UHV.

### Rotary Mechanical Pump

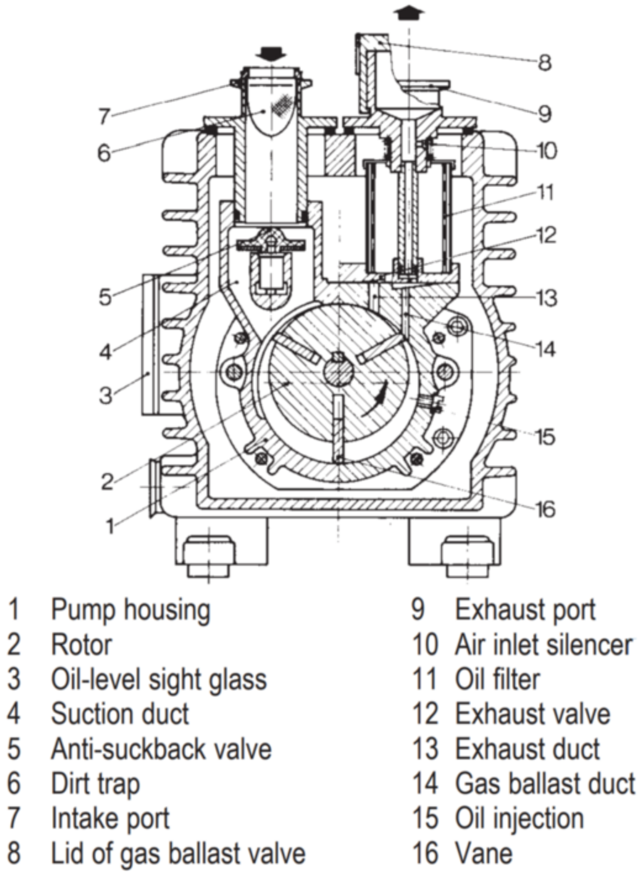

**Figure 2.1:** Diagram of the working of a rotary vane pump. Image sourced from Ref. 30. The diagram is a cross-section of the pump and the direction of flow is indicated via black arrows. It is clear as the rotor revolves gas from the intake is drawn into the vane and then compressed into the oil filter through the ballast duct.

Fig. 2.2 shows a simplified schematic for possibly the most common type of vacuum generator, the rotary mechanical pump. Rotary pumps are a form of gas-transfer pump that operate in the rough vacuum regime.[31] As the eccentrically mounted piston rotates, it draws in gas from the chamber and then isolates it from the inlet. The gas is then compressed and pushed out of the exhaust before the process is then repeated. Oil is used to seal the rotating piston and lubricate the moving components, however the oil can be a source of contamination and so oil traps are usually affixed to the pumps in an attempt to minimise this risk. The rotary pump is adept at evacuating large volumes quickly to a pressure of $1 \times 10^{-3}$mbar and is often used as the first step in a multi-vacuum system. This step is to prepare the system for pumps able to provide a more significant reduction to the pressure.

### Turbomolecular Pump

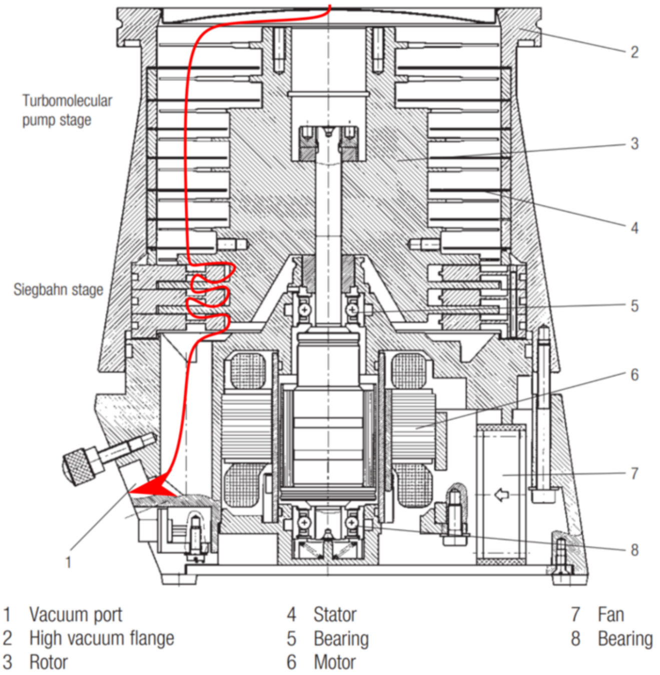

**Figure 2.2:** Diagram of the working of a turbomolecular pump. Image sourced from Ref. 30 and adapted to show the direction of flow, via a red arrow, of the pump. The diagram is a cross-section of the pump and shows the rotor, labelled 3, on which the blades are mounted and rotate about whilst deflecting molecules through the pumping stage into the Siegbahn drag stage.[32]

The turbomolecular pump is another gas-transfer pump that aims to solve the problem of oil contamination and be able to generate high vacuum pressures. Turbomolecular pumps use several rapid counter-rotating blades to impart direction to gas molecules via ballistic transport. The opposing direction of the blades prevent the gas molecules from re-entering the chamber. In the sections between each set of rotating blades the interaction of the gas and the turbines compresses the gas forcing it to follow the pressure gradient into the next section. As the blades are spinning at upwards of 30,000 revolutions per minute ambient pressures will cause frictional heating of the pump through constant interaction with the gaseous atmosphere. For this reason the pumps are only employed once the chamber has been reduced to a pressure of around $1 \times 10^{-3}$mbar, in the case of the system used in this thesis after preparation by a rotary pump. The rotary pump also provides a second function, to back up the turbo. As gas molecules progress through the different stages of the turbo they increases the pressure of the exhaust. The rotary pump acts on the exhaust keeping the pressure low enough that the partial pressure of the gas inside the chamber is equal to the partial pressure of the exhaust divided by the compression ratio, this ensures that only $H_2$ will fail to be effectively pumped.[33] Due to this high compression the contamination from the oil of the rotary pump is reduced to negligible levels. Turbomolecular pumps are able to achieve pressures of $1 \times 10^{-9}$mbar at a relatively fast rate and so make a perfect vacuum generator for systems such as a MBE.

**Titanium Sublimation Pump**

An example of an entrapment pump is the Titanium Sublimation Pump (TSP). This style of pump is used to maintain UHV conditions and provides the push to help reduce the pressure from $1 \times 10^{-9}$mbar to below $1 \times 10^{-10}$mbar. By periodically subliming Ti atoms into the chamber a thin film is formed on the surfaces inside the chamber that capture reactive gases like hydrogen, oxygen and nitrogen. The TSP is able to effectively remove gases that provide more of a challenge to the turbomolecular pump and help to speed up recovery of the vacuum post gaseous growth. TSPs are, however, a finite source pump as once the Ti source is depleted the chamber must be vented and the source replaced as such the time period of the pump cycle is often several hours. Once growth is started the TSP should be checked for its position in the cycle and potentially turned off so as not to contaminated the growth with titanium.

### 2.1.2 Molecular Beam Epitaxy

MBE is a technique for thin film growth that provides formidable levels of precision and control for substrate interfacial structure, film crystallinity and thickness. The method is however time consuming with deposition rates of single monolayers per minute. The slow growth rate is required to allow the atomic layers to grow on a layer-by-layer basis with the atoms given enough mobility and time to be able to fall into their lowest energy configuration. It is because of these slow growth times that UHV conditions are required so that the film is not contaminated. Performing this requires a combination of the previously discussed vacuum generators, chamber preparation to achieve such low pressures and chamber design to effectively transfer from ambient to UHV conditions. As well as this, fine control over the influx of the base materials is required as this must be maintained throughout the growth.

### Chamber Design

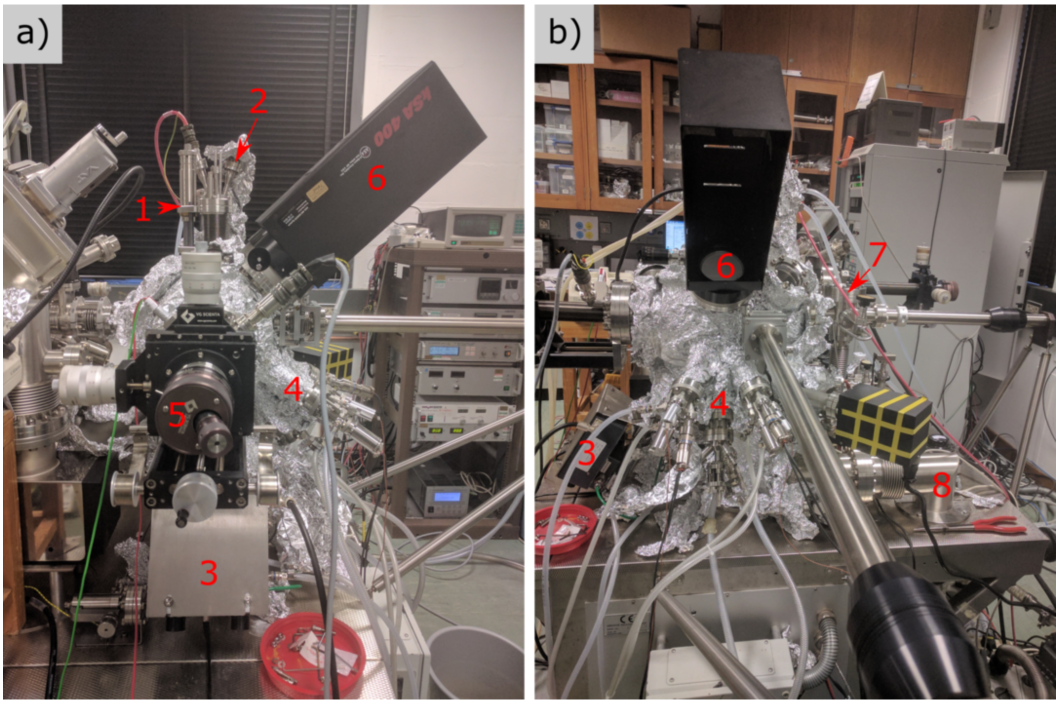

**Figure 2.3:** A front, a), and side, b), view of the MBE chamber used in the project. Specific inlets are numbered and correspond to the following: 1) quartz crystal microbalance 2) hydrogen cracker 3) oxygen plasma 4) Mg Ni and Fe (not used in this project) sources 5) stage manipulation with pass-through e-beam heating, resistive heating and thermocouple 6) RHEED screen 7) fast-entry load lock 8) right angle connector to turbomolecular pump.

The system used throughout this project, shown in Fig. 2.3, is a fourteen port stainless steel chamber equipped with a gate-valve protected Fast-Entry Load-Lock (FEL) for transfer between the ambient and the UHV conditions of the main chamber. Both the main chamber and the FEL are pumped by a rotary backed turbomolecular pump. This allows the FEL to be vented to ambient pressure independently of the main chamber and the use of a turbomolecular pump allows for rapid recovery of the vacuum to adequate levels before the gate-valve is open for sample transfer. The FEL is sealed with a rubber gasket for re-usability. All ports on the chamber, and any mounted accessories, comprise of a knife edge that bites into copper gaskets to create a tight seal. It is important that once components are removed or adjusted care is taken not to damage the knife edge and that the copper gasket is replaced. Any damage to the knife edge could compromise the base pressure of the system, likewise copper gaskets are only effective for the first use and if they were to be reused the bite from the knife edge would be compromised by the previous bite.

Measuring the pressure is done through the use of two types of vacuum gauges, Pirani and ion gauges. The use of two is required as both operate in different vacuum levels; Pirani gauges can read pressure in a rough vacuum whilst ion gauges can only operate in high vacuum and above conditions. Both gauges are considered indirect pressure gauges, meaning they are subject to uncertainty as they are calibrated for a single gas species, nitrogen. The Pirani gauge senses the heat transfer away from a resistive heated wire. The wire is supplied a precisely measured current and, after the temperature has been able to equilibrate, the resistance of the wire is measured. As the resistance of the wire is linearly proportional to the temperature, the amount of heat dissipated from the wire can be calculated. This value is directly proportional to the pressure of the surrounding environment. At pressures below the levels of the high vacuum regime, calculation of the heat transfer is impractical due to the low gas density. Instead ion gauges are used which measure the current of ionised molecules to calculate the pressure. Ions are generated via collision with produced electrons and the ion current is a measure of the gas density and as such the pressure of the system. Due to the collection of the ions the ion gauge is susceptible to oxidation and damage at high pressures.

The main chamber is also equipped with a TSP that runs for 20 minutes every four hours. This helps reduce the partial pressure of the gasses introduced to the system, oxygen, hydrogen and nitrogen, to allow for quick recovery of UHV conditions after a growth or venting of the chamber. Other than the pumps the main chamber is affixed with three gas inlets, controlled by two leak valves and one needle valve, connected to oxygen, hydrogen and nitrogen lines. The oxygen line is connected to a plasma generator that is capable of producing a 100W atomic oxygen plasma as well as allowing molecular oxygen pass through. The hydrogen line is connected to a hydrogen cracker, capable of producing atomic hydrogen for preparation of substrates for growth. The final gas line is used exclusively for venting and allows the chamber to pumped with nitrogen, this line is controlled by a needle valve rather than the leak valves which control the other two lines. A Quartz Crystal Microbalance (QCM), effusion cells and RHEED system are also equipped to the main chamber and will be explained further in upcoming sections.

### Chamber Preparation

Before the chamber can be used for growth several stages of preparation must be performed. First the chamber should be checked for leaks. This is done using a helium leak detector, first on the system with blanks affixed to each port and then one by one the blanks are replaced with the required equipment. Before being attached to the system all parts are thoroughly cleaned with acetone and IPA to reduce contamination. Whilst venting the main chamber, or FEL, nitrogen is introduced at a pressure slightly above ambient to reduce water vapour entering the system. After the main chamber has been vented the system needs to be purged of any contaminants, such as water vapour, that may have entered. To achieve this the system is baked at 140°C for two days and all equipment that produces heat, such as the effusion cells, are then outgassed by running at temperatures of 200°C. This process removes water vapour and hydrocarbons from the surfaces within the chamber allowing them to be exhausted from the system. Finally before the growth of a film the substrate is out-gassed in the FEL using a halogen lamp, this process removes water vapour and hydrocarbons from what would be the interface with the film.

### Film Growth

To deposit solid materials in the MBE chamber Langmuir-type effusion cells are used. These cells consist of a crucible in which material is heated, at temperatures to create the required vapour pressure, and escapes the cell through a large orifice. The large opening at the exit of the effusion cell allows for lower temperatures of operation in comparison to Knudsen-style cells due to the lack of aperture required to target the cell at the substrate. Effusion cells were used to provide Ni and Mg and were operated at temperatures of 1100°C and 270°C respectively, giving comparable vapour pressures between the two sources. The sources are affixed with a shutter, controllable from the exterior of the chamber, that allowed for the cells to be heated without depositing on to the substrate. A power source is coupled with a thermostat to regulate the source temperature and maintain constant flux throughout the deposition.

As well as using molecular oxygen, atomic oxygen was supplied to the chamber by the use of a 100W oxygen plasma. Although atomic oxygen is more reactive than its molecular counterpart the plasma was not used for many samples as there was no noticeable difference between films prepared either way. Generation of the plasma occurs through inductively coupled Radio Frequency (RF) excitation within an alumina crucible.[34] The plasma is contained within the crucible whilst atomic particles, due to their neutral charge, are not confined and follow the pressure gradient into the chamber. In cases where the plasma was used a lower partial pressure of atomic oxygen was used in comparison to the $5 \times 10^{-6}$mbar of molecular oxygen used when co-depositing with either Ni or Mg.

#### Quartz Crystal Microbalance

To measure the rate of deposition a QCM is lowered into the deposition position within the chamber. Knowing the properties of the material to be deposited, such as density and elastic moduli, allows for calculation of the deposition rate by monitoring the resonant frequency of the quartz crystal. As material is deposited on the QCM the properties that affect the resonate frequency, the mass, dimensions, elastic moduli and density, are all shifted. Thus the resonant frequency of the crystal is also shifted. By calculating the required material to perform the shift, and recording the time taken to achieve this shift, an accurate measurement of the deposition rate can be acquired. It is important to read the shift after the crystal has had time to equilibrate with the environment as frequency of the crystal is also temperature dependant.

### 2.1.3 Reflection High-Energy Electron Diffraction

The growth system used in this thesis used RHEED for *in-situ* characterisation of substrates and grown films. RHEED uses a grazing incident electron beam and as such is suitable for monitoring the film growth during deposition.[35–37] RHEED is incredibly sensitive to adsorbed surface impurities and scattering through a gaseous atmosphere and as such is only suited to use in MBE systems. Whilst RHEED is not considered a quantitative technique the method can provide information about the structure of film surfaces and even the underlying crystal structure.

Approximating that the electron collisions are elastic, the possible wave-vectors of the diffracted beam form a sphere, known as the Ewald sphere. The allowed diffractions are where this sphere intersects with the reciprocal lattice of the surface the beam is incident upon. For a perfectly flat surface this would lead to concentric dots however in practice, due to inelastic scattering, the pattern shown is actually vertical streaks. As the surface becomes less pristine and 3-dimensional facets are grown, the beam diffracts through the islands producing transmission diffraction spots.

## 2.2 Electron Microscopy

Electron microscopy is a widely used technique to probe the atomic structure and chemical composition of materials. The technique is fairly modern with the first device having been built only within the last 100 years in parallel, by the groups of Davison and Germer[38] as well as Thomson and Reid, only a couple of years after de Broglie's particle-wave duality was confirmed. The Abbe diffraction limit[39] shows direct proportionality between the minimum resolvable distance, $d$, and the wavelength, $\lambda$, for a system which can accept light of a range of angles described by its numerical aperture, NA

$$d = \frac{\lambda}{2\mathrm{NA}}. \tag{2.1}$$

Using this relation of wavelength and resolution the drive for higher resolution turned from visible light to smaller wavelength optics.

The de Broglie equation for the wavelength of a moving particle is given as,

$$\lambda = \frac{h}{p} \tag{2.2}$$

where $h$ is the Planck constant and $p$ is the particle's momentum.[40] Accelerating electrons through a high potential, usually 100-300keV, causes the electron to travel at over half the speed of light and as such a relativistic consideration of the momentum is required. Accounting for these relativistic effects the de Broglie equation can be rewritten in terms of $V$, the accelerating potential felt by the electron beam

$$\lambda = \frac{h}{\sqrt{2m_e eV\left(1 + \frac{eV}{2m_e c^2}\right)}}. \tag{2.3}$$

Here the mass and charge of an electron are denoted as $m_e$ and $e$ respectively whilst $c$ is the speed of light in a vacuum. It is clear to see that in order to reduce the wavelength, and consequentially increase the theoretical resolution, higher accelerating potentials should be used. Furthermore this allows for penetration through thicker samples, this is important due to transmission electron microscopy requiring sample thickness of less than 100nm — as to be electron transparent. Higher accelerating potential however leaves the sample more susceptible to beam damage, with the energy of the beam in some cases able to, at least partially, destroy the sample. This is more prevalent in biological samples and films in this thesis are considered beam resistant.

Other small wavelength particles, such as high energy x-rays, could theoretically offer improved resolution but due to the electron's inherent charge they are much easier to manipulate. This manipulation is vital to the operation of the microscope as, much like a visible-light microscope, a TEM requires the use of several lenses to focus the imagining wave.

### 2.2.1 Electron Lenses

The deflection of light caused by a lens in a visible light microscope is due to changing refractive index along the light path. This approach is mirrored in transmission electron microscopy with the use of generated magnetic fields that control the electron beam via the Lorentz force. Interacting with the beam this way has several advantages over the standard approach to light deflection as unlike in visible light microscopes the lenses do not have a fixed focal length. Adjusting the strength of the magnetic field, by adjusting the current passing through the coils generating the field, allows for the adjustment of the magnification without the need for several lenses. Magnetic lenses do, however, have many disadvantages as the strength of the magnetic field must be precisely controlled with a high level of stability for the microscope to function. Moreover the magnetic lenses suffer from the challenge of creating a magnetic field that acts consistently on all electrons, paraxial, off-axis and energy distributed alike.

As discussed the theoretical limiting factor to a microscope's resolution is the wavelength and numerical aperture, however in practical application aberrations from the lenses and astigmatisms are the cause of resolution capping in a TEM and STEM. The development of electron lenses is an area of much scientific research as the search for solutions to improve aberrational affects would drive great resolution. The three main limits of the magnetic lens are chromatic and spherical aberration along with astigmatism.

Much like chromatic aberration in optical microscopes, an electron travelling with a lower momentum will be more strongly affected by the magnetic lens and will be deflected by a larger amount compared to an electron with a higher momentum. The variation in wavelength, and momentum, within the electron beam before the sample is caused by the energy distribution of the electron source and after the sample is caused by inelastic interactions with the sample. Aberration caused by electron source can be reduced by using better electron guns with lower energy spread and also through the use of a monochromator. Whilst energy filtering of the electrons after they have passed through the sample can reduce the second cause of chromatic aberration.

Spherical aberration is caused by variation in the magnetic field as a function of distance from the central axis. The high angle electrons, far from the centre of the lens, are deflected by a greater amount than the low angle electrons. This leads to a similar problem as in the case of chromatic aberration whereby electrons are focused to different points in the microscope. Spherical aberration correction is a mixture of using apertures in an attempt to collimate the source as well as complex lens systems automatically controlled by computers. These lens systems modify the beam such that it focuses all incident angles to the same point and microscopes with this feature are able to reach sub-ångström resolution.

Astigmatism is caused by imperfections in the homogeneity of the magnetic field around the central axis of the microscope. This reduces the resolution of the image formed as the image is distorted by the non-uniformity of the field. One cause of astigmatism is the lenses themselves but charge accumulation on at the apertures due to contamination is also a source of astigmatism. Stigmator coils are used to correct the astigmatism by generating compensatory magnetic field that provides a 2-dimensional distortion to the beam that can be controlled manually.

### 2.2.2 Transmission Electron Microscopy

There are four main methods of operation for a TEM, Selected Area Electron Diffraction (SAED), High Resolution Transmission Electron Microscopy (HRTEM), Bright Field Transmission Electron Microscopy (BF-TEM) and Dark Field Transmission Electron Microscopy (DF-TEM). Each mode provides a different informative view on the sample with bright and dark field offering the isolation of scattered and unscattered electrons. A TEM consists of four main lens systems, one before the specimen and three after. The first lens, the illumination system or condenser lenses, captures and focuses the electrons emitted from the electron source, after filtration through a Wehnelt cylinder. The electrons are focused into a parallel beam and passed through the condenser aperture which helps to reduce the spherical aberration of the final image. This system is independent of the imaging mode and therefore is identical between all four modes of operation. A simplified schematic of the lens configuration and diagram of

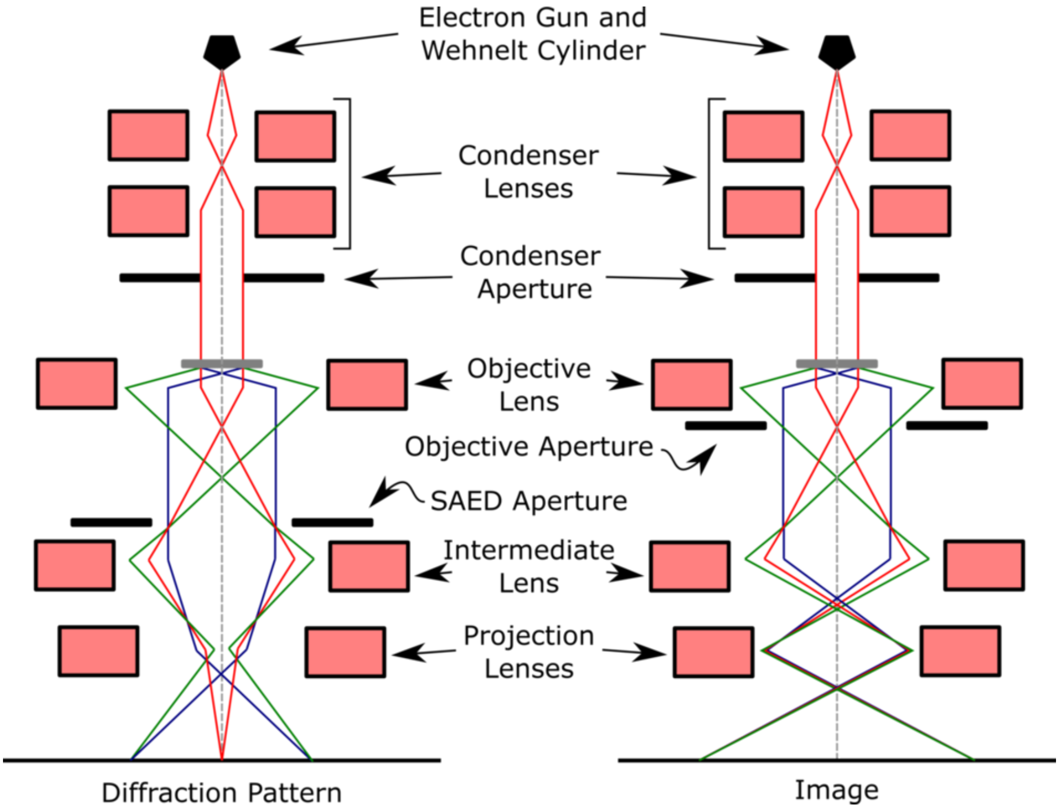

**Figure 2.4:** A simplified ray diagram of the TEM showing the different arrangement between diffraction and imaging modes. Above the sample, shown in grey, the two beam diagrams are identical whilst the focal plane of the intermediate lens and aperture placement after the objective lens are changed between the two setups.

the optics are shown in Fig. 2.4.

The first lens after the specimen is the objective lens, often considered the most important lens in the microscope. The objective lens has the largest angle of incident beam of all the lenses in the microscope and, as discussed when considering spherical aberration, is fundamental to the image quality produced by the microscope. The objective lens focuses the image formed by the specimen before either the diffraction in the back focal plane or image plane is magnified by the intermediate lens. Depending on the imaging mode of the microscope an aperture can be placed in the plane not at the focal point of the intermediate lens. In the case of SAED the SAED aperture is placed in the image plane, isolating a specific area of the image.

The different real-space imaging modes are distinguished by the placing of the objective aperture. The modes and the position of the aperture are shown in Fig. 2.5. HRTEM has no aperture inserted, instead collecting all of the allowed scattering angles to form the image as a complicated interference pattern. This creates an image with high levels of detail as each diffraction spot contains information about the sample, however the contrast of the image is low.

Both BF-TEM and DF-TEM make use of an aperture, the objective aperture placed in the back focal plane of the objective lens. The difference between the modes being the diffraction spot isolated by the aperture. BF-TEM allows only the central beam to be transmitted to the intermediate lens, isolating the unscattered electrons. This causes the bright areas of the image to be where the electron pass straight through without an deflection, whilst in the areas of crystal that scatters the beam the image appears darker. This mode allows the film to be highlighted more clearly in the image as the material composition of the substrate will scatter the electron beam in a different way to the film, providing a contrast between the two. DF-TEM is also a diffraction contrast imaging mode whereby a non-central diffraction spot is isolated by the objective aperture. In this mode the resultant image is therefore brighter in the regions that scatter the electrons at the angle allowed by the selected Bragg condition. This mode is useful for distinguishing between phases and grains within the sample as the contrast and brightness will be lower in regions that do not satisfy the isolated Bragg condition.

The first lens in the projection system, often called the intermediate or diffraction lens, is used to select between diffraction and imaging mode. By shifting the focal plane of the intermediate lens between the back focal and image plane of the objec-

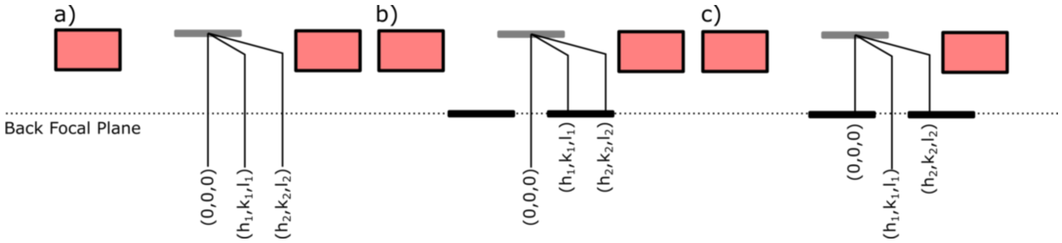

**Figure 2.5:** A schematic diagram of the three operational modes of real-space imaging in the TEM. Allowed reflections are shown leaving the specimen and objective lens, shown in the same form as in Fig. 2.4, where, depending on the mode, they are either blocked or allowed to pass to the intermediate lens. HRTEM is shown in a) where the entirety of the Bragg spots are allowed to pass through the back focal plane. As only the central spot passes in b) this is BF-TEM whilst isolation of a first order Bragg condition, shown in c), is the DF-TEM operation mode.

tive lens the operating mode of the TEM is switched between diffraction and imaging modes respectively. It also acts as the first lens in a series of projection lenses the magnify the image. By adjusting the current passing through the coils within the lenses the magnification can be increased or decreased. Doing so also increases or decreases the rotation of the light through the lens system meaning the resultant image rotates in the projection plane as the magnification is altered.

### 2.2.3 Scanning Transmission Electron Microscopy

Whereas a TEM operates with a parallel beam incident at the surface a STEM scans, in the case of aberration corrected machines, a sub-ångström converged probe[41,42] across the sample, rasterising an image. This scanning is achieved by a collection of scanning coils that shifts the probe by creating a the magnetic fields required to deflect the beam. Scanning the converged electron beam across the sample, rather than illuminating large areas with a parallel beam, allows for local probing of the sample. Rather than the phase contrast image, formed by the many interactions of the beam and sample, produced by HRTEM the position and composition of the sample is accessible to the STEM. A simplified schematic of the STEM is shown in Fig. 2.6.

Unlike the condenser lens in the TEM in the STEM the illumination system condenses the electrons exiting the Wehnelt cylinder into a converging beam. This beam then enters the probe corrector and scanning coils. The probe corrector, alongside stigmators that correct for the first order, adjusts for higher order spherical and chromatic aberrations for increased spatial resolution.

Once exiting the scanning coils the beam enters the objective lens, which further focuses the beam into the probe which is scanned across the surface. This is unlike

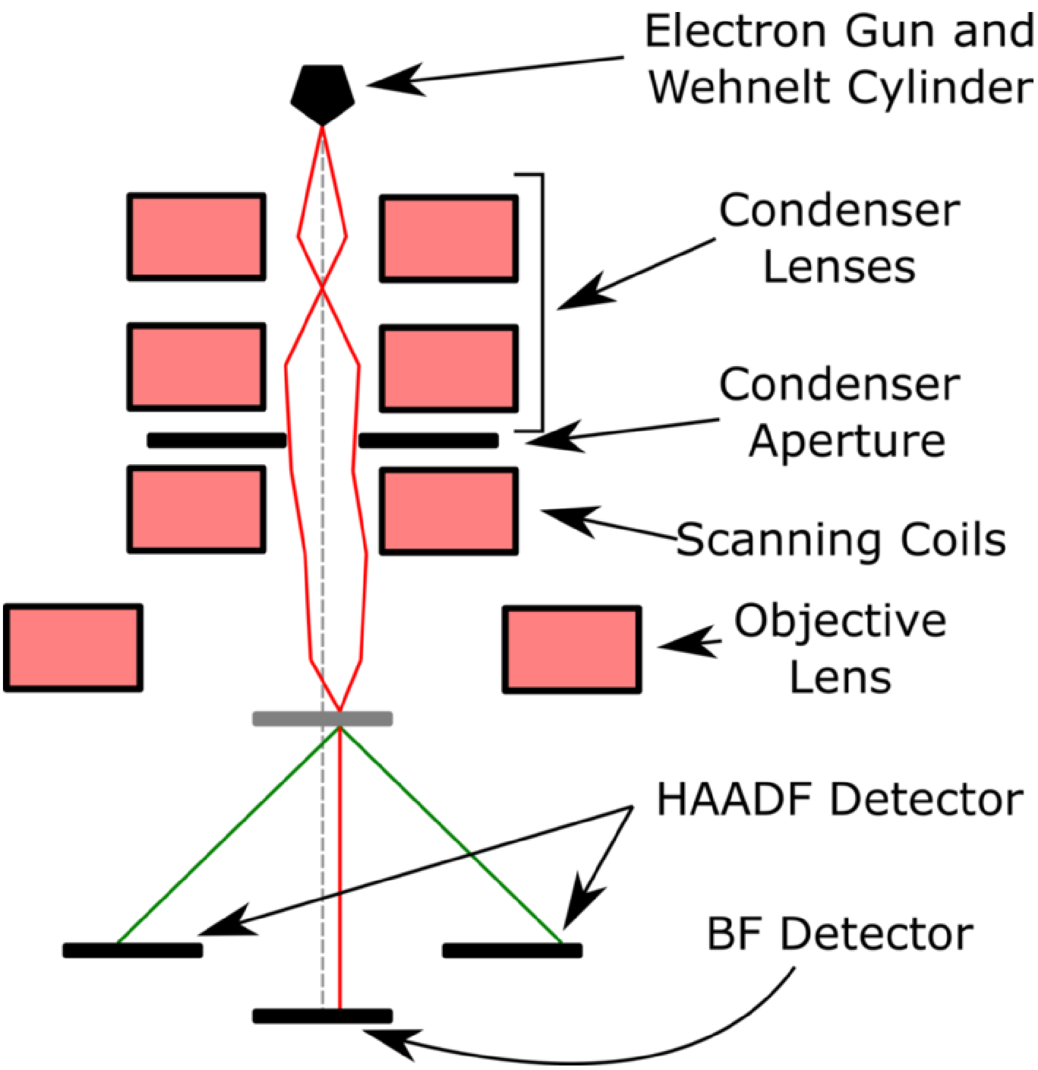

**Figure 2.6:** A simplified ray diagram of the TEM showing the different arrangement between diffraction and imaging modes. Above the sample, shown in grey, the two beam diagrams are identical whilst the focal plane of the intermediate lens and aperture placement after the objective lens are changed between the two setups.

the TEM where the objective lens acts on the beam as it leaves the sample. Instead the magnification of the STEM is dependant on the scanning window over which the probe is incident, with each movement of the probe corresponding to a pixel of the rasterised image produced. In this method of image collection the probe size limits the resolution and magnification of the image.

Also unlike the TEM the STEM has no lens systems after the beam leaves the sample. Instead after the sample plane are a series of detectors for different methods of imaging. In similar fashion to the TEM the detectors of the STEM centre around isolating regions of the back focal plane. Bright Field Scanning Transmission Electron Microscopy (BF-STEM) imaging, collected at a detector on the optical axis extending to an angle of 20mrad from the specimen, allows for the imaging of all species in the sample. The images formed are similar to BF-TEM however it has the ability to image light elements, such as oxygen, via a beam stop or phase contrast removal via in tandem use of an Annular Dark Field (ADF) detector.

Like the name suggests, ADF detectors, are ring-shaped detectors collecting scattered electrons outside the BF-STEM detector. Whilst a few modes of ADF imaging exist, low and medium angle ADF being examples, the most widely used is High Angle Annular Dark Field (HAADF).[43–45] As the beam no longer needs to pass through the objective lens after exiting the sample, the scattered electrons can be detected at higher angles than in a TEM. In the case of HAADF this is done within a 70-200mrad range from the optical axis. By removing the low angle scattering contributions from the image the diffraction contrast, present in the BF-TEM and DF-TEM modes, the image is instead dominated by the contrast caused by Rutherford scattering. This allows individual elements to be distinguished by their contrast and is why the technique is also known as Z-contrast imaging, however light elements, like oxygen, are practically invisible to the technique. As the electrons captured at the HAADF detectors are incoherently scattered the intensity can be considered the sum of the scattering intensities at atomic columns parallel to the beam in the sample.

A mixture of BF-STEM, HAADF, HRTEM and SAED techniques have been used to collect the data presented in this thesis

### 2.2.4 Sample Preparation

As previously mentioned samples for transmission electron microscopy have to be less than 100nm thick in the beam direction, as to achieve electron transparency. Manual preparation of samples for a TEM is a challenging, time consuming and often frustrating process that is not always successful. Focused Ion Beam (FIB) milling is a technique with a higher success rate for sample creation however this method of preparation leaves the surface is inaccessible to environmental TEMs and as such manual polishing was used for the samples presented in this thesis. The preparation of samples for the TEM is more often than not the limiting factor in resolving crystal structure. TEM imaging requires that the sample be as thin as possible to achieve the best image quality however as a sample reduces in size further complications arise. Samples that become too thin can loose their crystal structure as exposed surfaces, with normals parallel to the beam direction, dominate the sample. In these cases the

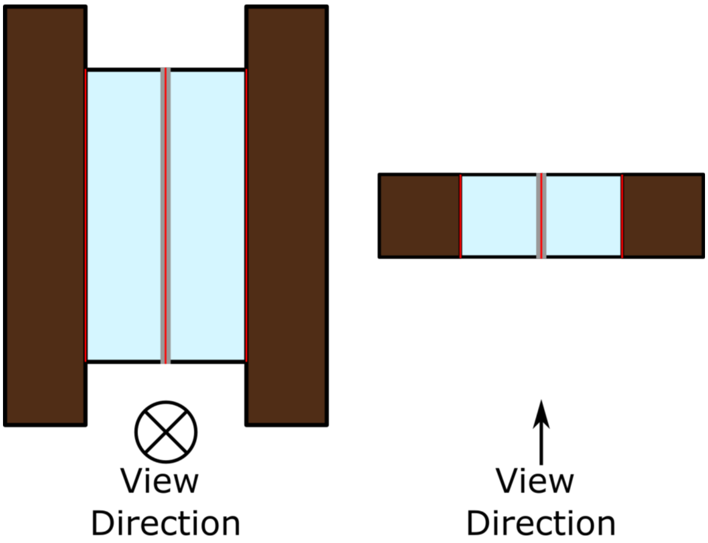

**Figure 2.7:** Cross-sectional sample preparation showing the sandwich style structure for polishing. The Si supports on the outside of the structure, shown in brown, are glued to the back of the substrates, shown in light blue. The thin-films, shown in grey, are glued opposing one another, using as little glue as possible to ensure low contamination when placed in the microscope.

samples may transition into an amorphous structure whilst also becoming more fragile. As such the production of optimal samples for the TEM is a balancing act between maintaining an accurate representation of the sample being viewed and the increasing image quality.

Manual polishing of samples is a destructive process whereby an area of 5mm$^2$ is, largely, discarded in the creation of a viable specimen. Firstly the sample is mounted to a glass slide using Cystalbond from Agar Scientific and two 2.5 × 1mm strips are cut from the material, with the short-edge parallel to the intended viewing direction, using a rotating diamond coated saw. Along with this two Si strips of slightly larger dimensions are cut, 3 × 1mm, and used as supports for the sample. A diagram showing the composition of the structure is shown in Fig. 2.7. Once cut the material is subjected to a three stage chemical cleaning process consisting of 3 minutes submerged in acetone followed by ethanol and finally isopropanol, all for the same amount of time and all in a sonicator. After the cleaning process a multi-layer structure is formed using the sample cuts and Si supports. In this structure the Si supports sandwich the two cuts of the sample which are bonded film-on-film with all materials glued together using minimal amounts of Gatan G1 epoxy. Once the epoxy has cured the sample is affixed to a glass slide and the manual polishing can begin.

First one side is slowly polished using 15, 9, 3 and finally 1$\mu$m diamond lapping pads until the interface of the films is free of scratches. The sample is then removed

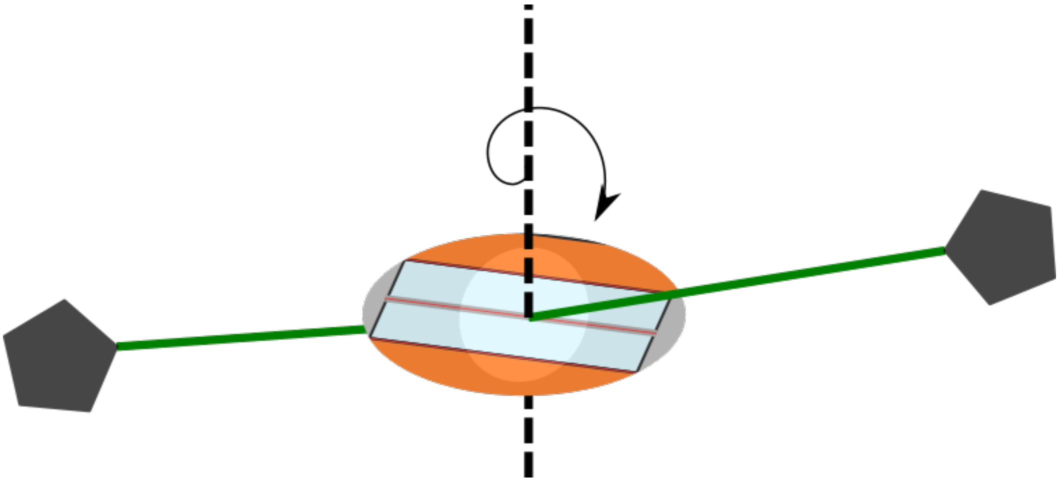

**Figure 2.8:** A diagram of the operation of the Gatan PIPS. Argon ion beams are fired from the guns at the sample from above and below at low grazing angles whilst the sample rotates. These beams are modulated to only fire when not within 30° of the beam being parallel to the glue line of the sample.

from the Crystalbond and cleaned using the same process mentioned earlier. A circular Cu or Mo grid is then affixed to the polished side, centring the film in the grids hole, using Gatan G1 epoxy. The sample is then re-situated on the glass slide, with Crystalbond, and the sample is thinned to 200$\mu$m, including the thickness of the TEM grid, using the 15$\mu$m lapping pad. The sample is then thinned to 150$\mu$m using the 9$\mu$m lapping pad and then to 100$\mu$m with the 3$\mu$m pad. From this thickness the 1$\mu$m pad is used but the thickness is no longer checked mechanically but instead an optical microscope is used in transmission mode.

Once the Si supports become thin enough their colour changes to a deep red as they become translucent. Depending on the fragility of the substrate the sample can be thinned further so that the Si supports become an orange, or more ideally a yellow, colour. At this stage the manual polishing is complete and the sample is carefully removed from the glass slide, by heating the Crystalbond, and subjected to the three stage chemical cleaning process. Excess Si material, extruding from the TEM grid, is removed with a diamond pen and the sample is ready for the next stage of the thinning process.

At this point the sample is now roughly 60$\mu$m thick and too thin for manual polishing without risking destroying the sample. As such the sample is now thinned using a Gatan Precision Ion Polishing System (PIPS). This machine accelerates argon ions, at up to 6keV, using two guns targeted at a rotating sample stage held within a vacuum. The guns are rotatable to create grazing angles between 0 and 10° above

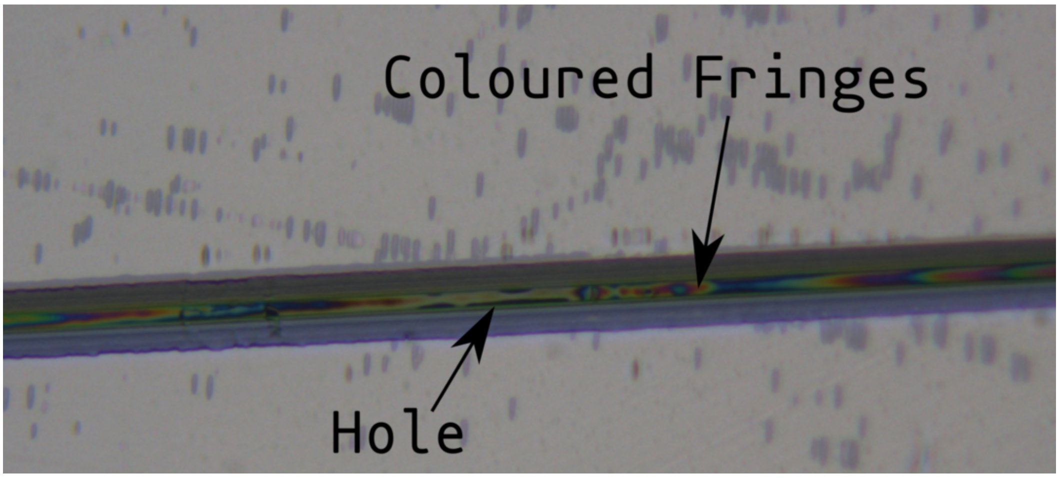

**Figure 2.9:** The coloured fringes around a hole formed in the centre of the glue line. The formation of the small holes indicates the sample is ready for the high angle, low energy cleaning stage.

and below the sample. A diagram of the operation of the PIPS is shown in Fig. 2.8. Using an accelerating voltage of 3.5keV and angles of $\pm5^\circ$ the sample is milled until colour fringes are visible via white light reflectance optical microscopy in the central trench, carved by the beam. These optical fringes indicate that a hole is soon to form and once it has formed the second stage of PIPS preparation can begin. Increasing the angle of the incident beams to $\pm8^\circ$ and reducing the beam voltage to 0.8keV the hole is carefully widened and around this hole will be suitable for transmission electron microscopy. The coloured fringes are shown in Fig. 2.9 along with a hole indicating the sample is ready for the high angle, low energy cleaning stage.

## 2.3 Atomic Force Microscopy

Another *ex-situ* characterisation technique employed in the duration of the project was Atomic Force Microscopy (AFM). This technique, in conjunction with electron microscopy and diffraction techniques, provides information on the surface quality of thin films. Like the STEM, AFM creates a rasterised image of the sample however this time sampling the 3-dimensional profile of the surface of the film. By measuring the force caused by the interaction between the surface and a sharp-tipped cantilever the height of the surface it a specific position is registered. As the probe is scanned across the surface a profile of the sample is captured. The tapping mode operation of an AFM, used in this thesis, detects the deflection the cantilever, oscillating at its resonant frequency, by tracking the position of a laser reflected off of the backside of the cantilever tip. The distance between cantilever and sample is set such that the tip makes contact at the bottom of its oscillation and a feedback loop is used to retain this distance as the probe is scanned. The technique is used to provide information on the surface roughness of films, calculated as the square-root of the second central moment of the height.[46,47]

## CHAPTER 3

# COMPUTATIONAL THEORY AND METHODOLOGY

Electronic structure defines the properties of a material, from the colour it appears to how it interacts with its environment. Thus an accurate description of the electrons within a system facilitates predictions of surface structures and can offer insight into the driving forces behind specific interactions. Computing the wavefunction for these types of systems is non-trivial however; there is no analytical solution available and the shear amount of information contained would make storing the wavefunctions impossible. Density-Functional Theory offers a practical solution to this, reducing the wavefunction to a functional of the combination of charge densities associated with non-interacting electrons. In this chapter the theory behind this simplification is presented. Key approximations are discussed and extensions to the theory are shown to allow for the treatment of materials beyond these base approximations. Methods for probing specific properties of systems, relevant to this thesis, are also explained as well as the practical implementation of the theory within the code VASP. Computer code, developed in the duration of this project, is also discussed in regards the theory behind the code.

## 3.1 Density-Functional Theory

### 3.1.1 The Many-body Problem

Since 1687, with the publication of Sir Isaac Newton's *Philosophiæ Naturalis Principia Mathematica*, the $n$-body problem has plagued scientists.[48] The simplest of these systems, a two-body problem, may be solved by reduction into two individual single-body problems. The *Principia* went further and put forth verbal and geometrical discussions of the motions of three massive bodies acting under a single force, gravity. With just this addition of a third entity a reformulation is no longer possible and a general analytical solution unknown. The difficulty and chaotic nature of the macroscopic $n$-body problem is amplified in the microscopic Coulomb equivalent many-body problem, prevalent when considering the electronic structure of crystals. The successful, and rigorous, solution requires the calculation of interactions between every individual particle and the remaining particles. When considering hundreds of atoms and thousands of electrons it is clear how this could become increasingly complex, even if an analytical solution was possible.

For quantum mechanical systems there exist a range of techniques for handling the many-body problem. Semi-empirical methods, such as Modified Neglect of Diatomic Overlap (MNDO),[49] offer low computational cost at the expense of parameterising and approximating electron-electron interactions across atomic sites. Quantum Monte-Carlo (QMC) provides near exact solutions with extreme computational cost and as such QMC is often used rather as a benchmark or to validate results. DFT is a popular, and highly successful, middle ground by adopting similar logic as that of the two-body problem. Instead of treating each individual electron, a system of auxiliary non-interacting particles are considered whereby their total density matches exactly the density of the interacting system. This reduces the system from a single many-body problem to many single-body problems. This approach, whilst remaining computationally cheap, often provides good agreement with experiment for ground-state properties such as lattice parameters and adsorption energies.

### 3.1.2 Born-Oppenhiemer Approximation

The information about each state, $i$, in quantum mechanical systems is stored within their wavefunctions, $\Psi_i$. The Time-Independent Schrödinger Equation (TISE), assuming non-relativistic velocities, provides a way of calculating this wavefunction,

$$\hat{\mathcal{H}}\Psi_i = E_i\Psi_i \tag{3.1}$$

where the wavefunction here depends on the position of all electrons and nuclei in the system, $\mathbf{r}_j$ and $\mathbf{R}_k$ respectively,

$$\Psi_i = \Psi_i\left(\mathbf{r}_1, \mathbf{r}_2, \ldots, \mathbf{r}_{N_e}, \mathbf{R}_1, \mathbf{R}_2, \ldots, \mathbf{R}_{N_n}\right) \tag{3.2}$$

wit $N_e$ and $N_n$ representing the total number of electrons and nuclei. The Hamiltonian contains kinetic energy operators for both electrons and nuclei as well as potential terms for the combination of interactions between the two and an, often zero, external electric potential:

$$\hat{\mathcal{H}} = \hat{\mathcal{T}}_n + \hat{\mathcal{T}}_e + \hat{\mathcal{U}}_{\text{n-n}} + \hat{\mathcal{U}}_{\text{n-e}} + \hat{\mathcal{U}}_{\text{e-e}} + \hat{\mathcal{V}}_{\text{pot}} \tag{3.3}$$

The operators are presented in full below, where all terms have their usual meaning and Coulomb's constant is defined as $k_e = \frac{1}{4\pi\epsilon_0}$

$$\hat{\mathcal{T}}_n = -\frac{\hbar^2}{2}\sum_i^{N_n}\frac{\nabla_i^2}{m_i} \qquad \hat{\mathcal{U}}_{\text{n-n}} = k_e\sum_i^{N_n}\sum_{j>i}^{N_n}\frac{Z_iZ_j}{|\mathbf{R}_i - \mathbf{R}_j|} \qquad \hat{\mathcal{V}}_{\text{pot}} = v_{\text{pot}}\left(\mathbf{r}\right)$$

$$\hat{\mathcal{T}}_e = -\frac{\hbar^2}{2m_e}\sum_i^{N_e}\nabla_i^2 \qquad \hat{\mathcal{U}}_{\text{e-e}} = k_e\sum_i^{N_e}\sum_{j>i}^{N_e}\frac{e^2}{|\mathbf{r}_i - \mathbf{r}_j|}$$

$$\hat{\mathcal{U}}_{\text{e-n}} = k_e\sum_i^{N_e}\sum_j^{N_n}\frac{-eZ_j}{|\mathbf{r}_i - \mathbf{R}_j|}$$

The Born-Oppenhiemer approximation asserts that the motion of the electrons and nuclei can be treated separately for small time scales.[50] This is due to the relatively small mass of the electrons allowing them to react much faster to changes in the potential; the nuclei are stationary and representable as an external potential. This allows it to be combined with the external electric potential to form

$$v_{\text{ext}} = v_{\text{n-e}} + v_{\text{pot}} \tag{3.4}$$

The TISE is now reducible to only depend on the electron positions with $v_{\text{ext}}$ including the fixed nuclei position equivalent of $\hat{\mathcal{U}}_{e-n}$.

$$\left[\hat{\mathcal{T}}_e + \hat{\mathcal{U}}_{\text{e-e}} + v_{\text{ext}}\right]\Psi_i = E_i\Psi_i\left(\mathbf{r}_1, \mathbf{r}_2, \ldots, \mathbf{r}_{N_e}\right) \tag{3.5}$$

### 3.1.3 Hohenberg-Kohn Theorem

Extracting the previously mentioned information from $\Psi_i$ is done by taking the expectation value of operators to reveal observables. One such observable is the particle density which, for a given number of electrons, is uniquely determined by the external potential, $v_{ext}$. The Hohenberg-Kohn theorem allows for the inversion of this mapping when considering the ground-state of the system; given a ground-state particle density, $n_0(\mathbf{r})$, the external potential can be found and as such the ground-state wavefunction, $\Psi_0$, can be calculated.[51] Therefore the ground-state wavefunction can be expressed as a functional of the ground-state particle density,

$$\Psi_0\left(\mathbf{r}_1, \mathbf{r}_2 \ldots \mathbf{r}_{N_e}\right) = \Psi\left[n_0\left(\mathbf{r}\right)\right] \tag{3.6}$$

From this it follows that if you operate upon the ground-state wavefunction to find a ground-state expectation value this too will be a functional of $n_0(\mathbf{r})$,

$$\left\langle \Psi\left[n_0\left(\mathbf{r}\right)\right] \middle| \hat{O} \middle| \Psi\left[n_0\left(\mathbf{r}\right)\right] \right\rangle = O\left[n_0\right] \tag{3.7}$$

Taking the previously mentioned Hamiltonian from Eq. (3.5) an expression for the ground-state energy of the system can now be written in terms of the particle density,

$$E\left[n_0\right] = \left\langle \Psi\left[n_0\left(\mathbf{r}\right)\right] \middle| \hat{\mathcal{T}}_e + \hat{\mathcal{U}}_{\text{e-e}} \middle| \Psi\left[n_0\left(\mathbf{r}\right)\right] \right\rangle + \int d\mathbf{r}\, n_0\left(\mathbf{r}\right) v_{ext}\left(\mathbf{r}\right) \tag{3.8}$$

The second part of the Hohenberg-Kohn theorem, the variational principle, follows from this stating that the ground-state particle density minimises this energy functional,

$$E\left[n_0\right] \leq E\left[n'\right] \tag{3.9}$$

Recalling that $\hat{\mathcal{T}}_e$ and $\hat{\mathcal{U}}_{\text{e-e}}$ are the standard kinetic and electron-electron Coulomb operators respectively, and therefore independent of the system, Eq. (3.8) can be rewritten

$$E\left[n_0\right] = \mathcal{T}_e\left[n_0\right] + \mathcal{U}_{\text{e-e}}\left[n_0\right] + \mathcal{V}_{ext}\left[n_0\right] \tag{3.10}$$

Where the system dependent expectation value

$$\mathcal{V}_{ext}\left[n_0\right] = \int d\mathbf{r}\, n_0\left(\mathbf{r}\right) v_{ext}\left(\mathbf{r}\right) \tag{3.11}$$

is known explicitly once the system is defined. The functional forms of the expectation values $\hat{\mathcal{T}}_e$ and $\hat{\mathcal{U}}_{\text{e-e}}$ are unknown making minimising the ground-state energy problematic.

### 3.1.4 Kohn-Sham Density-Functional Theory

A reasonable approximation of the interaction energy, $\mathcal{U}_{\text{e-e}}[n]$, is the energy from the electrostatic interaction of the particle density. This is known as the Hartree energy and has the form

$$\mathcal{U}_H[n] = \frac{e^2 k_e}{2} \int d\mathbf{r} \int d\mathbf{r}' \frac{n(\mathbf{r})\, n(\mathbf{r}')}{|\mathbf{r} - \mathbf{r}'|} \tag{3.12}$$

The kinetic energy of the electrons, $\mathcal{T}_e[n]$, can be thought of as the energy of non-interacting particles plus a correlation term

$$\mathcal{T}_e[n] = \mathcal{T}_s[n] + \mathcal{T}_c[n] \tag{3.13}$$

Single-particle orbitals, $\phi_i$, of the non-interacting system of density $n_s(\mathbf{r})$ are used to describe the non-interacting term.

$$\mathcal{T}_s[n] = \left\langle \phi_i[n_s] \middle| \hat{\mathcal{T}}_s \middle| \phi_i[n_s] \right\rangle = \mathcal{T}_s[\{\phi_i[n_s]\}] \tag{3.14}$$

Where $T_s[\{\phi_i[n_s]\}]$ means the non-interacting kinetic energy is now dependent upon a full set of occupied orbitals and these orbitals are a functional of the single-particle density. It is now possible to rewrite Eq. (3.10) with only one unknown functional

$$E[n] = \mathcal{T}_s[\{\phi_i[n_s]\}] + \mathcal{U}_H[n] + \mathcal{V}_{ext}[n] + E_{xc}[n] \tag{3.15}$$

where said unknown functional is known as the Exchange-Correlation (xc) energy and combines the difference between the true expected values of the kinetic and interaction energy with the ones just introduced

$$E_{xc}[n] = \mathcal{T}_c[n] + (\mathcal{U}_{\text{e-e}}[n] - \mathcal{U}_H[n]) \tag{3.16}$$

The functional form of this term is not known. However, xc energy is considered, and often found to be, relatively small in magnitude when compared to the other energies in Eq. (3.15). As such reasonable estimations of the xc energy still give results in accordance with experiment.

The Kohn-Sham (KS) approach starts by expressing the minimisation as a stationary point of the energy functional

$$\begin{aligned} 0 = \frac{\delta E\left[n\right]}{\delta n\left(\mathbf{r}\right)} &= \frac{\delta \mathcal{T}_s\left[n\right]}{\delta n\left(\mathbf{r}\right)} + \frac{\delta \mathcal{U}_H\left[n\right]}{\delta n\left(\mathbf{r}\right)} + \frac{\delta \mathcal{V}_{ext}\left[n\right]}{\delta n\left(\mathbf{r}\right)} + \frac{\delta E_{xc}\left[n\right]}{\delta n\left(\mathbf{r}\right)} \\ &= \frac{\delta \mathcal{T}_s\left[n\right]}{\delta n\left(\mathbf{r}\right)} + v_H\left(\mathbf{r}\right) + v_{ext}\left(\mathbf{r}\right) + v_{xc}\left(\mathbf{r}\right) \end{aligned} \tag{3.17}$$

$$v_H\left(\mathbf{r}\right) = q^2 k_e \int d\mathbf{r}' \frac{n\left(\mathbf{r}'\right)}{\left|\mathbf{r}-\mathbf{r}'\right|} \tag{3.18}$$

Where $v_H\left(\mathbf{r}\right)$ is the Hartree potential, $v_{ext}\left(\mathbf{r}\right)$ is the potential caused by the stationary nuclei and any other external field applied to the system, and xc potential, $v_{xc}\left(\mathbf{r}\right)$, is found explicitly from the chosen approximation for $E_{xc}\left[n\right]$. From direct comparison to the minimisation criteria for the non-interacting system

$$\begin{aligned} 0 = \frac{\delta E_s\left[n\right]}{\delta n\left(\mathbf{r}\right)} &= \frac{\delta T_s\left[n\right]}{\delta n\left(\mathbf{r}\right)} + \frac{\delta V_s\left[n\right]}{\delta n\left(\mathbf{r}\right)} \\ &= \frac{\delta T_s\left[n\right]}{\delta n\left(\mathbf{r}\right)} + v_s\left(\mathbf{r}\right) \end{aligned} \tag{3.19}$$

the first Kohn-Sham equation[52] is realised to convert the many-body problem into a single-body one

$$v_s\left(\mathbf{r}\right) = v_H\left(\mathbf{r}\right) + v_{ext}\left(\mathbf{r}\right) + v_{xc}\left(\mathbf{r}\right) \tag{3.20}$$

Solving the TISE for this system, where $\epsilon_i$ is energy eigenvalue for the $i$-th single-particle orbital,

$$\left[-\frac{\hbar^2\nabla^2}{2m_e} + v_s\left(\mathbf{r}\right)\right]\phi_i\left(\mathbf{r}\right) = \varepsilon_i\phi_i\left(\mathbf{r}\right) \tag{3.21}$$

produces orbitals identical to those in Eq. (3.14) as they reproduce the density of the interacting system

$$n\left(\mathbf{r}\right) \equiv n_s\left(\mathbf{r}\right) = \sum_i^{occ} f_i \left|\phi_i\left(\mathbf{r}\right)\right|^2 \tag{3.22}$$

where $f_i$ is the orbital occupation. Whilst these three equations have reduced the complexity of the system to that of a non-interacting one, it has introduced a self dependency. This is because $v_H$ and $v_{xc}$ are both defined in terms of the density, which through the above equation is dependant on the orbitals which in turn, via Eqs.(3.20, 3.21), is dependant on the aforementioned potentials. This means to find the ground-state density requires completing a self-consistency cycle where $n\left(\mathbf{r}\right)$ is iteratively improved through the process:

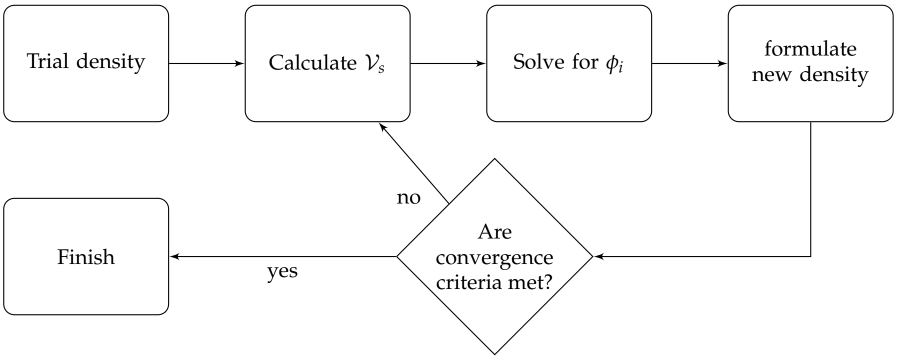

Once the convergence criteria has been met the ground-state energy of the original system is then found by relating Eq. (3.12) and Eq. (3.18) to rewrite the expectation value of the Kohn-Sham potential operator

$$\begin{aligned}\mathcal{V}_s[n] &= \int d\mathbf{r}\, v_s(\mathbf{r})\, n(\mathbf{r}) = \int d\mathbf{r}\left[v_H(\mathbf{r}) + v_{ext}(\mathbf{r}) + v_{xc}(\mathbf{r})\right] n(\mathbf{r}) \\ &= 2\,\mathcal{U}_H[n] + \mathcal{V}_{ext}[n] + \int d\mathbf{r}\, v_{xc}(\mathbf{r})\, n(\mathbf{r})\end{aligned} \tag{3.23}$$

Then realising

$$E_s[n] = \sum_i^{occ} f_i \varepsilon_i = \mathcal{T}_s[n] + \mathcal{V}_s[n] \tag{3.24}$$

These can then be used to find the total energy of the ground-state by combining these with Eq. (3.15) to give

$$E_0 = \sum_i^{occ} f_i \varepsilon_i - \mathcal{U}_H[n_0] - \int d\mathbf{r}\, v_{xc}(\mathbf{r})\, n_0(\mathbf{r}) + E_{xc}[n_0] \tag{3.25}$$

### 3.1.5 Exchange-Correlation Functionals

There exist two widely used forms of approximation for the unknown functional $E_{xc}$, the Local Density Approximation (LDA) and Generalised Gradient Approximation (GGA). The LDA considers a Homogeneous Electron-Gas (HEG) made charge neutral by a rigid, uniformly distributed, positive background charge. By calculating the xc energy per electron for this HEG, $\epsilon_{xc}(n)$, with density equal to that of related position within the studied system, the approximate xc functional is formed

$$E_{xc}^{LDA}[n] = \int d\mathbf{r}\, n(\mathbf{r})\, \epsilon_{xc}(n) \tag{3.26}$$

Whilst this formulation of the xc functional works well for crystalline metals, due to their slowly varying densities, improvements can be made by incorporating gradient corrections as to better describe the xc energy for materials with greater rates of density variation. This is known as the GGA and takes the form

$$E_{xc}^{GGA}\left[n\right] = \int d\mathbf{r}\, f\left(n\left(\mathbf{r}\right), \nabla n\left(\mathbf{r}\right)\right) \tag{3.27}$$

Different variants of the function, $f\left(n\left(\mathbf{r}\right), \nabla n\left(\mathbf{r}\right)\right)$, exist denoting distinct versions of a GGA functional. This project uses the Perdew-Burke-Ernzerhof (PBE) functional.[53]

### 3.1.6 Spin Channels

Like the xc energy, magnetisation density has an unknown form as a functional of the particle density. Kohn-Sham DFT can still be extended to include the collinear spin density of the electrons by introducing independent densities for each spin channel, $n^{\alpha}\left(\mathbf{r}\right)$ and $n^{\beta}\left(\mathbf{r}\right)$.

$$n\left(\mathbf{r}\right) = n^{\alpha}\left(\mathbf{r}\right) + n^{\beta}\left(\mathbf{r}\right) \tag{3.28a}$$

$$Q\left(\mathbf{r}\right) = n^{\alpha}\left(\mathbf{r}\right) - n^{\beta}\left(\mathbf{r}\right) \tag{3.28b}$$

The energy functional from Eq. (3.15) is now written as

$$E\left[n,Q\right] = \mathcal{T}_s\left[n,Q\right] + \mathcal{U}_H\left[n\right] + \mathcal{V}_{ext}\left[n\right] + E_{xc}\left[n,Q\right] \tag{3.29}$$

where $\mathcal{T}_s\left[n,Q\right]$ is the sum of the individual kinetic operators for each spin channel and $E_{xc}\left[n,Q\right]$ is defined much like previously only with a spin-polarised HEG as a reference and as such a spin density dependence.

$$E_{xc}^{GGA}\left[n,Q\right] = \int d\mathbf{r}\, f\left(n,Q,\nabla Q\right) \tag{3.30}$$

### 3.1.7 Bloch's Theorem

When considering the materials to be studied using DFT, approximations must be made to reduce the system size to something computable on modern hardware. To this end, across many forms of electronic structure modelling, periodic boundary conditions are employed. Through this the environment of a much larger crystal is simulated using the least amount of atoms necessary. The primitive cell of a material is the smallest tiling cell required to describe the lattice structure. In a 3 dimensional system

| Lattice System | Centring Type |  |  |  |
|---|---|---|---|---|
|  | Primitive | Base-centred | Body-centred | Face-centred |
| Triclinic | ✓ | x | x | x |
| Monoclinic | ✓ | ✓ | x | x |
| Orthorombic | ✓ | ✓ | ✓ | ✓ |
| Tetragonal | ✓ | x | ✓ | x |
| Rhombohedral | ✓ | x | x | x |
| Hexagonal | ✓ | x | x | x |
| Cubic | ✓ | x | ✓ | ✓ |

**Table 3.1:** The available centring types for the 7 lattice system in 3D space.

the vectors to describe this are given as

$$\mathbf{a} = a_1\hat{\mathbf{x}} + a_2\hat{\mathbf{y}} + a_3\hat{\mathbf{z}} \tag{3.31a}$$

$$\mathbf{b} = b_1\hat{\mathbf{x}} + b_2\hat{\mathbf{y}} + b_3\hat{\mathbf{z}} \tag{3.31b}$$

$$\mathbf{c} = c_1\hat{\mathbf{x}} + c_2\hat{\mathbf{y}} + c_3\hat{\mathbf{z}} \tag{3.31c}$$

where the set $\{\mathbf{a}, \mathbf{b}, \mathbf{c}\}$ spans $\mathbb{R}^3$ and taking a point within this cell and applying a translation

$$\mathbf{R} = n_1\mathbf{a} + n_2\mathbf{b} + n_3\mathbf{c} \tag{3.32}$$

for integer values of $n_1, n_2$ & $n_3$ returns the same point within a repeat of the cell. Using this description of the lattice there exist 230 space groups of distinct symmetry operations that can represent crystal structure. However it is often easier to instead characterise the lattice using the 14 non isomorphic symmetry groups, known as Bravais lattices. These lattices are a combination of the 7 lattice systems and their available centring types as shown in Table 3.1. The reciprocal lattice is defined as,

$$\mathbf{a}^* = 2\pi\frac{\mathbf{b} \times \mathbf{c}}{\mathbf{a} \cdot (\mathbf{b} \times \mathbf{c})} \tag{3.33a}$$

$$\mathbf{b}^* = 2\pi\frac{\mathbf{c} \times \mathbf{a}}{\mathbf{b} \cdot (\mathbf{c} \times \mathbf{a})} \tag{3.33b}$$

$$\mathbf{c}^* = 2\pi\frac{\mathbf{a} \times \mathbf{b}}{\mathbf{c} \cdot (\mathbf{a} \times \mathbf{b})} \tag{3.33c}$$

and is translationally periodic in the same way.

$$\mathbf{G} = n_1\mathbf{a}^* + n_2\mathbf{b}^* + n_3\mathbf{c}^* \tag{3.34}$$

Bloch's Theorem[54] states that the wavefunctions, $\psi_{n,\mathbf{k}}(\mathbf{r})$, of a system that is periodic in this way (a perfect crystal) can be represented as Bloch waves

$$\psi_{n,\mathbf{k}}\left(\mathbf{r}\right) = u_{n,\mathbf{k}}\left(r\right) e^{i\mathbf{k}\cdot\mathbf{r}} \tag{3.35}$$

where $u_{n,\mathbf{k}}\left(\mathbf{r}\right)$ is a function that shares the same periodicity as the crystal and $\mathbf{k}$ is a wave-vector in the reciprocal lattice basis. Substitution into the single-particle TISE from Eq. (3.21) gives

$$\left[-\frac{\hbar^2\left(\nabla + i\mathbf{k}\right)^2}{2m_e} + v_s\left(\mathbf{r}\right)\right] u_{n,\mathbf{k}}\left(\mathbf{r}\right) = \varepsilon_{n,\mathbf{k}} u_{n,\mathbf{k}}\left(\mathbf{r}\right). \tag{3.36}$$

This shows that the eigenvalues, $\varepsilon_{n,\mathbf{k}}$, vary with position in $k$-space giving rise to the band structure of the crystal. The band structure provides useful information about the electronic structure of system such as the nature of the band gap, either direct or indirect, as well as the locality of electron orbitals within the system.

### 3.1.8 Brillouin Zone Sampling

Using a Bloch wave to describe the wavefunction introduced a dependence on the wave-vector **k**. There are many properties of a crystal that are now described by an integration over all of $k$-space, the density for example. Fortunately, as the reciprocal lattice is also periodic, the region this spans can be completely described within the 1st Brillouin zone of the reciprocal lattice. Discretising this space is often done with a Monkhorst-Pack grid. This is a uniform grid of points in $k$-space, defined by the reciprocal basis vectors. Often a shift is performed to grids with even spacing of half a reciprocal lattice vector in each dimension to centre the grid on $\Gamma$, the **k** vector (0, 0, 0). This can help with convergence and is required by hexagonal lattices to to fully describe the symmetry of the crystal. With this shift $k$-points can be generated for the grid,

$$\mathbf{k} = \frac{n_1}{N_1}\mathbf{a}^* + \frac{n_2}{N_2}\mathbf{b}^* + \frac{n_3}{N_3}\mathbf{c}^* \tag{3.37}$$

Where $N_1$, $N_2$ and $N_3$ are the dimensions of the grid and $n_1$, $n_2$ and $n_3$ cover all positive integers less then their respective dimension. The amount of grid points to be used varies per system and must be carefully converged for the material of interest. The more dispersive the bands in a system are, the more $k$-space needs to be sampled to accurately describe the eigenvalue variance in $k$-space. In the absence of an external electric field the number of required $k$-points can be halved due to time-reversal symmetry

$$\psi_{n,\mathbf{k}}\left(\mathbf{r}\right) = \psi^{*}_{n,-\mathbf{k}}\left(\mathbf{r}\right). \tag{3.38}$$

## 3.2 Density-Functional Theory Extensions

### 3.2.1 Hubbard-like Correction

**Self-Interaction**

In the reduction of the many-body problem to a non-interacting system an error associated with the self-interaction of the system arises. Each single-particle orbital is interacting with a potential consisting of functional derivatives containing the entire density; the orbitals are, in effect, interacting with themselves. The exact xc functional would account for this, however, the current approximations leave in residual self-interaction. Self-interaction causes a delocalisation of the particles due to them being repelled by themselves, leading to more dispersive bands. This is problematic when modelling any localised charge within a system, such as the highly correlated $d$-orbitals in transition metals. The dispersive $d$-orbitals, caused by the self-interaction error, in these transition metals drastically change the electronic structure of the material, leading to highly erroneous predictions of the material's properties. In the case of NiO this leads to the wrong ground-state magnetic ordering, a near non-existent band-gap and even predicts $Ni_2O_3$ as the most stable phase.[55]

**DFT+$U$**

DFT with a Hubbard-like correction (DFT+$U$) is able to overcome the on-site Coulomb interaction of these systems with its own on-site parameters, Coulomb, $U$, and exchange, $J$. There are a few methods dictating how to apply these values however one of the most widely used is the Dudarev method.[56] In this approach the energy of the system is penalised for having wavefunctions spread over multiple atoms, using the difference between $U$ and $J$, denoted as $U_{eff}$ to scale the magnitude of this penalty. This is achieved by modifying the total energy of the system to include a term dependant on the on-site orbital occupation number, $\lambda_i^{I,\sigma}$

$$E_{DFT+U} = E_{DFT} + \frac{U_{eff}}{2}\sum_{I,\sigma}\sum_{i}\lambda_i^{I,\sigma}\left(1-\lambda_i^{I,\sigma}\right) \tag{3.39}$$

where $I$ is the atomic site with spin $\sigma$ and $i$ denotes a wavefunction of the specific angular momentum for which the penalty is applied. In Fig.(3.1) an illustration of the effect DFT+$U$ has on the 3$d$-orbitals of Ni within a bulk NiO cell is shown. It is clear the increased localisation the method provides for these states with the shape of the orbitals being drastically different also. The localisation shown by this figure can be tuned by the selection of the $U_{eff}$ value and as such care must be taken in the selection of this parameter.

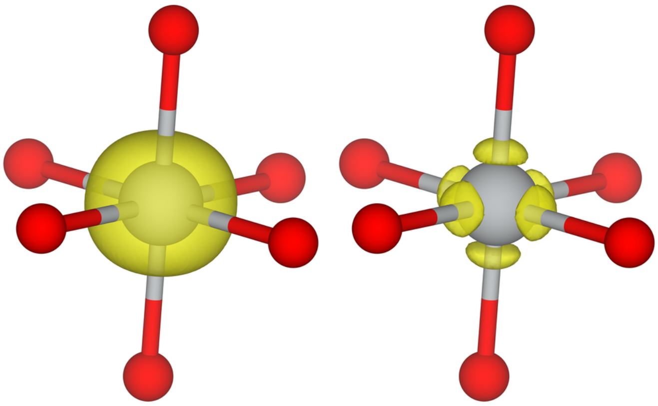

**Figure 3.1:** Projected $d$-orbitals surrounding a Ni atom from a VASP calculation on bulk NiO. The left image shows the orbitals from a standard DFT calculation whilst the right is a DFT+$U$ calculation with a $U_{eff}$ of 5.3 eV. Both images are produced using the same isosurface value for the charge density.

In practice the values are often obtained semi-empirically, matching specific properties of the material being studied with values for the on-site Coulomb and exchange parameters. Within this thesis the a $U_{eff}$ of 5.3 eV was used on the $d$-orbitals of Ni when studying NiO. This value was taken from literature[57] where it was shown to gave good agreement with many properties of the material, including magnetic ordering and the band-gap.

### Bader Charge Partitioning

Assigning charge from the charge density to atoms is not an easy task in DFT. This is due to the single-particle wavefunctions not representing the electrons in the system, instead representing fictitious non-interacting particles which make up a system with an identical total charge density. The quantum theory of atoms in molecules, developed by Richard Bader,[58] defines an atom solely on the bounds of zero-flux surfaces within the charge density. Zero-flux surfaces are 2-dimensional surfaces at which the gradient of the charge density does not cross. By following the gradient of the charge density from each voxel to a maximum, regions of charge are partitioned into basins that flow to the same maxima in the density. These basins are then assigned to the atom nearest the position of the maximum value. As the calculation of the gradient of a grid based density is trivial, this method of charge partitioning has become a popular form of analysis of the charge density calculated by DFT.

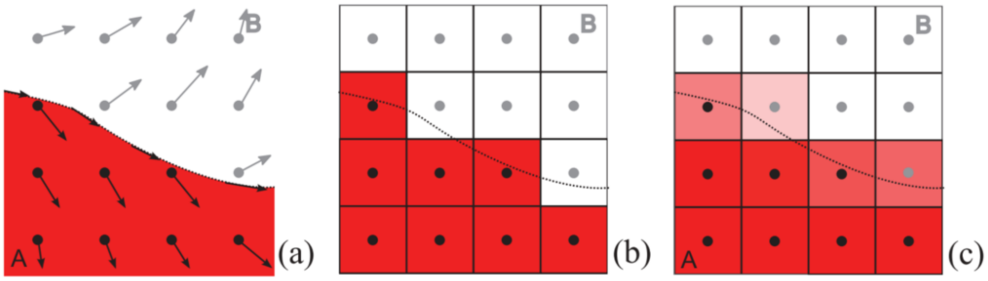

**Figure 3.2:** A schematic illustration of the zero-flux surface, shown as the dotted line in all three images. Basins A and B, represented by the colours red and white respectively, are separated by the zero-flux surface in a 2-dimensional representation of a discretised charge density. Each voxel, represented by a dot has a gradient associated to it, depicted by the magnitude and direction of the arrow coming from each voxel in a). The problem associated with the discretisation of the grid is shown in b) whilst c) shows the effect of the weight method assigning multiple weighted maxima to the boundary voxels. This figure was sourced from Ref. 59.

One problem associated with calculating gradients within the charge density is the bias imparted on them by the underlying voxel grid. This makes the calculation of the zero-flux surfaces difficult as the direction of the gradient is discretised and so the boundaries between atoms introduce an error in the assigned charge. The most obvious way to correct this is to increase the number of voxels in the charge density grid, however this increases both the time to run the DFT calculation as well as time to partition the charge. Another solution is to instead calculate the gradient along the Voronoi vectors of the lattice. The Voronoi vectors of the lattice are defined as the unit vectors normal to the Voronoi surfaces around lattice, the surface halfway between the origin of a voxel and its nearest neighbour voxels. Once the flux along each Voronoi vector has been calculated voxels at the boundary between basins are assigned a weight based on the flux into each basin. The boundary is now a soft transition between basins. This method, explained in full within Ref. 59, reduces the integration error associated with the lattice bias and discretisation of the gradient. Fig. 3.2[59] shows the way discretisation is minimised using this method allowing for less error in the partitioned charge with fewer grid points.

In practice these calculations can be time consuming due to the high voxel count in large supercells, exacerbated further in cells containing vacuum gaps due to the computation time being dependent upon the number of basins. For this thesis a new software package was developed that removed the dependence upon the number of basins and implemented a multi-threaded approach allowing for the parallelisation of the computation.[60] Code snippets of the software with brief commentary are given in Appendix A.

## 3.3 Computational Implementation of DFT

As previously discussed the many-body problem has no analytical solution and as such a numerical solution is required. There exist many DFT codes that often approach the complexity of solving the KS equations in different ways. This section will focus on tackling these equations using a plane-wave basis set with pseudo-potentials defined using the Projector Augmented Wave (PAW) method. It will discuss the benefits of using these methods over other available options as well as further analysis available by studying the derivatives of the total energy with respect to atomic positions. This further analysis will be described with respect to how they are done in the Vienna Ab initio Simulation Package (VASP) – the software package used in this thesis.

### 3.3.1 Plane-wave Basis

Storing the KS single-particle wavefunctions, in real-space, for each electron in the system would require a large amount of memory. As such a set of basis functions, $\phi_v$, are used to describe the wavefunction, $\psi_i$, instead.

$$\psi_i = \sum_{\nu} C_{i\nu}\phi_\nu \tag{3.40}$$

Now only the coefficients, $C_{iv}$, need to be stored for each wavefunction. It is obviously infeasible to store an infinite amount of basis coefficients and so the amount of functions is truncated once the basis set is reasonably complete. The basis set is considered reasonably complete once, to a tolerance often in-line with chemical accuracy, the property of the system that is to be studied, often the total energy, is converged with respect to the number of basis coefficients. It is wise to test this truncation against all prominent aspects of a calculation as different properties converge at different rates, with respect to basis completeness.

Plane-waves are often used as the basis set for DFT software packages as transforming between real-space Bloch waves, $u_{n,\mathbf{k}}(r)$, Eq. (3.35) and the basis set requires only a, computationally inexpensive, Fourier transform.

$$u_{n,\mathbf{k}}(\mathbf{r}) = \frac{1}{\Omega^{1/2}} \sum_{|\mathbf{G}+\mathbf{k}|<G_{cut}} C_{n,\mathbf{k}}(\mathbf{G})\, e^{i\mathbf{G}\cdot\mathbf{r}} \tag{3.41}$$

Notice that the number of plane-waves varies across $k$-points, this helps smooth the change in plane-waves and energy at different volumes of the cell, $\Omega$. $G_{cut}$ is the truncation cut-off wavevector and is often quoted instead as a cutoff energy.

$$E_{cut} = \frac{\hbar^2}{2m} G_{cut}^2 \tag{3.42}$$

As well as their speed plane-wave basis functions have other advantages over other basis choices, such as atom centred Gaussian basis functions. One advantage is that the basis is independent of atomic positions, so there is no change in overlap of basis functions as atoms move. In contrast the atom centred basis functions is lead to extra Pulay forces on the atoms that can be expensive to compute. For this reason using a plane-wave basis set is a good option for geometric optimisations, and other calculations dependent on derivatives of the total energy, at constant volume.

### 3.3.2 Pseudo-Potentials

The transformation between basis set and real-space needs to be done for every occupied wavefunction in the system. The computational cost of this is rather high with the operation scaling as $\mathcal{O}(N_e \cdot N_G log(N_G))$ where $N_G$ is the number of $G$-points included in the truncation. Due to the orthogonality of the wavefunctions rapid oscillations occur near the atomic sites for the valence single-particle orbitals. These sharp features require a greater number of plane-wave basis functions to describe, increasing the computational cost of the calculation. By freezing the core electrons of the system it is possible to reduce this cost, associated with a high $G$-point truncation, and the overall cost by reducing the number of electrons that need to be explicitly treated. This is known as the frozen core approximation and assumes that the core states are localised within a certain radius of the atom and are invariant to the environment. This allows for the creation of pseudo-potentials that result in a smooth wavefunction inside this radius whilst matching the all-electron wavefunction further away from the nucleus.

### Projector Augmented Wave Method

By only matching the pseudised wavefunction, $\tilde{\psi}_n(\mathbf{r})$, to that of the all-electron wavefunction, $\psi_n(\mathbf{r})$, outside the cutoff radius, $r_c$, information within the core region is lost. The PAW method applies a linear transformation to the wavefunction in this region, meaning this information can be recovered.[61] To do this the augmented region is described in a separate, atom-centred, radial basis set which the true all-electron wavefunction is expanded in giving the all-electron, $\phi_\nu^a$, and smooth, $\tilde{\phi}_\nu^a$, partial waves – for each augmentation sphere $a$.

$$\psi_n(\mathbf{r}) = \tilde{\psi}_n(\mathbf{r}) + \sum_a \sum_\nu \left(\phi_\nu^a(\mathbf{r}) - \tilde{\phi}_\nu^a(\mathbf{r})\right) \langle \tilde{p}_\nu^a | \tilde{\psi}_n \rangle \tag{3.43}$$

The smooth projector functions, $\tilde{p}_\nu^a(\mathbf{r})$, are choosen to satisfy

$$\sum_\nu |\phi_\nu^a\rangle \langle \tilde{p}_\nu^a| = 1 \tag{3.44}$$

for each augmentation sphere, as there is no overlap of core regions. Note that to not affect the wavefunction outside the augmented core $\phi_\nu^a(\mathbf{r}) = \tilde{\phi}_\nu^a(\mathbf{r})$ for $r > r_c$.

## 3.3.3 Geometry Optimisation

The Born-Oppenheimer approximation allowed the treatment of atomic nuclei as a fixed external potential, however the position of these ions is not always known. With atoms in their optimal position the stress upon a crystal and force upon the atoms is zero. The force on the atoms are calculated, using the Hellmann-Feynman theorem,[62–65] as the derivative of the total energy with respect to atomic positions,

$$\mathbf{F}_j = -\frac{\partial E}{\partial \mathbf{R}_j} = \langle \Psi_0 | \frac{\partial \hat{\mathcal{H}}}{\partial \mathbf{R}_j} | \Psi_0 \rangle \,. \tag{3.45}$$

There are many different geometry optimisation algorithms for iteratively updating atomic positions; methods like conjugate gradient are robust yet often require many steps to pin point the minima,[66] where as quasi-Newton methods[67] approximate the Hessian matrix for iteration history led minimisation, for faster convergence, however it is unstable with atomic positions far from equilibrium. It is possible to reduce the degrees of freedom available to optimiser by constraining the lattice or even atomic positions. This is particularly important when modelling surfaces of crystals as the surface should be allowed to reconstruct whilst still maintaining the lattice parameters in the bulk of the material. This is achieved by fixing the lattice vectors describing the periodic cell containing the surface slab.

### 3.3.4 Surface Calculations

Surfaces are created when bulk crystals are terminated and is the place where the material can interact with gaseous or liquid environments. The modelling of these surfaces is complicated by the periodic boundary conditions introduced in Sec. 3.1.7. To combat this when studying surfaces a slab model is created that exposes two, preferably symmetrically identical, surfaces separated by a vacuum gap as depicted in Fig. 3.3.

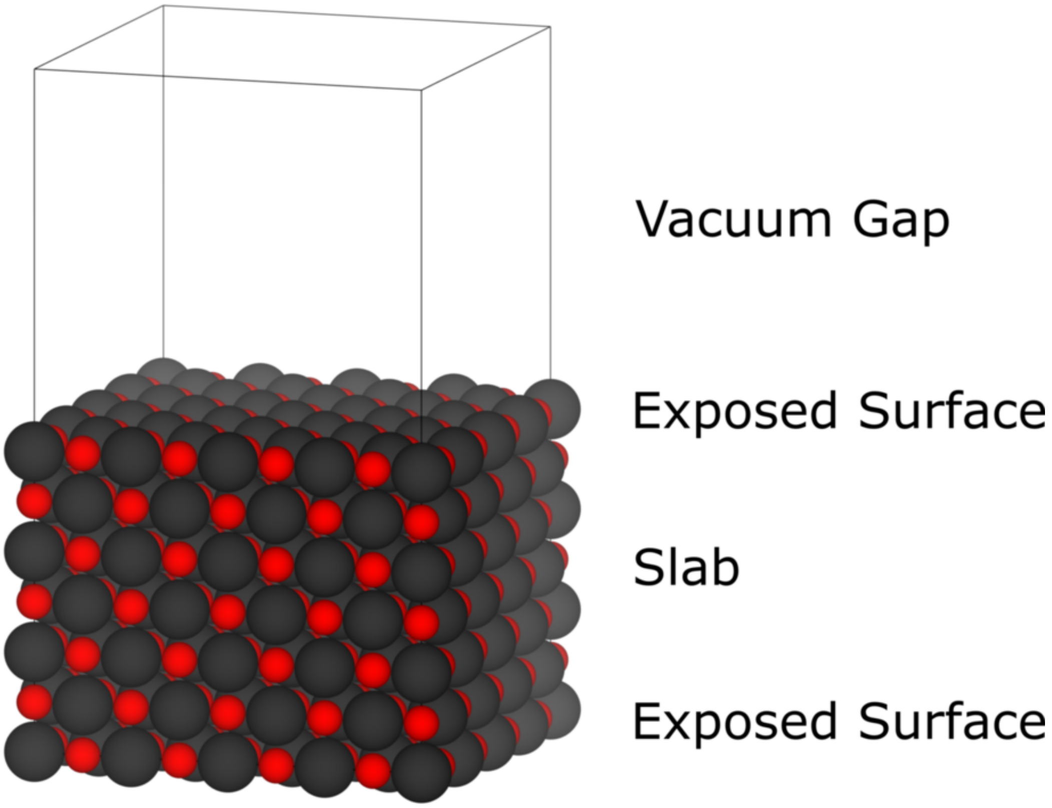

**Figure 3.3:** An example surface slab model for a (100) surface of a rock-salt crystal. Anions are shown in red whilst cations are depicted in black. The cell is shown by a thin black line which due to periodic boundary conditions is tessellated infinitely in each lattice direction. This exposes the bottom surface of the slab as well as the top surface to the vacuum gap.

Due to the change in environment for the surface atoms, upon geometry optimisation, a reconstruction occurs. The energy per unit area associated with this relaxation is known as the surface energy, $\gamma$. Using a surface slab with equivalent surface terminations, as is done for each surface calculation in this thesis, the surface energy is defined as,

$$\gamma = \frac{1}{2A}\left(E_{\text{slab}} - \frac{N_{\text{slab}}}{N_{\text{bulk}}}E_{\text{bulk}}\right), \tag{3.46}$$

where $E_{\text{slab}}$ and $E_{\text{bulk}}$ are the total energy of the slab and bulk systems respectively. $N_{\text{slab}}$ and $N_{\text{bulk}}$ are the number of atoms in the slab and the number of atoms in the bulk calculation respectively whilst A is the area of the exposed surface. The factor $\frac{1}{2}$ is due to the exposure of two surfaces to vacuum gap and assumes the two surfaces have relaxed in an identical way.

To aid the relaxation of the two surfaces happening in a symmetrical manner it is important to put distance between the two surfaces. This should be done both in terms of crystal between the surfaces inside the slab and vacuum outside the crystal. This ensures that the surfaces do not interact with each other during the relaxation. However this comes with computational cost as adding more bulk like crystal between the surfaces increases the number of atoms and, consequently, the number of electrons in the system. Furthermore the vacuum gap, despite not increasing the number of electrons, increases the number of basis functions required for the calculation when using plane-wave basis functions.

As molecules interact with a surface the energy released as it is adsorbed is called the adsorption energy and is calculated as,

$$E_{\text{adsorption}} = \frac{1}{N_{\text{molecules}}}\left(E_{\text{molecule/slab}} - E_{\text{slab}} - N_{\text{molecules}}E_{\text{molecule}}\right). \tag{3.47}$$

In this equation $N_{\text{molecules}}$ is the number of molecules in the calculation, showing that the adsorption energy has a dependence on the coverage of the surface. $E_{\text{molecule/slab}}$ and $E_{\text{molecule}}$ are the total energy of the molecule adsorbed on the slab and the total energy of the isolated molecule. As the molecules on used in this thesis have a dipole associated with them for all the calculations molecules were adsorbed on both surfaces of the slab on equivalent sites.

### 3.3.5 Vibrational Modes

Vibrational modes can be used to characterise adsorption sites of surfaces and as such can be a useful way to link the simulation with experiment and validate predictions.

It is possible to to access these modes by calculating the Hessian matrix,

$$H_{ij} = \frac{1}{\sqrt{m_i m_j}} \frac{\partial^2 E}{\partial R_i \partial R_j} \tag{3.48}$$

where $m_i$ is the mass of the atom positioned at $R_i$. This may be calculated using finite differences, displacing each ion by a small amount in the direction of each Cartesian coordinate. Once calculated the vibrational modes correspond to the eigenfunctions of the Hessian and their frequencies are the square roots of the eigenvalues. These calculations can be very expensive for systems with a large number of atoms but by only calculating a partial Hessian this cost can be reduced. This approximation is only valid when the specific modes of interest are localised subset of atoms. In this case the other atoms can be ignored in the calculation of the Hessian, effectively assigning them an infinite mass.

# CHAPTER 4

# PREPARATION OF POLAR NICKEL OXIDE THIN FILMS VIA MOLECULAR BEAM EPITAXY

The successful epitaxial growth of NiO (111) films is realised via MBE and characterised using RHEED and AFM. The thin films show dual domains, $[1\bar{1}0]$ and $[\bar{1}10]$, within the crystal as grown. The second domain, $[\bar{1}10]$, falls in prominence as the samples are annealed at increasing temperature in air. The annealing also decreases the roughness of the film's surface. DFT is used to study the formation of the second domain and it is shown to be bound by $\{111\}$ planes and form from intermixing at the interface driven twinning.

## 4.1 Introduction

This chapter discusses the growth of (111) NiO films and the impact of post-growth annealing on surface roughness and crystal quality. Nickel oxide is a material of interest for clean energy generation, such as hydrogen production and storage to photovoltaics.[68–74] For many of these applications, the ability to control the surface structure of NiO directly affects the ability of the film to perform its task. During its role as a catalyst, in hydrogen production, the surface roughness plays an active role leading to increased activity. This same characteristic in solar cell results in low coordination at the interface, often leading to charge trapping, reducing the films quality and subsequently reducing device performance.[75]

The task of growing NiO in the (111) direction is complicated by the polar nature of this orientation. As a Tasker type 3 surface, alternating single species layers build up an electrostatic potential across the film.[5] As discussed in Chapter 1, a redistribution of charge, via geometrical reconstructions or by adatoms such as hydrogen, is required to stabilise this divergent electric field. DFT studies on MgO have also shown that 3D island growth is preferential, due to this phenomenon, with the formation of new atomic layers preferential to formation of complete layers.[4] Similar behaviour is expected in NiO.

By combining several surface and film structure techniques, as well as a theoretical study, this chapter will examine the dynamics of single and multigrain crystal structures of NiO films grown eptixially on MgO (111).

## 4.2 Methods

### 4.2.1 Substrate Preparation

The films presented in this chapter were grown epitaxially upon (111) oriented MgO substrates. MgO is a logical choice of substrate as it has both the same lattice structure and oxidation state as the NiO film. The lattice parameters of the two materials are also well suited, with less than a 1% lattice mismatch. The MgO substrates were bought from MTI Corp, and their surfaces were prepared *ex-situ* in an image furnace. This equipment was used as it is better suited to high temperature gradients, with respect to time, than conventional ceramic furnaces.

The temperature was increased from room temperature to 1100°C at a rate of

100°$C$/min. This temperature was then held for 30 minutes and cooled at the same rate back to room temperature. The furnace is water cooled to aid with the cooling rate. However, it should be noted that the cooling rate is the rate of the set point temperature, and not the slower rate at which the substrate cools. The annealing process was carried out in an open atmosphere and the samples, once completed, were transferred into the MBE chamber. After the sample was degassed, RHEED was used to characterise the substrate quality.

### 4.2.2 Film Growth

The samples discussed in this chapter were prepared via MBE, as discussed in Chapter 2, in a chamber with a base pressure of $9 \times 10^{-10}$mbar. Films of 15nm thickness were produced in room temperature conditions at a 2.5 Å/min deposition rate. This rate was measured using a QCM placed in the position of sample stage, which was then removed as the sample stage was manoeuvred into position for deposition. A Ni source, in a standard effusion cell, was operated at 1300°C and a $6 \times 10^{-6}$mbar molecular oxygen pressure was set. The two sources were active at the same time for co-deposition, which has been shown to yield similar results to that of alternating anion and cation deposition for NiO and other materials of similar composition.[68] Post-growth, the sample was left in the oxygen atmosphere for 20 minutes before RHEED was again used to capture the surface conditions of the film.

### 4.2.3 Annealing

Once removed from the chamber, the samples underwent annealing in an image furnace for a series of temperatures. Using the same ramping rate as the substrate preparation, the films were subjected to 400°C, 600°C and 800°C temperatures for 30 minutes. The annealing was once again done in atmospheric conditions, and the samples were returned to the chamber for RHEED characterisation on completion.

### 4.2.4 Atomic Force Microscopy

The topography images of NiO (111) films in the chapter were collected using the AFM methods discussed in Chapter 2. Measurements of the roughness have been calculated across the entire scan area. The roughness is a moment-based quantity of the data and is calculated from the 2nd central moment where the *i*-th moment is defined as,

$$\mu_i = \frac{1}{N}\sum_{n}^{N}(z_n - \bar{z})^i. \tag{4.1}$$

Here, N is the total number of pixels in the image and $\bar{z}$ is the mean value of all the pixels. From this the RMS-roughness, $R_q$, is calculated as

$$R_q = \sqrt{\mu_2}. \tag{4.2}$$

### 4.2.5 Density Functional Theory

The VASP[76] code for running DFT calculations was used, along with the PAW pseudopotentials that are supplied with the package.[61] An effective U-value of 5.3 eV was applied to the *d*-orbitals of Ni, taken from the literature using the same pseudopotentials.[57] This value was optimised against multiple parameters, such as magnetic ordering and phase stability. Further examination of the choice of U-value is explored in Chapter 5. A planewave cut-off of 450eV was used along with a k-point spacing of 0.05 $2\pi\text{Å}^{-1}$, corresponding to a grid size of $6 \times 3 \times 1$. The interfaces were built in fully periodic supercells containing 6 anion-cation bi-layers per grain. Within these cells were a single interface with the second boundary of the grain being exposed to vacuum. To combat the polar nature of the exposed surface 50% of the oxygen atoms in the terminating oxygen layer were removed. The vacuum gap between the surfaces of each grain was 12Å. Convergence graphs for planewave cut-off, k-point spacing and vacuum gap are given in Appendix B.

During geometry optimisation of the cells, only the positions of the ions were relaxed with the lattice parameter in the lattice directions parallel to the surface fixed at 4.24 Å, the self-consistent value for MgO. This indicates the NiO was under a 1% strain, whereas in reality this strain would likely be relieved via misfit dislocations at the interface. The supercell was twice as large in the x direction as to accommodate removing 50% of the surface oxygen. An interface formation energy, $\gamma_{\text{interface}}$, was calculated in a similar fashion to a surface energy, as described in Chapter 3,

$$\gamma_{\text{interface}} = \frac{E_{\text{interface}} - E_{\text{bulk}}}{A}, \tag{4.3}$$

where, as the grains are terminated by vacuum, the number of atoms in the interface and bulk cells are equal, and A is the surface area of the interface. As the bulk cells also contain the 12Å vacuum gap, the surfaces evident on the opposite sides of the boundaries are also apparent in these cells. The distance between these surfaces and the interface was chosen to be large enough such that, with the addition of cation mixing at the boundary, the difference in interface energy is less than 0.01 J/m$^2$.

## 4.3 Film Growth

### 4.3.1 Reflection High-Energy Electron Diffraction

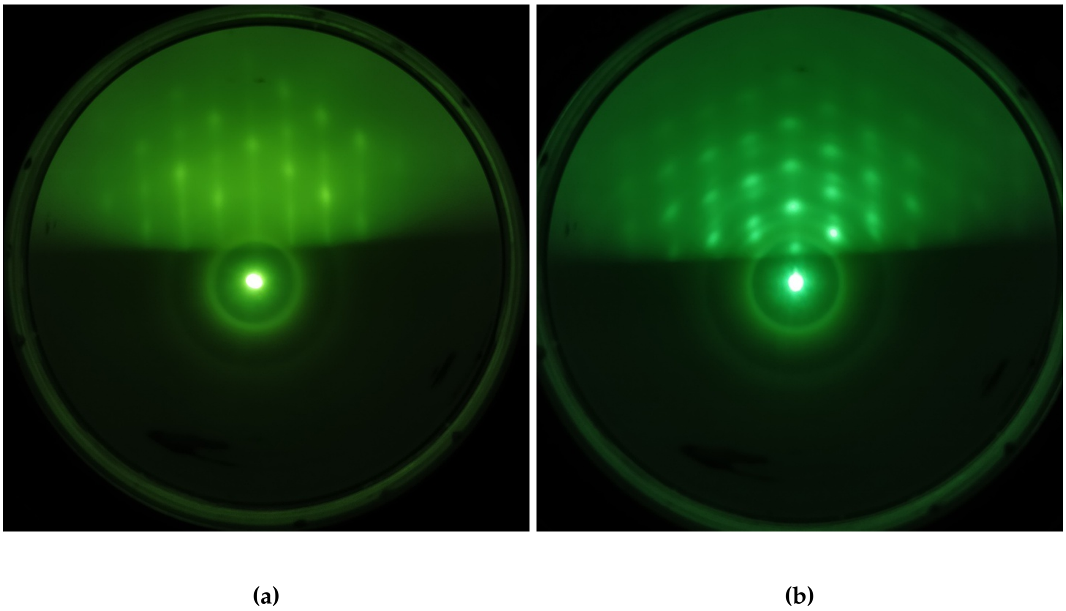

**(a)** **(b)**

**Figure 4.1:** RHEED patterns of surfaces of the MgO (111) substrate, shown in a), and, in b), as grown NiO (111). Both images are captured down the $[1\bar{1}0]$ crystal direction of the substrate. The RHEED gun is operated at 15 kV and a glancing angle of 4°.

The preparation of MgO (111) substrates via *ex-situ* annealing produced substrates of high quality. This can be seen in Fig. 4.1 as the streaks in the RHEED pattern indicate the substrates are flat. The lack of features between the main order streaks further imply an unreconstructed surface. From the spots in the image it is clear that there is only one domain, confirming the alignment of the incident beam with the $[1\bar{1}0]$ direction of the crystal. This is indicative of the substrate conditions for all four of the samples used in this study.

Likewise, the second image in Fig. 4.1 is an example of the RHEED pattern for the thin films as grown. Here the image is showing transmission spots through the 3D islands that have formed on the substrate. It is theorised that circular fringes, faintly visible between the spots in the image, are indicative of sharp reconstructions

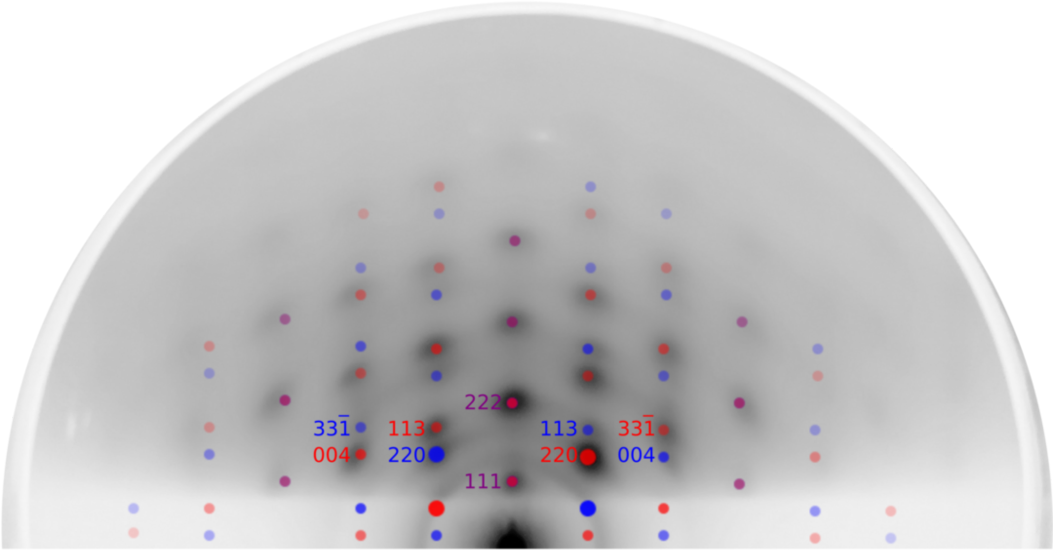

**Figure 4.2:** RHEED image of as grown sample from Fig.4.1 overlaid with simulated diffraction patterns. The diffraction patterns are for a NiO crystal along the $[1\bar{1}0]$ (red) and $[\bar{1}10]$ (blue) and were produced using jems software.[77] Both patterns have been aligned such that the [111] direction is normal to the surface of the film.

of surfaces that occur over 3 or more layers.[78] Also of note is the mirroring of the spots across the central vertical line. This is consistent with electron diffraction of multiple domains; the $[1\bar{1}0]$ domain, which is grown epitaxially on the surface, and a $[\bar{1}10]$ domain, hinting at the presence of twinned grain boundaries or stacking fault growth. This has been seen before with NiO (111) growth via passive Ni (111) exposure to air at room temperature.[79]

This is illustrated in Fig. 4.2 where the diffraction patterns of these two 180°rotated domains are superimposed on the RHEED pattern from Fig. 4.1b. The prominence of the transmission spots relating to the $[1\bar{1}0]$ domain indicate that the domain matched epitaxial growth dominates.

### 4.3.2 Density Functional Theory

To investigate the origin of the twin domain formation, three interfaces between MgO and NiO were constructed, an epitaxial growth, cation mirrored and anion mirrored. The same interfaces were then converted into grain boundaries within a NiO crystal. The interfaces of these six structures, along with three mixed interface structures for the anion mirrored structure, are shown in Fig. 4.3. Here cation mirrored relates to a (A, B, C, B) cation stacking, and visually the final cation layer in the substrate is the mirror plane for the boundary. Whereas the anion mirrored structure describes a oxygen layer mirror plane and a cation stacking of (A, B, C, C). By using the epitaxial

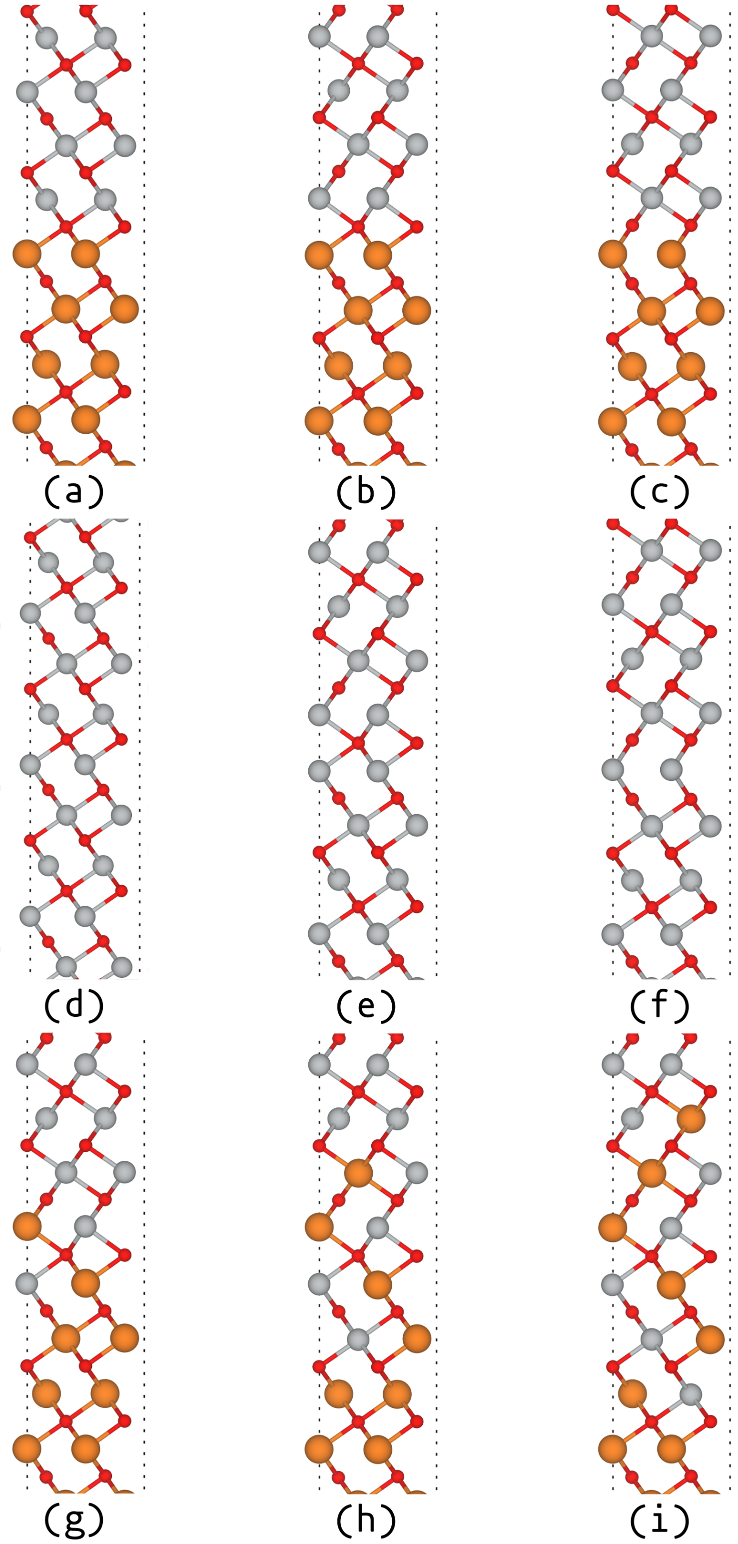

**Figure 4.3:** The structures of the interfaces for MgO | NiO, NiO | NiO and mixed NiO | MgO. Ni is shown in grey, Mg is orange whilst O is displayed as red. The structures in (a), (b) and (c) are repeated as entirely NiO in (d), (e) and (f), respectively. The structures in (a) and (d) are the epitaxial continuation of the grain whilst (b), (e) and (c), (f) are cation mirrored and anion mirrored, respectively. The mixed interfaces, (g), (h) and (i) are built from the anion twinned structures and retain a spin structure consistent with these.

structures for the MgO | NiO interface and NiO | NiO interface as the bulk reference in calculation of the respective interfacial energies via Eqn. 4.3, it is possible to compare the likelihood of second domain's origin. These energies are given in Table 4.1. The cation mirrored structures are far higher in energy than those that are anion mirrored in both the MgO | NiO and NiO | NiO interfaces. As such, only this configuration is considered for the mixed interfaces. In each of the mixed interfaces a chequerboard pattern of atomic mixing is preferred, with the spin of the nickel atoms maintaining their anti-ferromagnetic ordering across (111) layers. It is clear to see that the domain is mostly likely to be formed within the NiO crystal itself, as oppose to an abrupt interface between substrate and film. However, the introduction of cation mixing at the interface changes this with two layers of mixing being more favourable than the NiO | NiO twin and with three layers of mixing the twinned interface has an energy cost comparable to the untwinned growth. This shows why the second domain is often seen in regions of high intermixing as the energetic cost of the twin is so low.

| Interface Type | Interface Formation Energy (J/m$^2$) | |
|---|---|---|
| | Cation Mirrored | Anion Mirrored |
| NiO \| NiO | 1.03 | 0.28 |
| MgO \| NiO | 1.78 | 0.49 |
| 1 Layer Mixed MgO \| NiO | – | 0.35 |
| 2 Layer Mixed MgO \| NiO | – | 0.20 |
| 3 Layer Mixed MgO \| NiO | – | 0.06 |

**Table 4.1:** Interface energies for the symmetrically inequivalent stacking of the two domains. The cation mirrored structures for the mixed configurations were not calculated due to the higher energy cost in both the MgO | NiO and NiO | NiO interfaces.

The magnetic ordering of the nickel atoms was considered with the values presented in Table 4.1 being the lowest energy spin configuration for each structural permutation considered across the three levels of mixing. For each structure a range of spin configurations were explored, an example of such structures and their associated energies are shown in Fig. 4.4. Whilst the figure shows only the three layer mixed structure the lowest energy ordering is the same between all of the mixing options and mirrors the magnetic structure of the bulk material, anti-ferromagnetic ordering along the (111) planes.

Due to the periodicity of the cell the calculation is not able to explore more disordered spin configurations however the strong preference for maintaining the same ordering as the bulk crystal shown in the configurations sampled suggest that this would be unnecessary. A more stable structure or spin configuration would only lower the

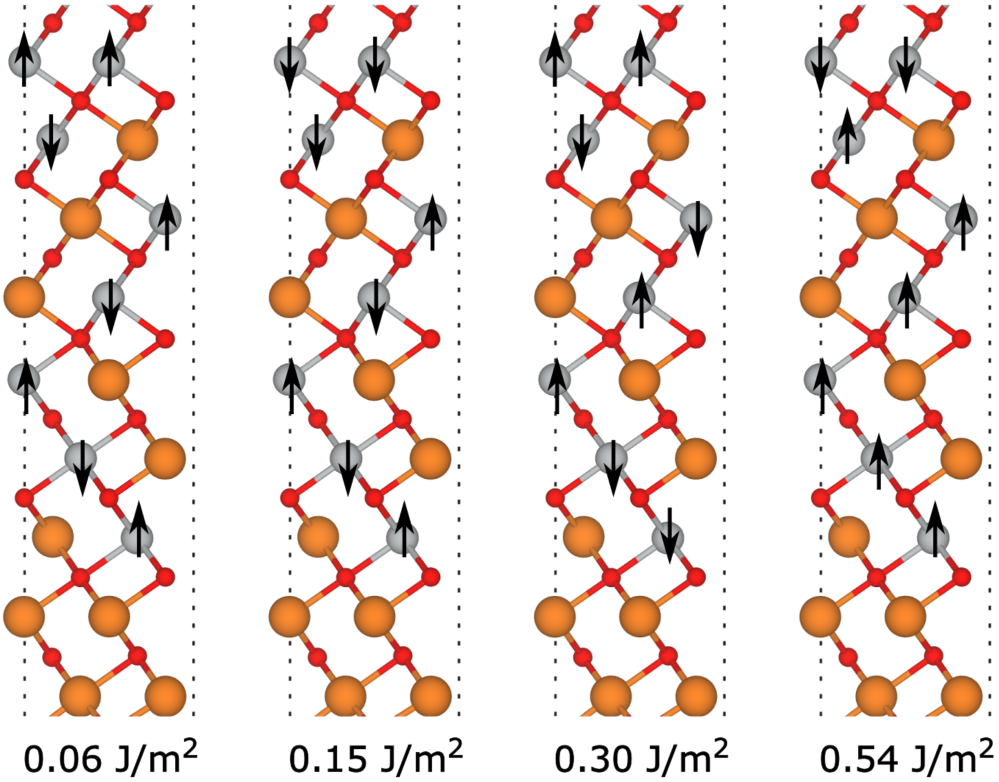

**Figure 4.4:** A selection of different spin configurations for the three layer mixed structure and their associated interface energies. The arrows on the image represent the spin of the atom they are overlaying, either up or down, atoms without an arrow have no moment associated with them. The ordering that follows the bulk magnetic structure, anti-ferromagnetic across (111) planes, is shown to be the lowest energy solution, which is the case for all levels of mixing. Also shown is the same ordering of the spin within the mixed region with the spin in the non-mixed having been flipped as well as coupling of the layers such that two layers in the mixed region now form a plane of spin. Finally the mixed region being ferromagnetic and the non-mixed retaining its anti-ferromagnetic structure is shown and has the highest energy of all the structures.

level of intermixing required to make the twinning favourable.

In Fig. 4.5 an example of the NiO $[\bar{1}10]$ | MgO $[1\bar{1}0]$ interface is shown. The interface displays the anion mirroring structure predicted by the DFT+$U$ calculations, as highlighted via Fast Fourier Transform (FFT) filtering in the top right of the image. The FFT filtering was performed by isolating the (111), $(\bar{1}\bar{1}\bar{1})$, $(11\bar{1})$, (003), $(00\bar{2})$ and $(\bar{1}\bar{1}2)$ spots of both domains in the diffractogram and performing an inverse FFT. Additionally, it is shown that the mixing of the cations around the boundary, as showcased by the brighter Ni atoms appearing below the interface, is present. This is highlighted in the bottom right of the image with the varying contrast of the atomic layers indicating mixing across interface. Paired with the DFT+$U$ calculations this shows the promotion of the second domain with interfacial mixing of cations.

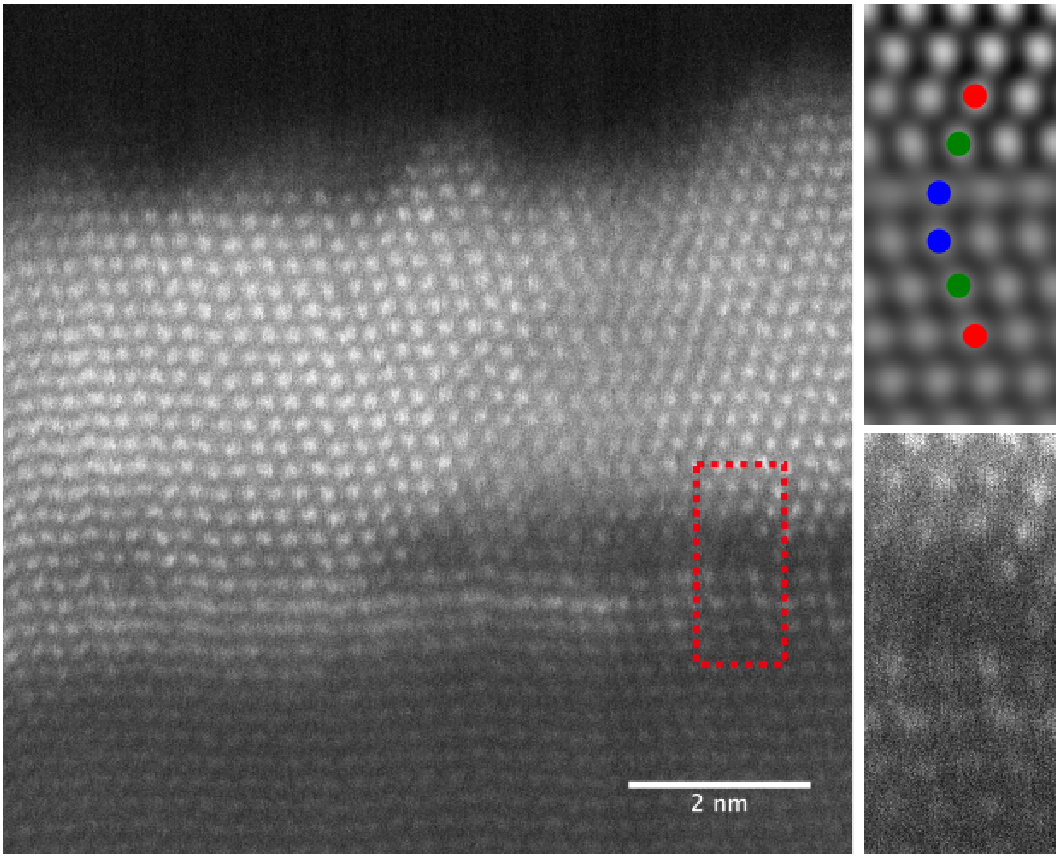

**Figure 4.5:** A HAADF STEM image of Pulsed Laser Deposition (PLD) prepared NiO Film grown on a MgO (111) substrate displaying a [$\bar{1}$10] domain. The film was grown by collaborator, Dr. Kosuke Matsuzaki, at the Tokyo Institute of Technology, Japan and imaged by Dr. Leonardo Lari at the University of York. A region, marked by a red dashed box is blown up to highlight the interface. A FFT filtered image clearly shows the anion mirrored (A, B, C, C) structure and the contrast variation within the enlarged unfiltered image indicates interfacial mixing.

## 4.4 Annealed Films

### 4.4.1 Surface Structure

#### Reflective High-Energy Electron Diffraction

Fig. 4.6 shows the RHEED patterns for the 400°C, 600°C and 800°C annealed thin films. The film corresponding to the 400°C anneal is very similar to the as grown sample with 3D island growth, indicated by transmission spots, and multiple domains prominently still visible. These spots are sharper than the as grown sample however, thus indicating less inelastic scattering of the beam at the surface; the surface whilst still rough has greater periodicity over the beam area. Additionally, circular fringes are still evident whilst faint vertical streaks indicate areas of flatness among the grains. These vertical streaks become more pronounced throughout the series of images as annealing temperature increases. This means larger areas of the samples become dominated by atomically flat planes. From the 600°C anneal the samples no longer exhibit the circular fringes, indicating a lower level of surface roughness with less atomically sharp facet features, and the 800°C sample is free of transmission spots suggesting the film is flat. Furthermore, the 600°C anneal also displays a lack of the dual domain structure. This indicates that the sample is single crystalline.

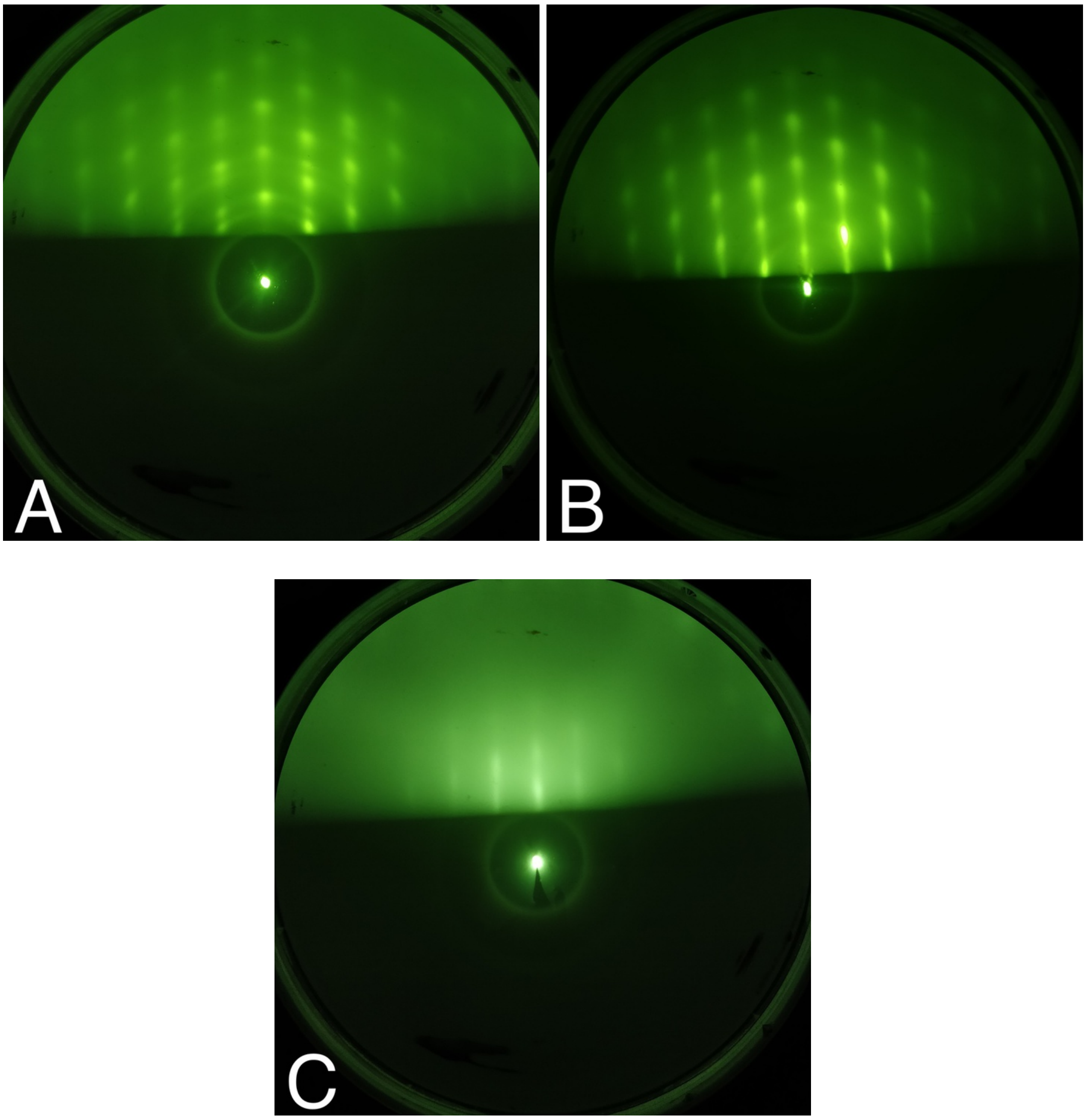

**Figure 4.6:** RHEED patterns of the annealing series of samples. (A) shows 3D island growth producing transmission spots from RHEED for the 400°C anneal. The spots are still visible in (B), which corresponds to the 600°C anneal, yet are not apparent in (C), the anneal at 800°C. All images are taken with the <110> zone axis incident in the azimuth direction. The RHEED gun is operated at 15 kV with a glancing angle of 4°. The chamber in which the measurements were taken in had a base pressure of 9E-9 mbar and the surfaces have had no treatment other than the *ex-situ* anneal.

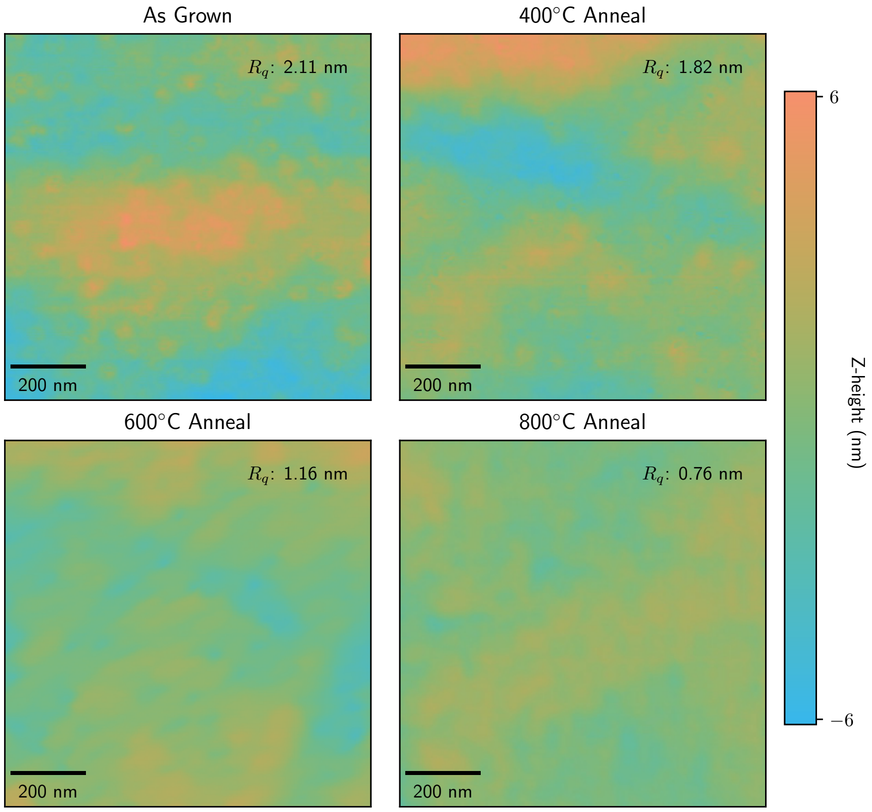

**Figure 4.7:** AFM images of the four samples in the annealing series. All images have a scan size of 256x256px and 0.5x0.5$\mu$m dimensions. The height profiles have been adjusted so that the 0 z-height is the centre of the z-range for each image. The same range of the colour scale has been used for each image and is an isoluminant colour map from the python package colorcet.[80]

The implication of these patterns is that as the annealing temperature is increased the surface becomes smoother and the crystal more ordered, with the energy from the anneal able to re-crystallise the samples. As there are no minor streaks between the main lines, the RHEED data shows no evidence of $p(2 \times 2)$ or $\left(\sqrt{3}\times\sqrt{3}\right)$R30° reconstructions. This suggests that the surfaces, where flat, are stabilised through hydroxylation.

### Atomic Force Microscopy

The surface morphology of the annealed NiO films were characterised via AFM. The respective values for the roughness are displayed, along with the $500nm \times 500nm$ images from which they were calculated, in Fig. 4.7. The slight increase in ordering, shown by the difference in RHEED images, between the as grown and 400°C samples is further evident in this figure with a reduction of the RMS roughness from 2.11nm to 1.82nm. There is a clear trend towards a smoother surface with every increased an-

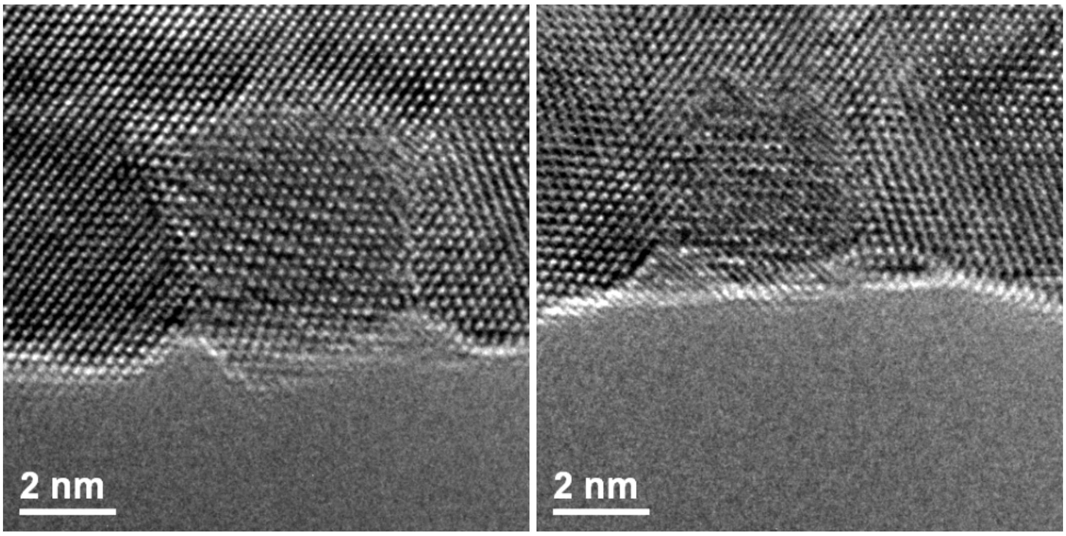

(a) (b)

**Figure 4.8:** Environmental TEM images of the evolution of the size of a, PLD-grown, NiO $[1\bar{1}0]$ grain within air. The film was grown and imaged by collaborators, Dr. Kosuke Matsuzaki and Dr. Kenta Yoshida, at the Tokyo Institute of Technology and Nagoya University, Japan. (a) shows the grain before the introduction of the air whilst (b) shows the same location after 11 minutes and 12 seconds. The grain is bounded by $\{111\}$ planes in (a) and shows evidence of a faceted surface. This surface is much flatter in (b) and the domain has shrunk whilst maintaining the $\{111\}$ boundaries.

nealing temperature, with the highest temperature anneal displaying a sub-nanometer RMS roughness in-line with values reported for low index non-polar surfaces of NiO grown on MgO.[81]

## 4.4.2 Crystal Structure

### Environmental High-Resolution Transmission Electron Microscopy

As shown in Fig. 4.1 & 4.6 the 400°C annealed and as grown sample comprise of 2 domains. As the annealing temperature is increased further, this twin domain structure disappears. The healing of the $[\bar{1}10]$ domain occurs through migration of the interface between the two domains. The bounds of the grain are most likely along the $\{111\}$ planes within the structure, due to the low energy cost of forming such an interface. Another interface, the $\{11\bar{2}\}$, has been considered in previous work that have noticed this dual domain behaviour.[79,82] However, this boundary was not apparent during this work and DFT calculations, performing a fully optimised scan of grain translations at this boundary, produced 2 distinct structures with the lowest formation energy, $\gamma_{\text{interface}}$, of $1.93 J/m^2$; the $\{11\bar{2}\}$ grain boundary formation energy is nearly seven times the formation energy of the most stable {111} interface and nearly twice as expensive as the less stable cation mirrored boundary.

This shrinking of the domain, by movement of grain boundaries, can be visualised by using the energy provided by the electron beam in an environmental TEM. This acts as a replacement for the infrared radiation heating of the image furnace. The introduction of air into the microscope chamber causes the reduction in size of the second domain, alongside a smoothing of the surface. This is shown in Fig. 4.8 where a {111} bounded $[1\bar{1}0]$ domain is reduced from a width of 4.3nm to 2.7nm, with a similar 40% reduction in height. From Fig. 4.8b it is evident that {111} planes still bound the domain. This complements the theoretical calculations showing that even as the domain is being healed, the preferential boundary is still lowest energy interface between the domains.

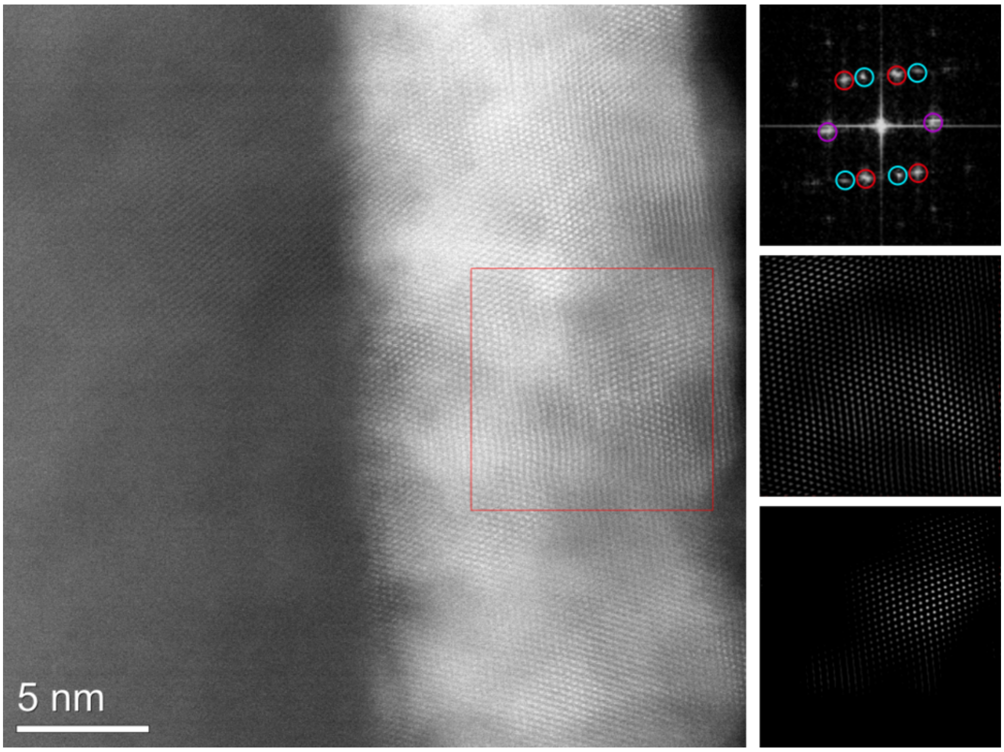

**Figure 4.9:** A HAADF image of two domains causing a Moiré pattern. Sample shown is grown via MBE and annealed at 400°C in open atmosphere. A diffractogram of the highlighted area is shown in the top right with the spots relating to the separate domains highlighted in red for the $[1\bar{1}0]$ and blue for $[\bar{1}10]$, purple indicates the shared spots. Beneath the diffractogram is the FFT filtered image for the epitaxial domain and beneath that the FFT filtered $[\bar{1}10]$ domain. The image is captured at 5M magnification with a beam energy of 200keV.

The images also provide insight into the dynamics of the annealing process; not only are the secondary domains removed, the roughness of the surface is reduced, mirroring the AFM and RHEED surface analysis presented in Section 4.4.1. Atomically sharp features, like those predicted in the as grown and 400°C annealed sample in Figs. 4.1b and 4.6a, are present in this sample and are evident Fig. 4.8a. These features are not visible in Fig. 4.8b as the surfaces likely becomes hydroxylated in the atmosphere.

### Scanning Transmission Electron Microscopy

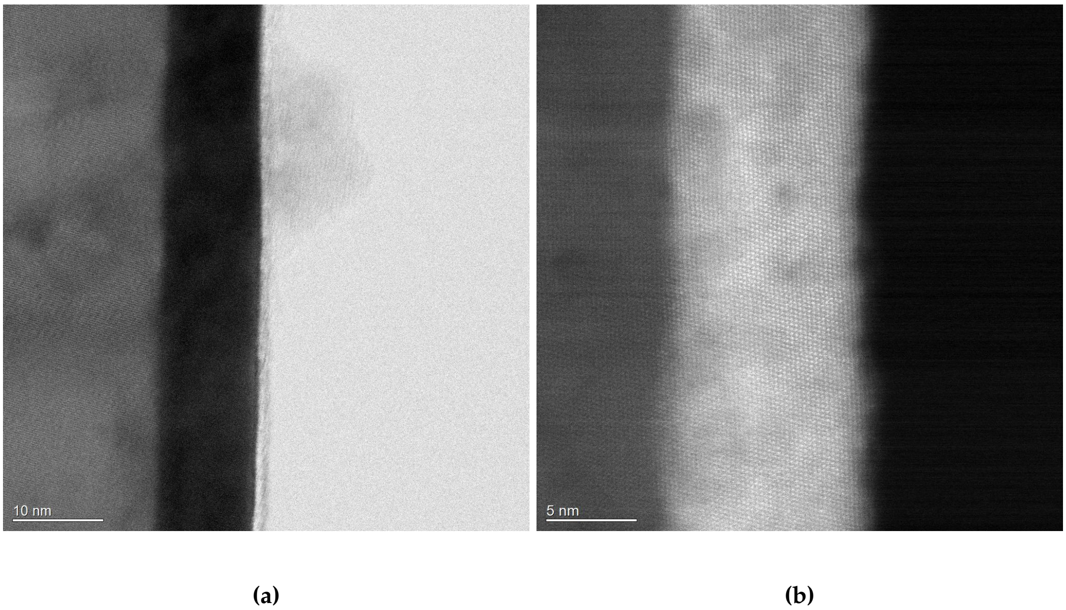

**(a)** **(b)**

**Figure 4.10:** BF-STEM, a), and HAADF, b), images of a NiO (111) film annealed at 800°C. The BF-STEM image shows a lower magnification view of the film displaying a sharp surface and single-crystal structure, free of Moiré patterns. In b) it is shown that the crystal is well ordered with a flat surface.

The crystal structure of the annealed samples was studied in a JEOL 2200FS Cs aberration corrected STEM to view the atomic positions within the film. The 400°C film is shown in Fig. 4.9, along with the diffractogram of the highlighted region and the FFT filtered images for the $[\bar{1}10]$ and $[1\bar{1}0]$ domains. The Moiré pattern in the highlighted area is a result of the combination of both domains occupying the same cross-sectional area. When analysing the diffractogram this becomes obvious and, using the simulated SAED patterns in Fig. 4.2 to isolate each domain, the underlying structure evident. Also of significance are the $\{111\}$ boundaries containing the $[1\bar{1}0]$ grain, alongside an extended boundary parallel to the [110] plane. This interface would correspond to a grain boundary between the [110] and [114] planes however is more likely a series of steps at the interface. Domains of this size were evenly distributed throughout the film and consistently evident in as grown samples. It is pertinent to note the similarity of the diffractogram to a hexagonal structure with two faint spots appearing between the zero spot and the (111). It would be an easy mistake for this Moiré pattern to be misidentified as a wurzite phase, however the FFT analysis and RHEED images show clearly this is beating between two grains.

Once at higher annealing temperatures the structure became single crystal and no longer contained any secondary domains. This is evident in Fig. 4.10a and 4.10b where the bright-field image shows a flat single crystal free of Moiré patterns and the dark-field image displays atomic resolution of a well ordered crystal.

## 4.5 Conclusions

Using MBE, NiO (111) films have been epitaxially grown upon MgO (111) substrates using molecular oxygen. These films have rough surfaces and contain both $[1\bar{1}0]$ and $[\bar{1}10]$ domains, the formation of which was driven by both cation mixing at the interface, and a low formation energy of a NiO (111) twin in the bulk. The structure of these interfaces was predicted using DFT+$U$, and compared with STEM images of the interface, displaying the correct stacking of cations around the boundary. Via FFT filtering TEM and STEM images, the interface between these domains was also shown to occur along $\{111\}$ planes, not the $\{11\bar{2}\}$ as previously stated in the literature. Through a process of annealing the samples, in an open atmosphere at increasing temperatures, the transformation from the rough dual domain film to a flat single crystal was catalogued using RHEED and AFM. The dynamics of this transformation, captured via a recreation of the annealing process in an environmental TEM, were shown to favour progression along the $\{111\}$ planes associated with the lowest formation energy interface between the domains. Moiré patterns in the films were indicative of the dual domains despite the diffractogram being easily confused with that of the wurzite structure. Finally, post-annealing in air at 800°C gave a single crystal NiO film with a surface roughness comparable to that seen on low index non-polar surfaces of NiO also grown upon MgO.

# CHAPTER 5

# CHARACTERISATION OF THE (111) SURFACE ON POLAR OXIDES

A study into the surface reconstructions required to stabilise the polar (111) surfaces in NiO and MgO is presented. It is shown that the (111) surface forms {100} facets that have lower surface energy per unit area than the currently regarded theoretically stable surface, the octopolar reconstruction. These facets are imaged, using (scanning) transmission electron microscopy, and are shown to form when grown using molecular beam epitaxy and also through a dynamical transition driven via the electron beam. This surface is then characterised theoretically via the vibrational modes of adsorption sites and compared to other surfaces that have been studied in the literature to provide a reference.

## 5.1 Introduction

In recent years the interest in the structure of polar oxide surfaces has increased, with much speculation over the termination of such surfaces.[4,9,10,18] NiO and MgO are ideal candidates for the study of these surfaces. As rocksalt structures, the two polar oxides are prototypes of magnetic transition metal oxides and paramagnetic ionic compounds that form simple crystals uncomplicated by variations in cation oxidation state. This allows for useful theoretical modelling of the surfaces to supplement experimental evidence.

Due to the polar catastrophe the (111) surface of both NiO and MgO is unstable. As mentioned in the previous chapter, this instability requires passivation through a redistribution of charge at the surface. Passivation can occur in multiple ways with the most commonly proposed being either geometrical and electronic reconstructions or surface adatoms. This chapter looks at the dynamics behind the formation of a large scale geometrical reconstruction to heal the polar catastrophe and provides characteristics of the reconstruction.

## 5.2 Methods

### 5.2.1 Sample Information

This chapter looks at data from one MgO and two NiO samples, grown via MBE. These samples will be referenced as S01, S02 and S03. A MgO (111) | SiC (0001) sample from previous work (S01) is presented alongside a NiO (111) | MgO (111) sample (S02) to display faceted termination of the (111) surfaces in both materials, formed during sample growth. S01 was grown in the same growth parameters as discussed in Chapter 4 however a 100W oxygen plasma, providing 6E-6 mbar of atomic oxygen, was utilised instead of molecular oxygen. A Mg source, in a standard effusion cell, was operated at 280°C to provide a comparable deposition rate to that previously presented. This source was active simultaneously with the oxygen plasma for co-deposition and the sample stage was held at 500°C throughout the growth. The full description of the growth parameters for S01 is given in Ref. 4. S02 was prepared as discussed in Chapter 4 however, like S01, replacing the molecular oxygen for 100W oxygen plasma, providing $\left(6 \times 10^{6}\right)$ mbar of atomic oxygen, and with the sample substrate at 500°C for the duration of the growth. Neither S01 or S02 have been subject to any post processing other than the standard cross-sectional TEM specimen preparation, discussed in Chapter 2, and as such are considered as grown.

SO3 was grown by a collaborator, Dr. Kosuke Matsuzaki, at the Tokyo Institute of Technology, Japan. The growth method for S03 was via PLD using a KrF excimer laser with a oxygen partial pressure of $2 \times 10^{-4}$. Once grown the samples were annealed at 1100°C in a $CO/CO_2$ mixture for 30 minutes. The mixing ratio $P_{CO_2}/P_{CO}$ was set to 5000, the same conditions used for the production of single crystal $Fe_3O_4$.[83] This sample was then imaged by collaborators at Nagoya University, Japan, in their aberration corrected STEM.

### 5.2.2 Computational Details

#### DFT+$U$

This chapter uses the same planewave cut-off and $k$-point spacing as Chapter 4 as well as the same effective U-value for the Ni $3d$-orbitals. This U-value has been chosen from the literature in which the value is justified by comparison to a plethora properties of NiO, including the charge distribution at a (100) surface and the bonding with a CO molecule. There are many methods for choosing an effective-U value and several different values exist in the literature for addressing different problems.

One such method is to fit the U value as to force the calculation to reproduce a band-gap that matches experiment. To do this however requires an extremely high effective-U value, $U_{eff} = 8.4$ eV. Whilst this value has been used in studies, these studies often focus on specific states within the band-gap and not on correct structure and charge distribution.

Another approach is to correct the formation enthalpy of NiO with respect to $Ni_2O_3$, a less stable compound predicted to be more stable by standard DFT. For this method a lower value of the effective-U is used, often $U_{eff} = 3.3$ eV.[84] However this method is often applied when comparing NiO with other $3d$ transition metal oxides and so the value is often chosen to be consistent across the set studied and so ranges from 3 - 5 eV.[85]

The most widely used value in the literature however is $U_{eff} = 5.3$ eV. This follows from work by Dudarev[56] and Rohrbach[57] for the Local Spin Density Approximation (LSDA) and Spin Polarised Generalised Gradient Approximation (SGGA) respectively. In these studies the properties of NiO have been used to arrive at the Hubbard-like correction. This value has the advantage of being calculated for the pseudopoten-

| | Experimental | SGGA+U |
|---|---|---|
| $E_g$ (eV) | $4.2^a$, $3.8^b$ | 3.0 |
| a (Å) | $4.17^a$ | 4.20 |
| m ($\mu_B$) | $1.66^c$, $1.77^d$ | 1.69 |
| B (GPa) | $205^a$ | 203 |

[a] Ref. 86
[b] Ref. 87
[c] Ref. 88
[d] Ref. 89

**Table 5.1:** Experimental and calculated properties of NiO. The calculation is using a $U_{eff} = 5.3$ eV. $E_g$ is the bandgap of NiO whilst m is the magnetic moment of a Ni atom in the material. B and a are the bulk modulus and lattice constant respectively, these values were found computationally via fitting of a Birch-Murnaghan equation of state.[90]

tials used in this study also.

### Surface Slabs

Surface slab models were created for the (100) surface and three terminations of the (111) surface; OH terminated, octopolar reconstructed and faceted. Each slab was separated from its periodic repeat by a vacuum gap of 15Å. Doing this exposes two surfaces to the vacuum, the top and bottom of the slab, and consideration was taken to ensure that the exposed surfaces were equivalent. The region between these exposed surfaces contained enough layers such that the surface energy of the structure was converged to a tolerance of $1 \times 10^{-3}$ eV/Å$^2$. For the (100) surface a (4×4) supercell of the Fm-3m unit cell was used for comparable coverage to the faceted (111) surface which is a p(4×4) reconstruction. For the octopolar and OH terminated structures a p(2×2) sized cell was used.

### Molecular Adsorption

For the adsorption of CO molecules a molecule was adsorbed onto each exposed surface. Rotational symmetry around the centre of the surface slab was maintained as to ensure that no dipole was formed in the cell. The molecules were geometrically optimised to a force tolerance of $1 \times 10^{-2}$eV/Å.

### Vibrational Frequency

Vibrational frequency calculations were performed using the non-symmetry reduced finite difference approach implemented in the VASP[76] software package. Four displacements were made in each Cartesian direction for the CO molecule whilst the rest of the atoms were fixed in place.

## 5.3 Transmission Electron Microscopy Evidence

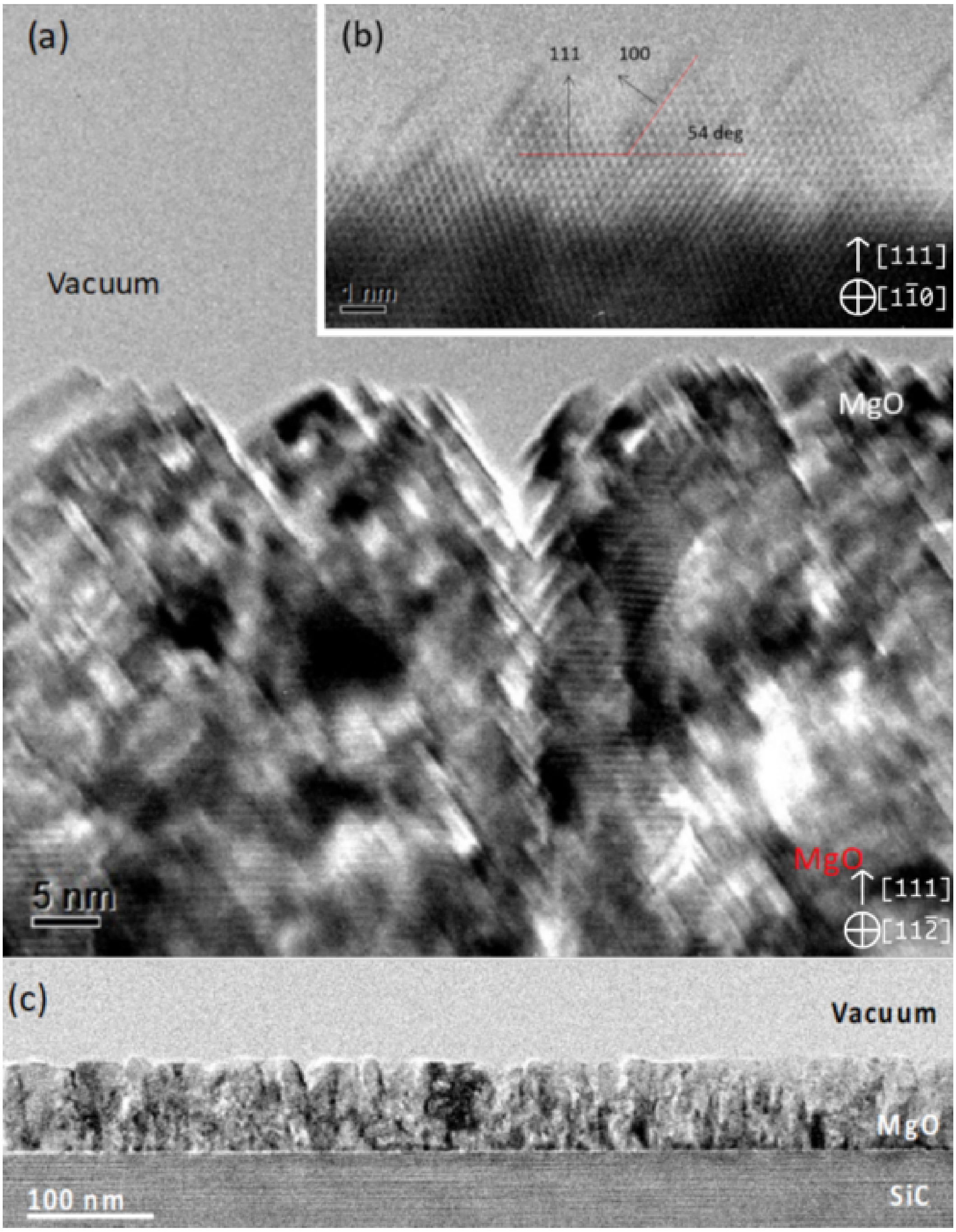

**Figure 5.1:** TEM images of a MgO(111) thin film grown at high substrate temperature, wherein (a) a bright field TEM image shows faceting of the film surface with nanometre scale features, (b) a High Resolution TEM image of the faceted surface showing the angle between faceted planes and the (111) orientation and (c) a bright field TEM image recorded at reduced magnification showing non-pillar like structures that extend to the interface showing 3D growth of the MgO(111) thin film. This image and caption is used from Ref. 4.

The surface structure of the S01 film is shown in Fig. 5.1 and displays clear evidence of {100} facets. This is further emphasised in Fig. 5.1b where, viewed down the $[1\bar{1}0]$ zone axis, the angle between facet and surface normal shows the expected 54.7° between [001] and [111]. These {100} facets form pyramid structures on the surface, several nanometres in scale as highlighted in Fig. 5.1a.

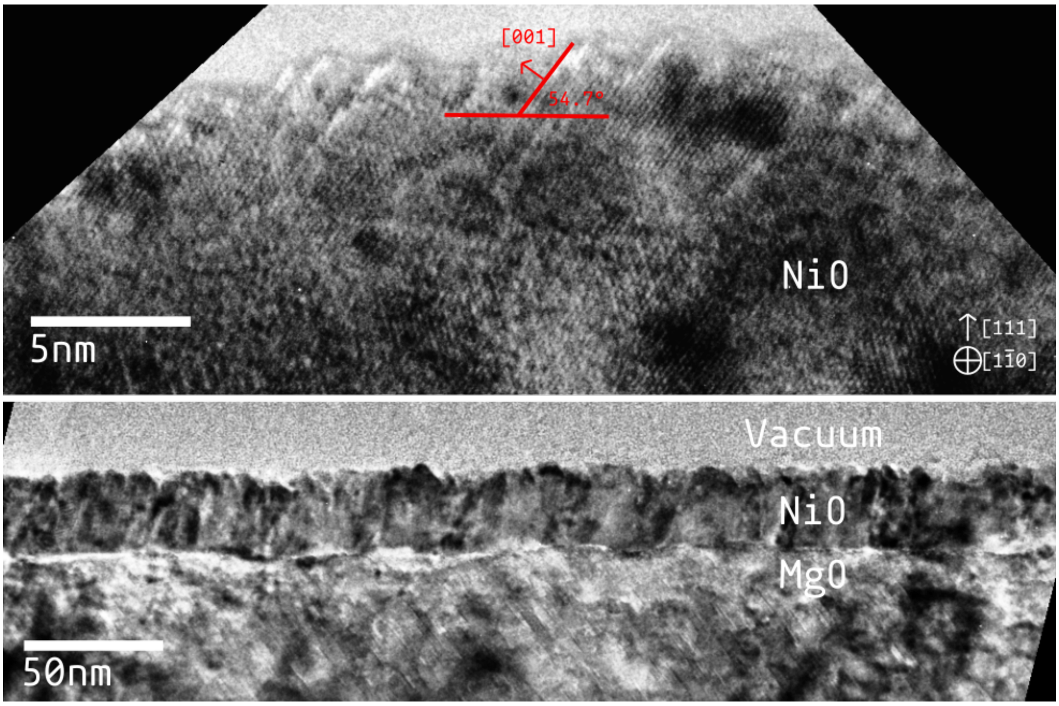

**Figure 5.2:** TEM images of a NiO (111) film grown on MgO (111). The first image shows nanometre scale features on the surface. These features are {100} facets, shown by the angle facet with the (111) surface, creating pyramid like structures. The second image is a lower magnification TEM image of the same film showing extended vertical grains similar to what is shown in Fig. 5.1. Both images are viewed down the $[1\bar{1}0]$ miller direction.

This surface structure is also evident in Fig. 5.2 which displays TEM images of S02. Highlighted again is the angle of the facets with the surface, showing that the exposed planes are {100} surfaces. A noticeable difference between the two films is the smaller scale of the pyramid features on the S02 sample compared with S01. This provides a higher concentration of low coordinated surface sites as there is less facet surface area. One possible cause of this is the difference in film thickness between the samples with the thicker film having larger reconstructions. Comparing the lower magnification image from Figs. 5.1 & 5.2 it is clear that the film structure of the two samples is similar, with both displaying long thin vertical grains. This film structure is consistent with island growth which is shown clearly in the transmission diffraction pattern captured by RHEED in Fig. 5.3.

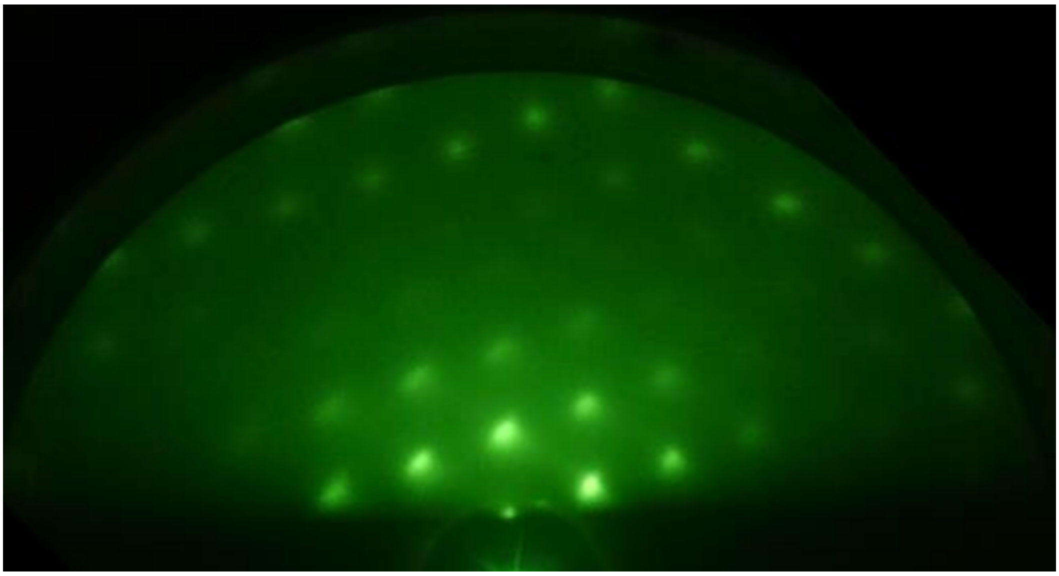

**Figure 5.3:** RHEED images of a NiO (111) film grown on MgO (111). The RHEED pattern indicates 3-dimension surface islands as Bragg condition transmission spots are clearly visible. This correlates with the low magnification image in Fig. 5.2 showing that the growth mechanism of S02 is indeed island growth terminated with {100} facets.

Whilst both of these samples, S01 and S02, show evidence of faceted termination on as grown polar oxide surfaces, S03 shows evidence of transitions to a faceted reconstruction from a rough, disordered surface driven by beam irradiation. This is shown in Fig. 5.4a where an initial image shows little faceting, followed by Fig. 5.4b, taken after the electron beam has been incident on the area for a prolonged period of time. The transition from a disordered surface to a faceted one indicates that the beam is interacting with the surface, driving the reconstruction.

A higher magnification HAADF image of the same region is analysed in Fig. 5.5 showing the same {100} facets displayed in Fig. 5.1 & 5.2. This image shows well resolved atomic columns terminating at {100} and {110} planes, indicative of {100} faceting. The facets are forming triangular pyramids with the termination at {110} planes being the junction between two {100} facets.

From these images we can conclude that the {100} faceted surface dominates in as grown samples for both NiO and MgO, when prepared in hydrogen poor conditions. As the form of the facets and overall film structure on S02 is near identical to that of S01, it is reasonable to suggest that NiO, like previously shown for MgO,[4] will preferentially form a new atomic layer over maintaining true layer by layer growth. However even for samples that show no evidence of faceting with a rough disordered surface, a faceted reconstruction can be achieved through sample irradiation by the

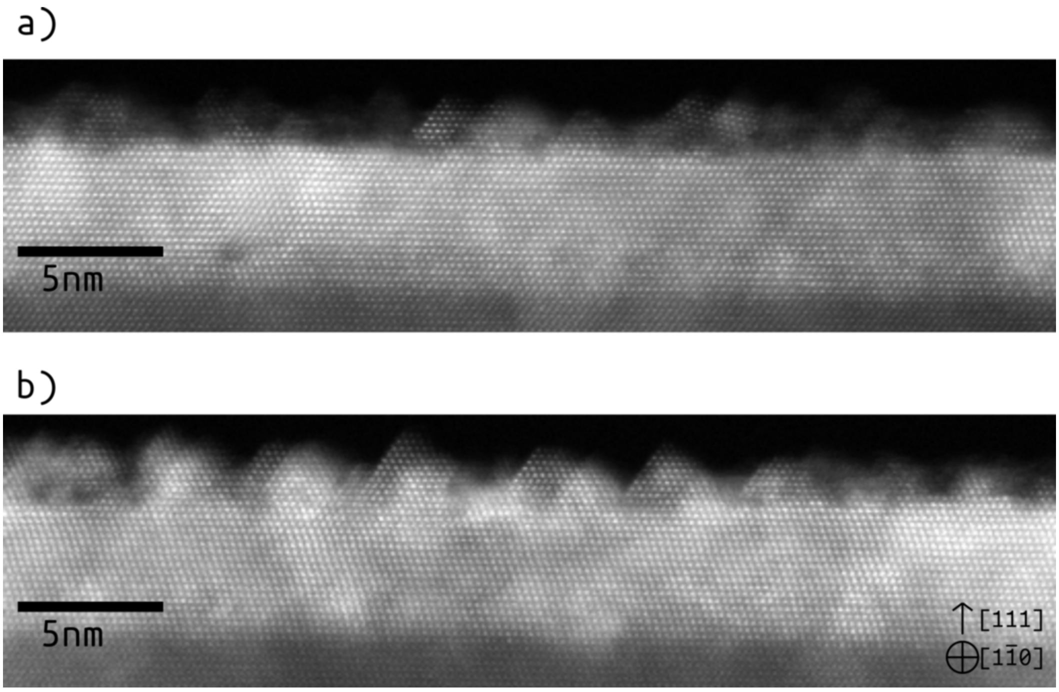

**Figure 5.4:** HAADF images of beam induced faceting on NiO (111). An image of the NiO (111) surface is shown in a) and the beam is left scanning over the displayed region. After some time the surface begins faceting resulting in the image shown in b) whereby the surface is now populated with {100} facets. These images were taken by collaborators at Nagoya University, Japan.

electron beam, as shown by S03, of a STEM. A curious notion is that this behaviour is not seen in standard TEM images of NiO (111) suggesting this reconstruction is triggered by the concentrated beam as it is scanned across the surface.

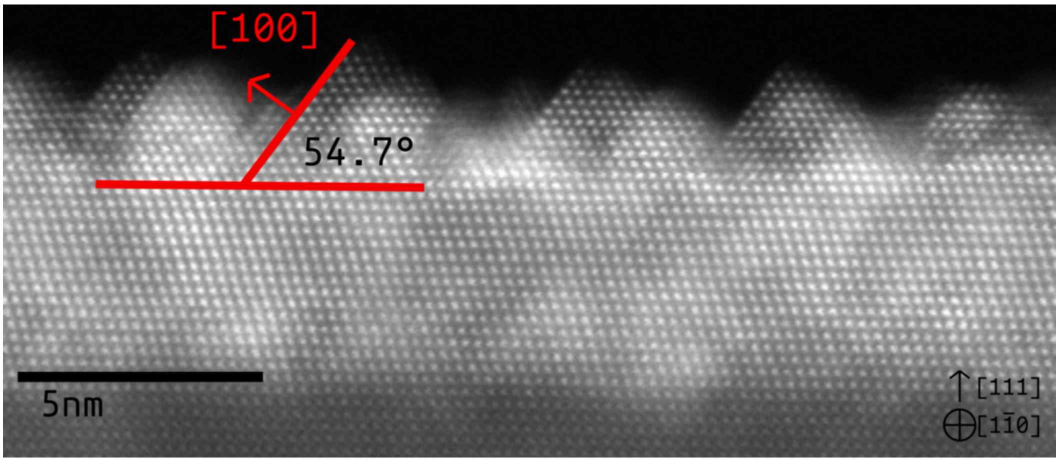

**Figure 5.5:** A higher magnification image of Fig. 5.4b showing more clearly the facets. The atomic columns are well resolved in the image showing abrupt junctures at {100} and {110} planes indicating {100} facets have formed on the surface. This image was taken by collaborators at Nagoya University, Japan.

## 5.4 Surface Structures and Characterisation

To understand the energetics behind the formation of {100} facets on the (111) surface the (100) and (111) surfaces of both NiO and MgO were studied. Five surfaces have been studied for the (111) surface, an OH terminated surface, both cation and anion terminated octopolar reconstructions and faceted surfaces also terminated with both cation and anion. These orientations and terminations are identical between NiO and MgO and as such a common crystal is used for visualisation. For each figure relevant properties are given in blue for NiO and red for MgO, whilst a black sphere is used to represent the cation in each structure.

### 5.4.1 (100) Surface

#### Surface Structure

The (100) surface of MgO and NiO is the lowest energy surface for both structures. The energy required to form this surface is so low, relative to other surface cuts, that both oxide's Wulff construction consists entirely of {100} planes.[91]

The surface energies were calculated as 0.87 J/m$^2$ and 0.90 J/m$^2$, for NiO and MgO respectively. Further properties of each surface are listed in Table 5.2 below. The properties show that, as expected, the two surfaces are structurally extremely similar, with both experiencing similar strain in the bi-layer spacing at the surface. The BCT is the difference between the Bader charge assigned to the atom and the amount of charge defined in the psuedopotential for said atom. For the (100) surface there is a single inequivalent atom per layer with equivalent atom having the same BCT within

|  | Layer | $d_{(L,L-1)}$ (Å) | BCT$_{cation}$ (e) | BCT$_{anion}$ (e) |
|---|---|---|---|---|
| NiO (100) | 1 | 2.07 (1.49%) | -1.18 (1.70) | 1.17 (0.05) |
|  | 2 | 2.11 (0.47%) | -1.17 (1.68) | 1.17 (0.02) |
|  | 3 | 2.10 (0.00%) | -1.18 (1.67) | 1.18 (0.00) |
| NiO bulk |  | 2.10 | -1.18 (1.68) | 1.18 (0.00) |
| MgO (100) | 1 | 2.10 (1.00%) | -1.65 | 1.65 |
|  | 2 | 2.13 (0.47%) | -1.65 | 1.65 |
|  | 3 | 2.12 (0.00%) | -1.65 | 1.65 |
| MgO bulk |  | 2.12 | -1.65 | 1.65 |

**Table 5.2:** The inter-layer spacing, $d_{(L,L-1)}$, and Bader Charge Transfer (BCT) of (100) surfaces. Percentage of the strain for the inter-layer spacing is shown in brackets whilst for the BCT bracketed values represent the Bader spin of the atom.

a $1 \times 10^{-6}$ electrons tolerance. The BCT shows how, despite the lower coordination, the surface ions retain the bulk-like oxidation state.

The reconstruction of both NiO and MgO (100) surfaces is therefore highly localised to the first layer of the surface, this is echoed in the Projected Density of States (PDOS) shown in Fig. 5.6. For both NiO and MgO the 2nd layer is similar to the bulk like region of the slab. The surface layer of MgO has a higher density of states at the Valence Band Minimum (VBM), whereas NiO has a much larger density at the Conduction Band Maximum (CBM). These features are indicative of hole and electron trap susceptibility respectively.[92] The change in density of states at the VBM comes from a shift in the O $p$-orbitals whilst the extra states at the CBM in the case of NiO are Ni $d$-states, shown in Fig. 5.7.

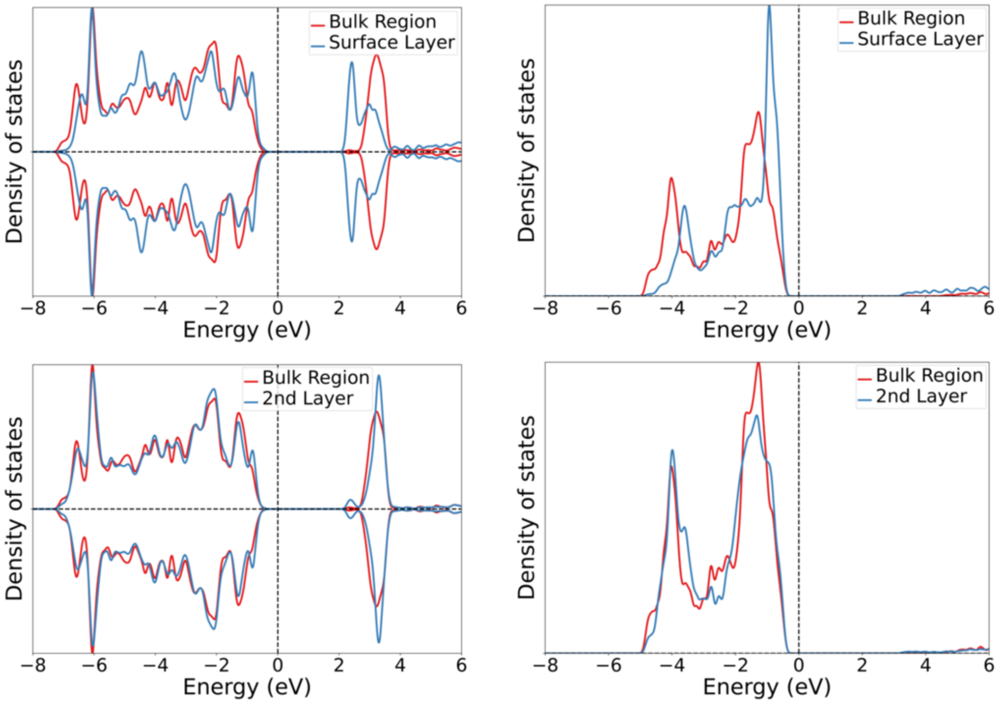

**Figure 5.6:** Projected density of states (PDOS) for the first two layers for the NiO and MgO (100) surface. For all figures the energy axis is calibrated such the Fermi energy of the respective calculations is 0eV. The left two panels show the PDOS for NiO whilst MgO is shown in the right-hand panels. As MgO is non-spin-polarised a single spin channel is shown.

### CO Adsorption

Previous studies of CO adsorption on MgO (100) and NiO (100) have often been performed using embedded cluster models. For NiO this often involves a single Nickel atom in a MgO lattice. The few studies in which a higher level of theory has been implemented often involve restricting the degrees of freedom afforded to the CO

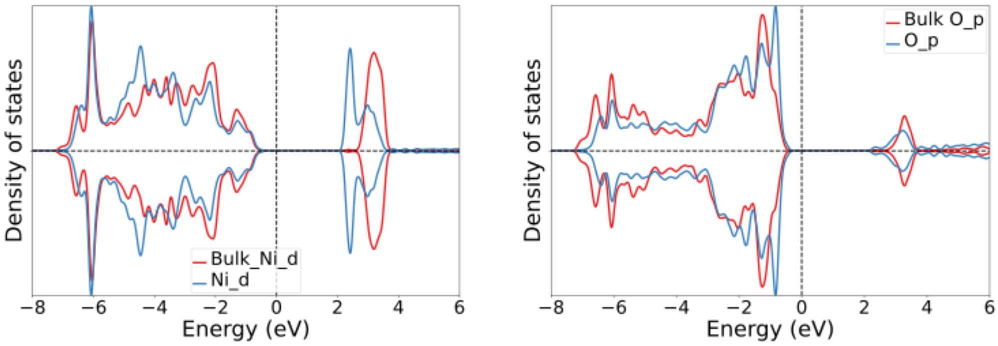

**Figure 5.7:** Orbital projected density of states for a NiO (100) surface. For both figures the energy axis is calibrated such the Fermi energy of the calculation is 0eV.

molecule. This is done as a method of exploring the rotational freedom of the molecule as many geometrical local minima exist with little energy difference or barrier between them. This study addresses this problem by fully optimising the geometry of several molecular rotations, after a single-point energy calculation screening.

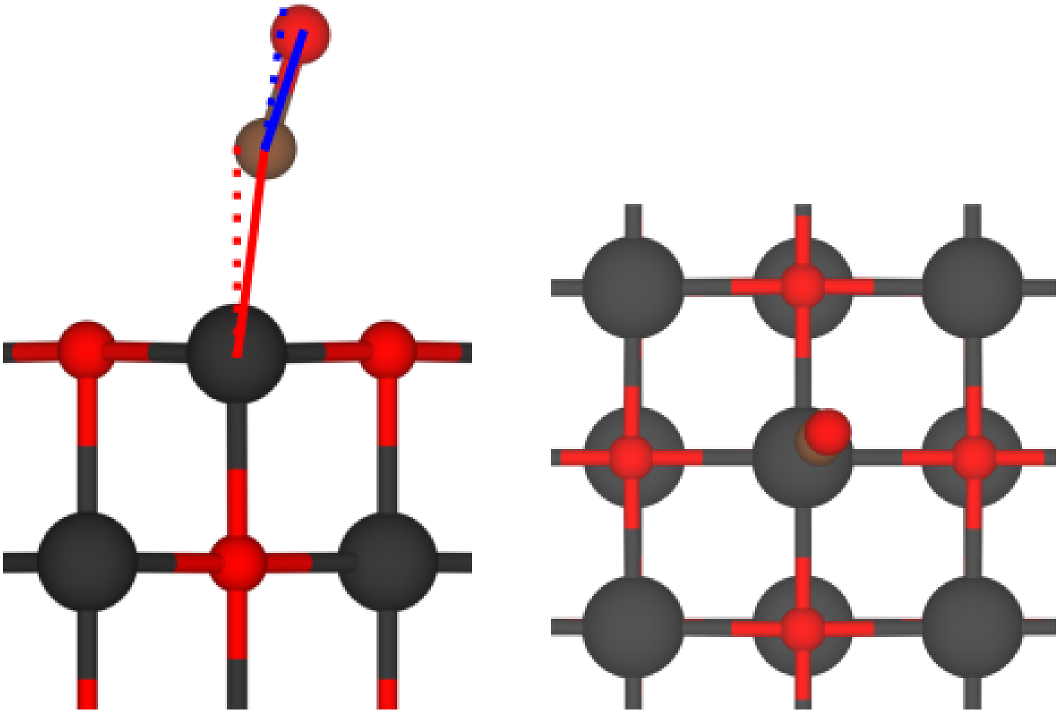

**Figure 5.8:** CO molecular adsorption on a (100) rock-salt surface. Cations are displayed in black whilst oxygen and carbon are red and brown respectively. The solid red line depicts the cation-carbon bond and the angle it makes with the surface normal, represented as a red dotted line, is the first scanning angle, $\phi_C$. The solid blue line depicts the carbon-oxygen bond and the angle it makes with the extension of the cation-carbon bond, the blue dotted line, is the second scanning angle, $\phi_O$. Both of these angles are towards the [011] direction, shown in the right hand image, following previous findings.[57]

The screening was done via a scan over two angles, $\phi_C$ and $\phi_O$. The definition of these angles is shown in Fig. 5.8. From the work of Rohrback, Hafner and Kresse[57] ranges for the two scanning angles were chosen as:

$$0^\circ \leq \phi_C \leq 8^\circ$$
$$-12^\circ \leq \phi_O \leq 12^\circ$$

with steps of 2° and 3° respectively. From this scan the lowest energy structures for each $\phi_C$ were fully optimised. The results of this scan were four distinct structures, for each material, whose properties are shown in Table 5.3.

| | $(\phi_C, \phi_O)$ (°) | Adsorption Energy (eV) | Bond Length (Å) | $\omega$ (cm$^{-1}$) | $\Delta\omega$ (cm$^{-1}$) |
|---|---|---|---|---|---|
| NiO | (0.0, 0.0) | -0.391 | 2.021 | 2071 | -9 |
| | (2.0, 3.4) | -0.391 | 2.022 | 2069 | -12 |
| | (4.0, 6.4) | -0.390 | 2.026 | 2067 | -14 |
| | (6.3, 9.7) | -0.390 | 2.026 | 2066 | -15 |
| | Exp. | -0.4[a] | – | (2142, 2156)[b] | (-1, 13)[b] |
| MgO | (8.2, 11.9) | -0.251 | 2.418 | 2064 | -17 |
| | (6.1, 9.1) | -0.250 | 2.425 | 2067 | -14 |
| | (4.2, 6.6) | -0.249 | 2.427 | 2069 | -12 |
| | (0.0, 0.0) | -0.248 | 2.424 | 2071 | -9 |
| | Exp. | -0.2[c] | – | 2178[d] | 35[d] |

[a] Ref. 93
[b] Ref. 94
[c] Ref. 95
[d] Ref. 96

**Table 5.3:** Adsorption Energy, Bond Length and Vibrational Frequency, $\omega$, of rotated CO molecules on NiO and MgO (100) surfaces. Entries are ordered by material and adsorption energy. $\Delta\omega$ is the shift on vibrational frequency relative to a CO molecule in vacuum, as calculated by DFT.

Contrary to the restrictive optimisations performed by Rohrbach,[57] there is no preference to tilt on the NiO surface. Instead the CO molecule aligned with the surface normal is the lowest energy structure suggesting that the tilt encountered in their study was either an artefact of reduced degrees of freedom or a consequence of higher adsorption coverage, from the calculation having a smaller surface area.

However this is not the case for MgO with all three of the lowest energy structures consisting of high angles for both $\phi_C$ and $\phi_O$.

Apparent from this data is how small the deviation in results, from the tilting of the molecule, is. In both the NiO and MgO the difference between the highest tilt angle and the molecule aligned perpendicular to the surface is, at most, 0.003 eV. For this reason, and the increased number of inequivalent sites, CO adsorption on the other surfaces studied was performed with multiple adsorption orientations only on the low coordinated sites.

### 5.4.2 (111) Surface

Cases that have studied the (111) surface on MgO or NiO, across many levels of theory, consistently find OH-termination and octopolar reconstruction to be the most energetically favourable surface configurations.[9,17] With this in mind surface slabs for these terminations were considered alongside the faceted surface shown in Fig. 5.9, and the cation terminated structure, which is structurally identical with the ions swapped. A facet size of $4a^2$, where $a$ is the lattice constant of the material, was chosen as this retains $\{100\}$ surface behaviour in the centre of the facet.

The surface energy of the different surface terminations is calculated with respect to the $H_2O$ chemical potential and is shown in Fig. 5.10. As with the (100) surface the formation energy is lower for faceted and octopolar terminations of NiO surfaces compared to their MgO counterparts. As these terminations are related to the (100) surface this is unsurprising. The OH-terminated MgO surface however is more stable, shifting the chemical potential at which you would expect this surface to dominate to poorer $H_2O$ conditions. This matches with experimental data as a lower annealing temperature in an environment of air is required to produce sharper (111) surfaces on MgO than NiO. The difference between ion termination in the faceted surfaces is very slight and as such it can be expected to see both terminations across a sample with a more even split on the NiO surface, where the energy difference between the two surfaces is exceptionally tight. This is unlike the octopolar reconstruction where the difference in surface energy between oxygen and nickel termination is orders of magnitude larger. Due to this the ratio of the, more catalytically active,[97] 3-coordinated Ni to 3-coordinated O would be lower in extended regions of octopolar surfaces.

Two larger sized facets of oxygen terminated NiO were studied to explore the effects of increasing the area of exposed (100) facets. The surface energy of these two facet sizes, along with the previously mentioned facet size, are shown in Table 5.4. The surface area of each faceted (111) simulation cell, $A_c$, can be expressed as function of the length of a single side of a facet:

$$A_c = \sqrt{3}n^2a^2 \tag{5.1}$$

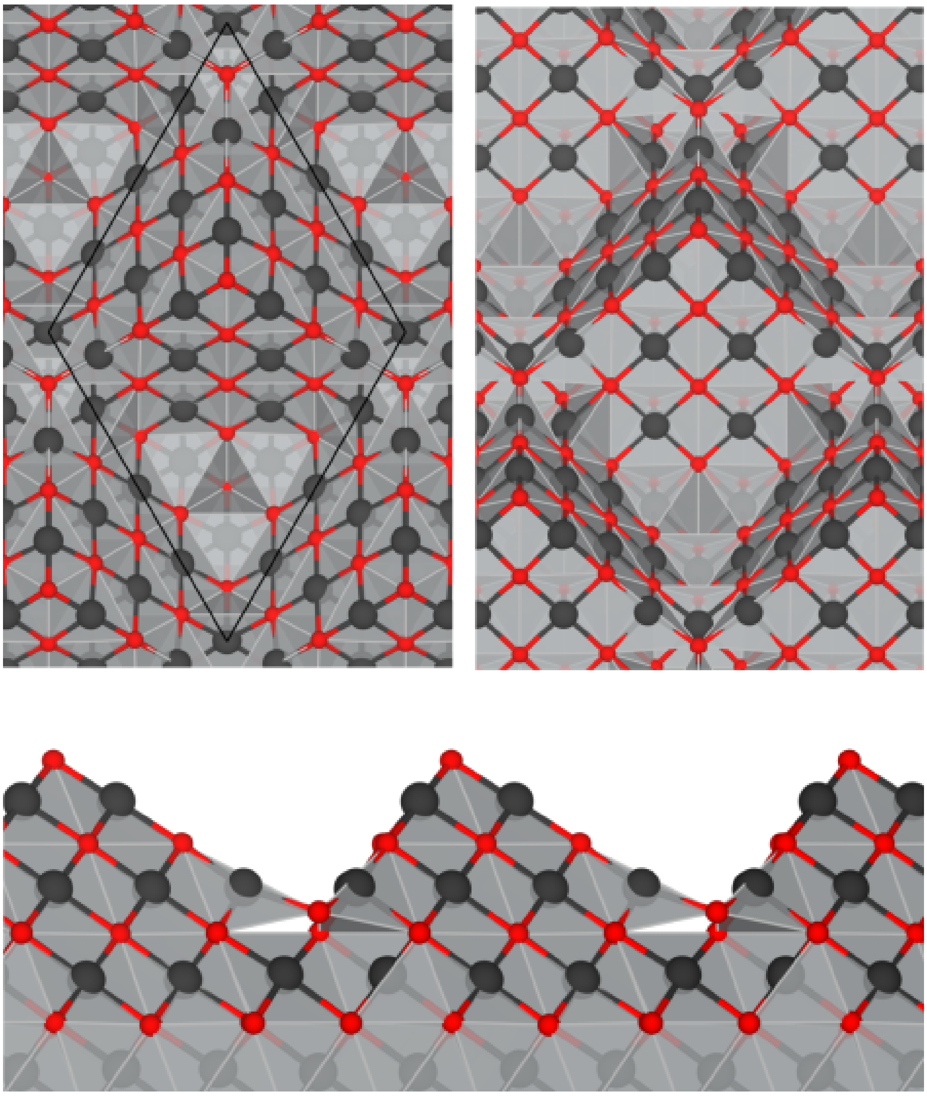

**Figure 5.9:** Images of a fully relaxed, oxygen terminated, faceted (111) surface simulation cell. Cations are displayed in black whilst Oxygen is shown as red. The top left image shows a top down view of cell with the periodic cell boundary as a solid black line. For greater clarity the top right image has been rotated slightly to accentuate the shape of the surface. In the bottom image the cell is viewed down the $[1\bar{1}0]$ axis and shows the raising of the saddle points where the pyramids meet.

where $a$ is the lattice constant and $n$ is the number of lattice constants between the tip of the facet and the saddle point. For the reconstruction shown in Fig 5.9 the value of n would be equal to 2. The reconstruction also has another relevant surface area to consider, the area of the exposed (100) surface - $A_f$. This too can be expressed as a function of the length of the facet edge:

$$A_f = 3n^2a^2 \tag{5.2}$$

where $n$ and $a$ retain the same meaning. By considering the ratio of these two areas,

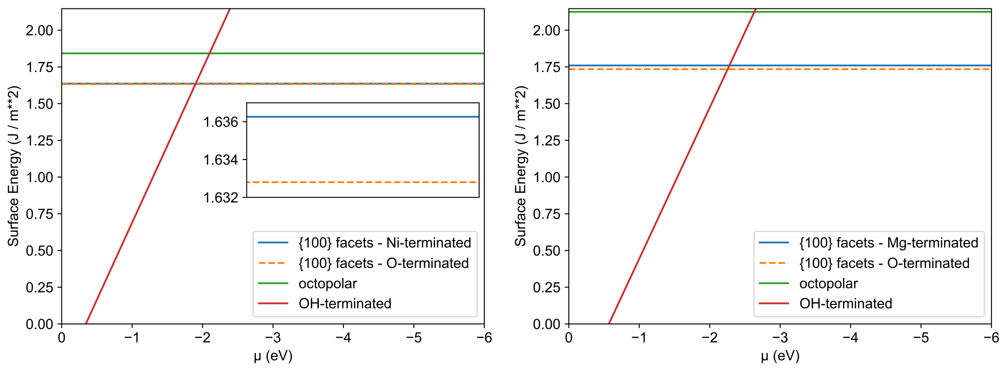

**Figure 5.10:** The surface energy of various reconstructions of the (111) surface of both NiO and MgO, with respect to $H_2O$ chemical potential. The left figure shows NiO and has an inset figure with the same axis highlighting the split between O and Ni terminations of the faceted surface.

it is clear that as the size of the reconstruction increases the ratio between the surface area of the reconstruction and surface area of the exposed facets remains constant.

$$\frac{A_f}{A_c} = \sqrt{3} \tag{5.3}$$

Using this ratio and the previously calculated (100) surface energy allows the calculation of a surface energy assuming that the facets are pristine (100) surfaces. By comparing the values in Table 5.4 with this pristine (100) facet surface energy, also shown in Table 5.4, it shows that increasing facet size increases stability of the surface up to theoretical minimum surface energy.

### Surface Representation

When discussing individual surface sites it is useful to assign them to a group of sites with similar properties. Considering the symmetry of the pyramids allows for the exposed surface to be reduced to a single (100) facet halved along the vertical symme-

| Facet Area | Surface Energy (J/m$^2$) |
|---|---|
| $4a^2$ | 1.63 |
| $9a^2$ | 1.58 |
| $16a^2$ | 1.55 |
| (100) Surface | 1.52 |

**Table 5.4:** The surface energy of increasing facet sizes, where $a$ is the lattice constant of NiO. A value for the surface energy assuming that all exposed facets are pristine (100) surfaces is also presented for comparison.

try line. This leaves eleven symmetrically inequivalent sites shown, colour coded by group, in Fig. 5.11. Each group represents a different coordination of the surface site with five coordinated sites split again to distinguish different local geometry. Where multiple sites have the same coordination further alphabetical identification is provided. Sites will be addressed by their species, coordination and, if applicable, unique identifier. Such that for an oxygen terminated facet the top site would be represented as $O_{3C}$, and the nearest neighbour as $Ni_{4Cb}$. This identifies the termination implicitly as $O_{4Cb}$ would reside on a cation terminated surface. The five coordinated sites are split further as the 5C{c,d,e} sites are closest to the junction formed by the meeting of multiple facets.

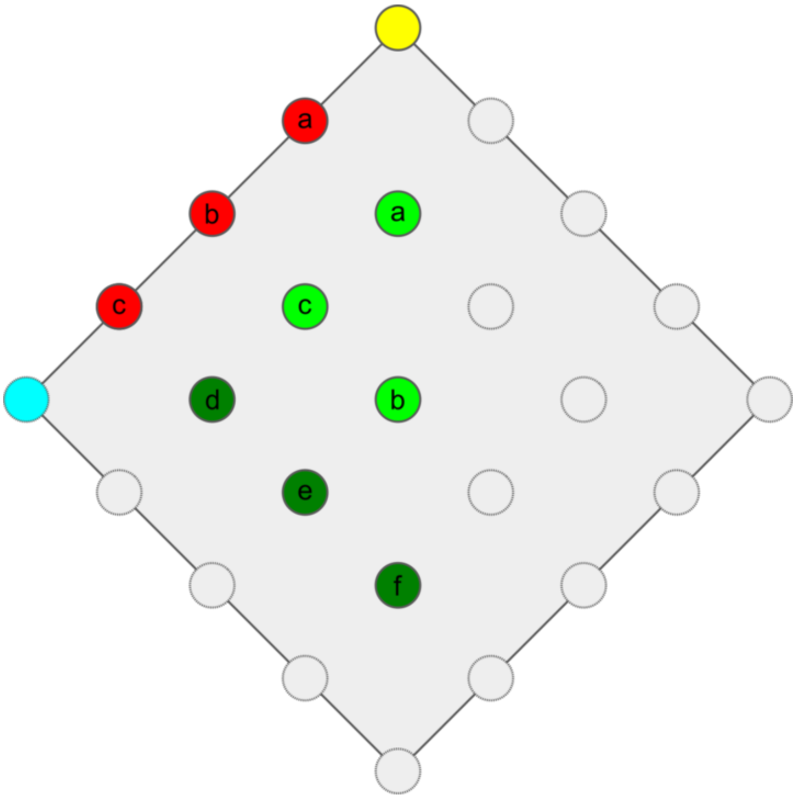

**Figure 5.11:** 2D representation of the symmetrically inequivalent sites on the (111) faceted surface. Symmetrically equivalent and 6C sites covered by other facets are shown in a dashed circle with no colour.. Yellow represents the 3C site with red showing the 4C sites. The light green group is the standard (100) facet sites whilst the dark green group contains the other 5C sites differentiated by their proximity to other facets. The final group is the 6C saddle point between facets, shown in light blue.

### 5.4.3 Bader Charge Distribution

It can be verified that the faceted reconstruction suitably corrects the dipole of the polar (111) surface by considering the equation presented in Chapter 1

$$\sum_{j=1}^{m} \sigma_j = \frac{\sigma_{m+1}}{2} \cdot (-1)^{m+1} \tag{5.4}$$

where m is the number of layers involved in the reconstruction and sigma is the charge density of a specific layer in a Tasker type 3 surface.[5] By calculating the BCT of the atoms within the reconstruction it is possible to approximate the charge density at each atomic layer by assuming constant volume. Doing this for the seven under coordinated layers in both anion and cation terminated faceted surfaces verifies that the dipole has been correctly healed as shown in Table 5.5. Curiously the cation terminated surfaces show better agreement with the expected value, however this is likely due to difficulties the Bader algorithm has with low density regions such as the vacuum gap within the simulation cell. As the ionic radius of oxygen is larger, both the top most atom and saddle point between pyramids are likely to attract more of the vacuum region charge when anion terminated. As part of the reconstruction sees the saddle point atom sit between atomic layers, as shown in Fig 5.9, this could explain the discrepancy for the anion terminated surface. This discrepancy is however relatively small.

| | Surface Termination | $\sum_{j=1}^{m} \sigma_j$ (e) |
|---|---|---|
| NiO | Anion | 9.41 |
| | Cation | -9.44 |
| | Exp | ±9.44 |
| MgO | Anion | 13.19 |
| | Cation | -13.20 |
| | Exp | ±13.20 |

**Table 5.5:** Bader charge analysis of the charge reconstruction required for supressing the polar catastrophe. The expected value is calculated from the Bader charge of the ions in the bulk material and assumes constant distance between atomic layers.

The BCT was also studied per site to examine how the charge density varied at the edge of the facets with respect to the centre, which displayed (100) surface like characteristics.

Table 5.6 confirms the (100) characteristics of the centre of the facet by showing identical charge transfer between the 5Cb site and the first layer of the respective (100)

| Site | NiO |  | MgO |  |
|---|---|---|---|---|
|  | Cation | Anion | Cation | Anion |
| 3C | -1.07 (1.67) | 1.08 (0.17) | -1.60 | 1.60 |
| 4Ca | -1.13 (1.71) | 1.13 (0.04) | -1.63 | 1.63 |
| 4Cb | -1.15 (1.71) | 1.15 (0.12) | -1.63 | 1.63 |
| 4Cc | -1.13 (1.72) | 1.13 (0.12) | -1.63 | 1.62 |
| 5Ca | -1.14 (1.69) | 1.14 (0.01) | -1.64 | 1.64 |
| 5Cb | -1.18 (1.70) | 1.18 (0.06) | -1.65 | 1.65 |
| 5Cc | -1.16 (1.69) | 1.15 (0.01) | -1.64 | 1.64 |
| 5Cd | -1.14 (1.69) | 1.15 (0.02) | -1.64 | 1.64 |
| 5Ce | -1.16 (1.68) | 1.16 (0.06) | -1.64 | 1.63 |
| 5Cf | -1.14 (1.69) | 1.15 (0.04) | -1.63 | 1.63 |
| 6C | -1.24 (1.73) | 1.20 (0.00) | -1.67 | 1.67 |

**Table 5.6:** BCT of specific sites of the facet (111) surface for NiO and MgO. For NiO the Bader spin of each site is also given in brackets.

surfaces reported in Table 5.2. As previously noted for the (100) surface, the range of the BCT for the NiO surface is larger than that of the MgO suggesting that geometrical pertubations have a greater affect on the charge density in NiO than in MgO. This is difficult to separate from the effect of the functional used to simulate the model NiO which obviously is a localised correction. However the consistency between directional shift of the BCT between sites across NiO and MgO lends validity to the results presented.

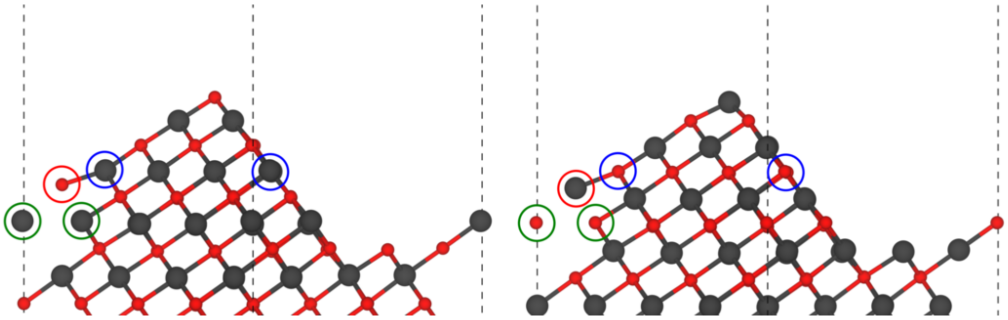

**Figure 5.12:** The relaxed geometry of the saddle point between facets on the pyramidal (111) surface. Cations are displayed in black whilst oxygen is shown as red. The saddle point is circled in red for both the anion and cation terminated structures. Also highlighted are the nearest neighbours of the saddle point in the layer above and below in blue and green respectively. Periodic boundaries of the simulation cell are shown as dashed lines as the structure is viewed down the [$\bar{1}$10] direction.

The under coordinated surface sites all show a reduction in magnitude of BCT with the 3C site showing the largest reduction. This is expected with half of the neighbouring atoms removed. As the site moves further away from the centre of the facet the charge transfer falls, with no difference between the two groups of 5C sites. It is expected to see smaller changes in BCT than integer steps between oxidation states for transition metals.[98] Of particular note is the 6C site which for each individual material has a higher magnitude of charge transfer. This charge transfer has a noticeable effect on the geometry of the reconstruction as shown in Fig. 5.12. The 6C site, which acts as the saddle point between the pyramids, is raised to sit in-between the two atomic layers. This shift in position maintains bulk-like bond distances between itself and its neighbours above - closer to the top of the pyramid, whilst extending the bond length to the neighbours below. The extension, of around 12% for both materials and both terminations, is also seen in the octopolar reconstruction on a smaller scale, only extending by around 6%.

### 5.4.4 Surface Characterisation via Vibrational Spectroscopy

Like the (100) surface, CO was adsorbed onto the inequivalent sites of the faceted surface reconstruction. Using the results from the (100) surface, adsorption on the hollow and oxygen sites were not considered. Unsurprisingly the 6C site was not a viable adsorption site due to being fully coordinated, and as such any attempt to adsorb a CO molecule onto the site resulted in CO floating into the vacuum gap. The 3C and 4C sites had multiple orientations of CO molecules adsorbed and the lowest energy configuration was used. Interestingly, like in the case of the (100) surface, the material of the surface provided variation to the orientation of the adsorption. For NiO this resulted in the CO molecule preferring to be aligned with the normal of the (100) facet whilst on MgO the CO aligned with the [110] direction. This is shown for $Ni_{3C}$ and $Mg_{3C}$ in Fig 5.13 however it occurred for all 4C sites as well.

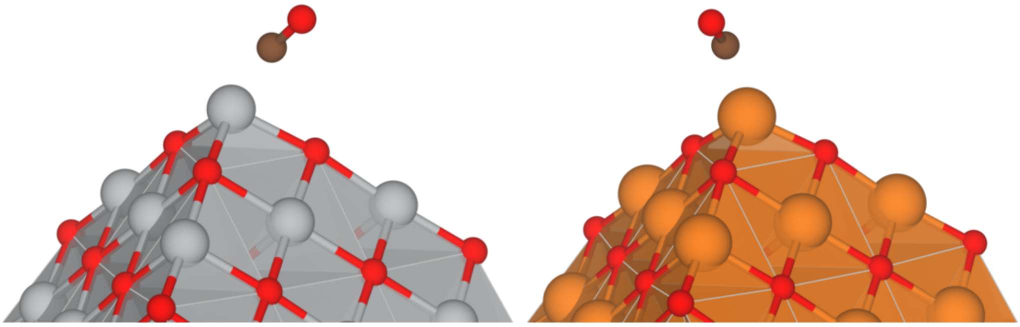

**Figure 5.13:** Differing CO adsorption energies between NiO, the left hand image, and MgO, shown on the right. Cations, Ni and Mg, are shown in grey and orange whilst oxygen and carbon are red and brown respectively. The site on which the CO molecule is adsorbed is the same in both images, $Ni_{3C}$ and $Mg_{3C}$. For NiO the CO is aligned with the normal to the front facing (001) facet whilst in the MgO structure the CO aligns with the [011] direction.

Fig. 5.14 shows a colour coded map of the adsorption sites, weighted by adsorption energy. Comparing this figure with Fig. 5.11 shows that besides the coordination also the local environment affects the interaction between surface and molecule. The collection of 5C sites located near the joining of two or more facets show a substantial favourability for CO adsorption over the standard (100) facet sites. The vibrational frequency of these sites are shifted by a much larger amount than the (100) surface like sites on the facet also, as shown in Table 5.7. For both NiO and MgO the most favourable sites, 3C and 4Ca, have the same CO vibrational frequency as CO adsorbed on the octopolar reconstruction with only the stronger binding to the surface of the faceted reconstruction distinguishing the two geometries. However the 5C sites show a large deviation with 5C{a,b,c} redshifting by 10cm$^{-1}$ bringing the value inline with what is expected on a (100) surface. The remaining 5C{d,e,f} flip this and blueshift, with the site adjoining the meeting point at the base of 3 facets (5Cf) shifting by around 50cm$^{-1}$. As the large blueshifting site is fairly favourable with respect to the rest of the sites this shift should be noticeable even at low coverage.

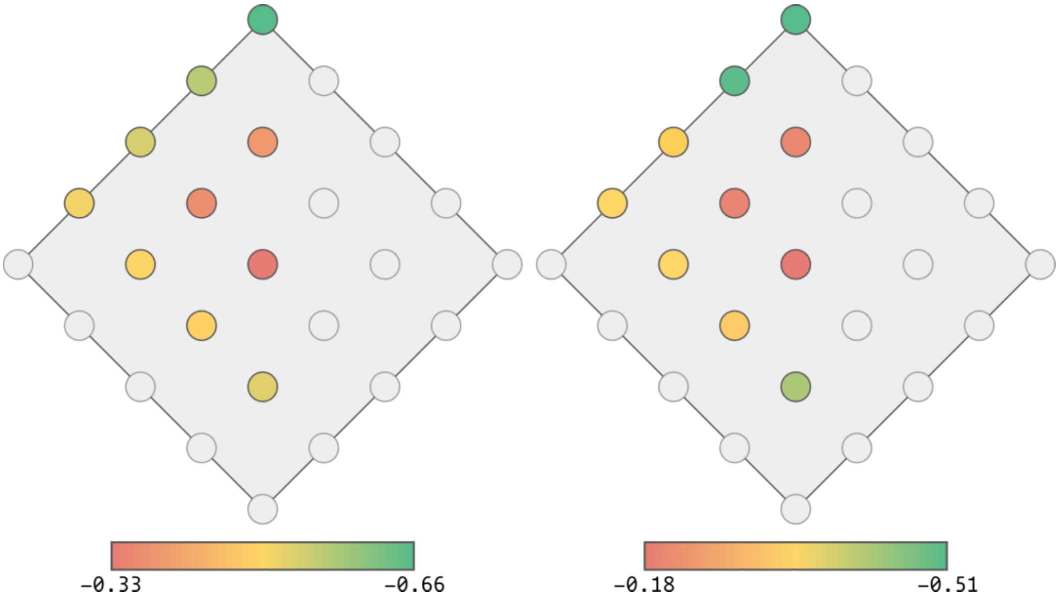

**Figure 5.14:** CO molecular adsorption on a (111) rock-salt surface using site map shown in Fig 5.11. Each site is coloured site is colour based upon the adsorption energy of the site. NiO is shown on the left and MgO on the right hand side. The precise values for each site are given in Table 5.7. Both materials show a similar distribution across the sites with the increased favourability of $Ni_{4C}$ sites compared with $Mg_{4C}$ being the largest difference.

Whilst the value of $\omega$ is not close to experiment, a known problem for DFT, it is argued here that the shifts within a material are accurate. This is evident in the octopolar reconstruction for NiO which has a $\Delta\omega$ of -13cm$^{-1}$ when compared with

| Site | Adsorption Energy (eV) | | $\omega$ (cm$^{-1}$) | | $\Delta\omega$ (cm$^{-1}$) | |
|---|---|---|---|---|---|---|
| | NiO | MgO | NiO | MgO | NiO | MgO |
| 3C | -0.66 | -0.51 | 2059 | 2075 | -12 | 9 |
| 4Ca | -0.50 | -0.50 | 2059 | 2075 | -12 | 9 |
| 4Cb | -0.46 | -0.27 | 2066 | 1970 | -5 | -94 |
| 4Cc | -0.44 | -0.28 | 2042 | 2018 | -29 | -44 |
| 5Ca | -0.35 | -0.20 | 2070 | 2070 | -1 | 6 |
| 5Cb | -0.32 | -0.18 | 2069 | 2068 | -2 | 4 |
| 5Cc | -0.34 | -0.19 | 2071 | 2067 | 0 | 3 |
| 5Cd | -0.41 | -0.28 | 2023 | 2048 | -48 | -16 |
| 5Ce | -0.39 | -0.27 | 2029 | 2054 | -42 | -10 |
| 5Cf | -0.45 | -0.39 | 2010 | 2026 | -61 | -38 |
| Octopolar | -0.47 | -0.44 | 2058 | 2040 | -13 | -24 |

**Table 5.7:** Adsorption energies and vibrational frequencies for faceted (111) surfaces of NiO and MgO. The difference between the vibrational frequency of the site and the vibrational frequency of a CO molecule on a (100) surface for each material is also shown as $\Delta\omega$. Due to the size difference of simulation cells the octopolar reconstruction is calculated at a coverage of 0.25ML as opposed to the 0.0625ML of the faceted surface.

the (100) surface. This compares well to the experimental value of -8cm$^{-1}$.[99] As such the $\Delta\omega$ value is more important result.

## 5.5 Conclusions

This chapter has shown the various pathways to the formation of {100} facets on both NiO and MgO (111) surfaces. The facets have been imaged through STEM and TEM imaging techniques and the transition between reconstructions has been captured. To support these findings DFT+$U$ and DFT calculations have been performed to judge the stability of these reconstructed surfaces with respect to other known terminations. The faceted surface is more stable than the previous agreed upon stable structure of the p(2×2) octopolar reconstruction and in $H_2O$ poor conditions is more stable than p(1×1) OH termination. Further to this the calculations provided characteristic signatures by which to identify the reconstructions through CO vibrational spectroscopy. We predict that the (111) faceted surface will show vibrational frequencies that match that of the (100) surface at high coverage whilst also showing red shifts much greater than the octopolar surface at low coverage.

## CHAPTER 6

# NIO AS A CATALYST FOR THE WATER-GAS SHIFT REACTION

In this chapter the polar NiO (111) surface is considered as a redox catalyst for the WGSR. Through environmental TEM the surface of NiO (111) films is shown to become amorphous like in the presence of CO molecules. Using environmental XPS this is shown to be a reduction to nickel metal and exposure to atmospheric conditions re-crystallises the sample into a {100} faceted (111) surface of NiO. The energetics of this reaction are explored using DFT and it is shown that the reduction in the energy cost to form oxygen vacancies on the (111) surface is facilitating the reaction. As well as the reduced cost of vacancy formation, unlike the (100) surface, the (111) surface dissociatively adsorbs water molecules. This provides a pathway for re-oxidation of the surface, making NiO a candidate for use as a redox catalyst in the WGSR. This is confirmed via environmental TEM of NiO (111) interacting with a CO and $H_2O$ environment, in which the surface is shown to be dynamic yet remain crystallised.

## 6.1 Introduction

The NiO (111) surface is considered a more active catalytic surface than the more stable (100) surface due to the low coordinated sites exposed via reconstructions driven by the polar catastrophy.[100] Due to the importance of CO oxidation for pollution reduction in cleansing of exhaust fumes many reactions involving such reactions have been studied for transition metal oxides. One such reaction, the WGSR - named for shifting the ratio of CO to $H_2$ in water-gas, converts CO and $H_2O$ into $CO_2$ and $H_2$. The WGSR is known to be exothermic with a reaction enthalpy of -41 kJ/mol. Previous work has considered the NiO (111) surface an active catalyst for associative CO oxidation in the presence of $O_2$[101] however, with the less active (100) surface known to reduce in CO atmospheres at temperatures upwards of 873K,[102] NiO (111) is a candidate for CO oxidation via reduction. Moreover the (111) surface of NiO is known to dissociatively adsorb water molecules which could facilitate the re-oxidation of the reduced surface.[16,103] This would suggest that NiO could be used as a redox catalyst for the WGSR.

In this chapter the reduction of NiO in a CO atmosphere is studied via environmental TEM, XPS and DFT. Comparisons between (100) and (111) surfaces will be made to study how the different coordination of surface atoms affects the formation of oxygen vacancies and how this directly impacts catalytic performance. The re-oxidation of the surface via exposure to $H_2O$ is also considered with the difference in adsorption of a water molecule providing the lower barriers to re-oxidation. The structure of the re-oxidised sample is examined via TEM and XPS supports the view provided. Finally NiO is shown to act as a catalyst in the WGSR through a redox mechanism and potential ways to improve performance are suggested.

## 6.2 Methods

### 6.2.1 Transmission Electron Microscopy

Images shown of NiO in various gaseous atmospheres were taken by collaborators at the Nagoya University. The samples used were grown, by Dr. Kosuke Matsuzaki, on MgO (111) substrates via PLD using the same methods as previously stated for S03 in Chapter 5. The images were collected using an environmental TEM. This microscope uses differential pumping to allow high gaseous pressure around the sample whilst maintaining a high vacuum throughout the rest of the electron beam's path.[104] This is achieved by widening of the objective lens pole pieces, as pioneered by Boyes and Gai,[105–107] to facilitate a series of differential pumping apertures.

### 6.2.2 XPS

The samples used for the XPS experiments were grown, via PLD, on Nb doped $SrTiO_3$ substrates by collaborators at Xiamen University. This was done as the technique requires a conductive substrate and as the reaction is occurring entirely at the surface of the sample should not cause any noticeable difference between the two experiments. The samples were measured at the Eindhoven University of Technology by collaborators. The peaks where determined using Gaussian fitting on the spectra of the fully reduced and fully oxidised sample. The time resolved data was sampled at a rate of 31.5 seconds, the acquisition time of the equipment and was captured until no further changes in the spectra were observed. For the temperature resolved data the spectra were captured as the temperature was increased, this introduces a few errors to the temperature measurement. The temperature was increased slowly, at a rate of 10K/min, to allow for the system to rise in temperature as a whole. However as the temperature recorded for each spectra is tied to the temperature of the heaters set point it is unlikely that the sample stage is at the temperature recorded and instead is at a lower value. Coupled with this NiO is known to have an induction period with low temperature reduction taking several minutes to occur.[108] This means that the temperature values at which reduction is shown to happen in these XPS experiments are likely higher than the actual value.

### 6.2.3 Formation Enthalpy

The formation enthalpy of each material was calculated using DFT and the assumption was made that the formation enthalpy, $\Delta H_f$, is equal to the formation energy, $\Delta E_f$, determined as

$$\Delta H_f = \Delta E_f = E - \sum_i n_i \mu_i. \tag{6.1}$$

Where $E$ is the total energy of the material and $i$ is each constituent part. The references from which the formation enthalpy is calculated have the number and chemical potential, given as $n_i$ and $\mu_i$ respectively, summed to supply an energy of the isolated components. For each material studied - NiO, MgO, $CO_2$ and $H_2O$ - the reference systems for the calculation of each constituent part were calculated at the same level of theory as the material and as such Ni metal was calculated with Hubbard-like U value on the $3d$ electrons. The chemical potentials selected do not include carbides or hydroxides as these are not deemed critical to the WGSR on the studied materials. This is justified in the case of carbides as there is no indication of their presence in the reduction process, as shown by XPS and the ability of the surface to recrystallise after the reduction process, shown via TEM. This recrystallisation is also evidence that, whilst likely an intermediary step in the oxidisation, hydroxides do not effect the overall thermodynamics of the process. This is due to the final structure of the films, imaged via TEM, being shown to be in the faceted reconstruction rather than the abrupt hydroxylated surfaces. For NiO and MgO the chemical potentials were the corresponding metal in an FCC structure and half the total energy of an isolated $O_2$ molecule in a triplet spin state. The oxygen molecule was used in the calculation of the formation enthalpy for all materials with the other systems being an isolated $H_2$ molecule and isolated CO molecule for $H_2O$ and $CO_2$ respectively. CO was used as reference system for the formation enthalpy of $CO_2$, instead of graphite and an $O_2$ molecule for easy calculation of the reducibilty of NiO and MgO. The expressions used to calculate each formation enthalpy are shown below.

$$\begin{aligned} \mathrm{NiO}(s) &\rightarrow \mathrm{Ni}(s) + \frac{1}{2}\mathrm{O}_2(g) \\ \mathrm{MgO}(s) &\rightarrow \mathrm{Mg}(s) + \frac{1}{2}\mathrm{O}_2(g) \\ \mathrm{CO}_2(g) &\rightarrow \mathrm{CO}(g) + \frac{1}{2}\mathrm{O}_2(g) \\ \mathrm{H}_2\mathrm{O}(g) &\rightarrow \mathrm{H}_2(g) + \frac{1}{2}\mathrm{O}_2(g) \end{aligned} \tag{6.2}$$

### 6.2.4 Gibbs Free Energy

The free energy of a system is given by

$$\Delta G = \Delta E_f + p\Delta V - T\Delta S \tag{6.3}$$

where $\Delta E_f$ is the formation enthalpy, $p\Delta V$ - set to zero for a constant volume equation - is the pressure and change in volume and $T\Delta S$, the temperature and change in entropy, is calculated for only the gaseous elements of the reduction using the *JANAF* thermochemistry tables.[24] The tables provide values of entropy for many materials at standard pressure for a range of temperatures. The difference between the entropy of the product and reactant gases can be calculated directly from these tables and used with the formation enthalpy to provide a value of the Gibbs free energy at specific temperature.

## 6.3 Formation Enthalpy

The formation enthalpy for $CO_2$, $H_2O$, NiO and MgO were calculated using DFT and compared with experimental values. This provides an indication to the feasibility of the material for reduction in CO and oxidation in $H_2O$. The results of the calculations, along with the expected values are shown in Table 6.1. From this table it is clear that, whilst the values predicted don't match exactly with experimental evidence, the ordering of the heats of formation is correct. This means that at the level of theory used we still expect to capture the right dynamics. NiO is shown to be reducible in a CO atmosphere as the formation enthalpy of $CO_2$ is lower. Reducing MgO in a CO atmosphere is, however, endothermic and energy would need to be supplied to the system. The irreducibility of MgO is well known and as such is not considered in this chapter as a catalyst for the WGSR. Both NiO and MgO would re-oxidise in the presence of water vapour due to the relatively high formation enthalpy of $H_2O$. The reaction enthalpy of the WGSR can be calculated from these values to give -62 kJ/mol.

|  | NiO | MgO | $CO_2$ | $H_2O$ |
|---|---|---|---|---|
| $\Delta H_f$ | -305 | -467 | -314 | -252 |
| Exp. | -244 | -602 | -283 | -242 |

**Table 6.1:** Values of the formation enthalpy, as calculated by DFT compared to experimental values. All values are given in kJ/mol and experimental values are taken from Ref. 109.

## 6.4 Carbon Monoxide Induced Reduction

### 6.4.1 Environmental TEM

The effects of CO on NiO (111) were captured via an environmental TEM and are shown in Fig. 6.1. This details the evolution of a flat crystalline NiO surface into an amorphous like, constantly evolving surface. This transformation happens within a period of 48 seconds and affects a 1.5nm thick region at the interface of the surface and CO environment. The quasi-liquid layers at the surface appear to be formed by the formation, and subsequent segregation, of oxygen vacancies in the surface layers, likely driven by the electron beam. With the surface becoming heavily reduced, oxygen is constantly being moved through the amorphous like region of Ni to interact with the CO and form $CO_2$.

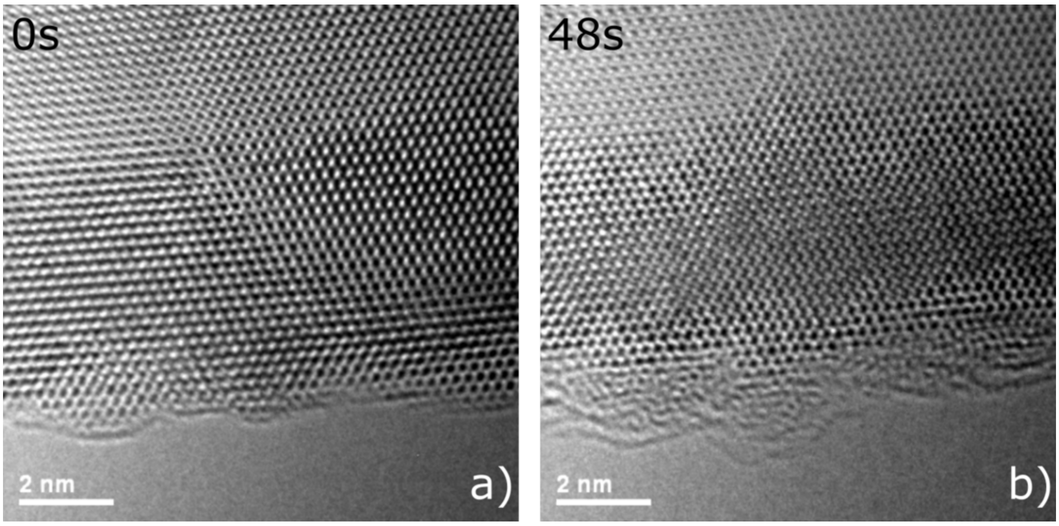

**Figure 6.1:** Snapshots from a TEM video of a NiO (111) surface, viewed down the $[1\bar{1}0]$ in a 0.05Pa CO atmosphere. Shown in (a) is the surface as CO is introduced with a sharp, crystalline surface. (b) is the same area 48 seconds later, now showing an amorphous and mobile, 1.5nm thick, region at the surface.

### 6.4.2 Environmental XPS

To confirm that the amorphous region shown in Fig. 6.1b is due to carbon monoxide reducing the NiO surface the same experiment was performed in an environmental XPS. First a NiO(111) film was exposed to CO whilst it was heated from room temperature to 773K, at a rate of 10K/min, and then held at this temperature for 3 minutes. The temperature recorded was the temperature set point at the time the spectra was taken. Fig. 6.2 shows the Ni $2p_{3/2}$ peak and satellite as it evolves carbon monoxide atmosphere. The data confirms a NiO surface with the multiplet-split $Ni2p_{3/2}$ at 854.6eV and 854.9eV, characteristic of oxidised nickel.[110] The satellite peak at 861.6eV is also characteristic of NiO compared to the lower energy, 858eV, satellite peak of Ni metal. As the temperature is increased a peak at 852.3eV develops indicative of $Ni2p_{3/2}$ in nickel metal.[111–113] Also evident in the 773K data is a peak at 869.6eV consistent with $Ni2p_{1/2}$ for metallic nickel.[111]

As the temperatures below 773K show no evidence of NiO reduction the data suggests the reaction is endothermic. However the extent of the energy required may not be as high as the 773K implies due to the difference between set point temperature and

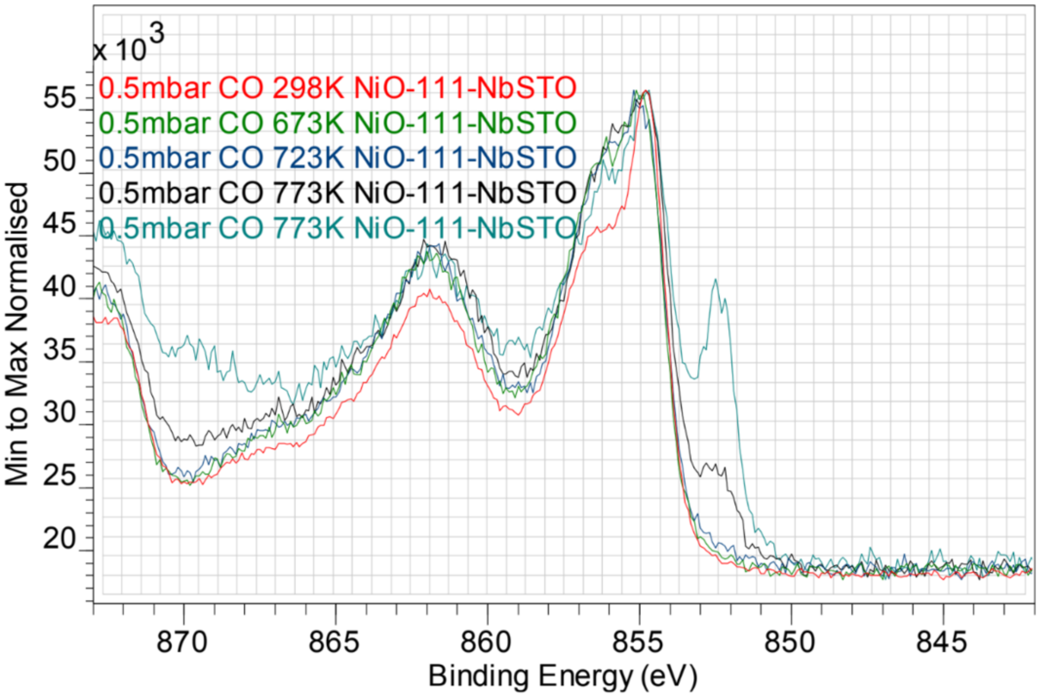

**Figure 6.2:** XPS of the temperature resolved evolution of NiO (111) in a CO atmosphere. The data is centred on the multiplet-split Ni2$p_{3/2}$, evident at 854eV and 856eV, and its satellite peak, visible at 862eV, both consistent with NiO. As the temperature is increased a new peak, identified as Ni2$p_{3/2}$ peak in nickel metal, is seen at 852eV. Also providing evidence of the reduction of NiO to metallic Ni is introduction of the Ni2$p_{1/2}$ peak at 869eV. The data has been normalised such that the maximum and minimum values of each curve are the same.

sample temperature. This means that when studying the TEM images it is likely that the driving force of the reaction seen is interaction with the electron beam. The energy deposited in the surface from the incident electrons provides the necessary energy to allow the reduction of NiO in a CO atmosphere.

Also assessed was the time evolution of the reduction reaction at the temperature 773K. Spectra, taken at 31.5 second intervals, show the increasing relative count of metallic nickel Ni2$p_{3/2}$ in comparison to an oxidised Ni2$p_{3/2}$ as well as the introduction of a metallic Ni2$p_{1/2}$ peak at 869.6eV. Like with the temperature resolved evolution of the reaction these features are indicative of the reduction of NiO. The XPS data further supports the TEM images as the relative height of the metallic nickel peaks stops increasing after 2 minutes suggesting that there is a maximum level of reduction the surface is able to under go, as evidenced in the constant thickness of the amorphous nickel layer with respect to time in Fig. 6.1.

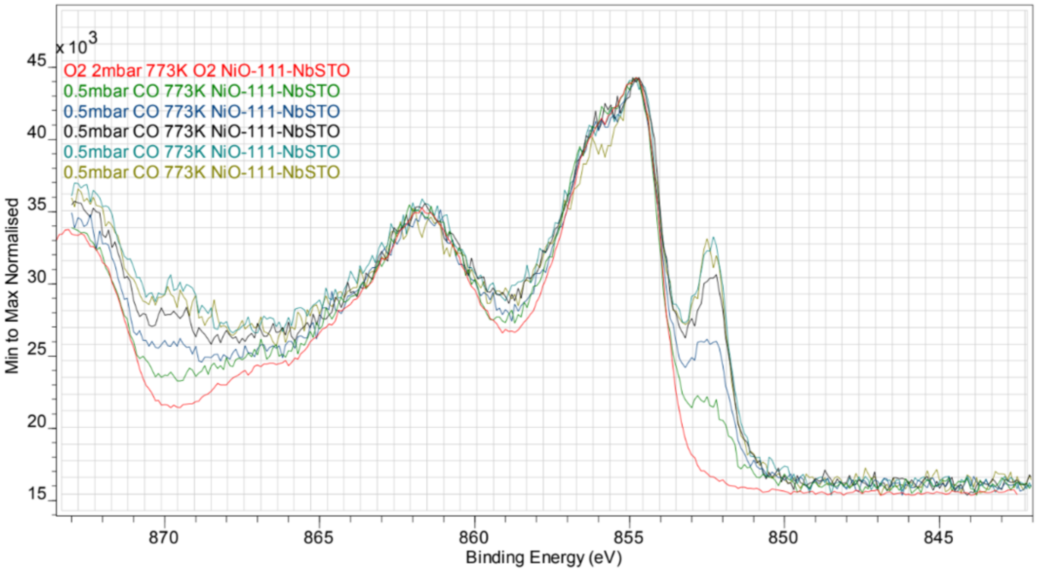

**Figure 6.3:** XPS of the time resolved evolution of NiO (111) in a CO atmosphere. As with Fig. 6.2 the data is centred on the multiplet-split Ni2p$_{3/2}$, evident at 854eV and 856eV, and its satellite peak, visible at 862eV, both consistent with NiO. As time evolves, through intervals of 31.5 seconds the peaks characteristic of Ni metal grow in counts relative to the NiO peaks. This stops after 2 minutes suggesting that the surface is fully reduced.

### 6.4.3 Density Functional Theory

To explore the reducibility of NiO (111) surfaces in a CO atmosphere the formation of oxygen vacancies were studied. For comparison the NiO (100) surface is also studied as a reference and is presented first. Previous work has assessed oxygen vacancies in NiO (100) surfaces and found that whilst a vacancy in the subsurface layer is the most stable, the migration energy barrier between the two layers is extremely high and as such, due to the reduction being facilitated by a surface interaction, we only consider the surface vacancy.[114,115] As mentioned in Chapter 5 the (100) surface has only one symmetrically inequivalent site and the vacancy at this location is shown in Fig.6.4.

The vacancy causes the neighbouring Ni atoms to distort, contracting their position around the vacancy. For the neighbouring Ni atoms, in both the surface and the subsurface layers, this positional shift has a magnitude of 0.05Å. The formation energy of the vacancy, with respect to half an isolated $O_2$ molecule, was calculated to be 4.6eV. This energy and the local distortions matches well with other previous studies of the (100) surface and bulk NiO.[114–116] Following the reaction,

$$\text{Surface} + \text{CO} \rightarrow \text{Surface}_{\text{Vacancy}} + \text{CO}_2, \tag{6.4}$$

the formation of this vacancy was then calculated with respect to CO and $CO_2$ refer-

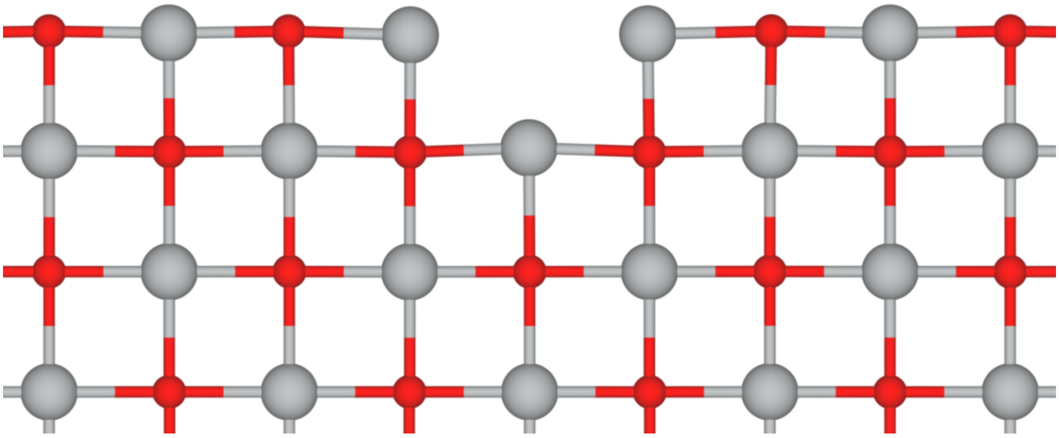

**Figure 6.4:** The structure of an oxygen vacancy at the (100) surface of NiO viewed down the [001] direction. Nickel atoms are shown as grey whilst oxygen is red. A [001] slice is shown of the plane containing the vacancy. A clear contraction centred on the vacancy is clear for the nearest neighbouring Ni atoms.

ence molecules. This reduction energy, $E_{\text{reduction}}$, was calculated using Eqn. 6.5.

$$E_{\text{reduction}} = E_{\text{vacancy}} + E_{CO_2} - (E_{\text{surface}} + E_{CO}) \tag{6.5}$$

The value of $E_{\text{reduction}}$ was calculated as 1.35eV, showing that the reduction of NiO (100) in a CO atmosphere to produce $CO_2$ is endothermic.

The same calculations were then performed on a faceted (111) surface. The site notation is the same as used in the previous chapter and shown in Fig. 5.11. The formation energy of the vacancies for the (111) surface are visualised in Fig. 6.5 with 3.87eV being the lowest for an oxygen terminated surface and 3.91eV the lowest for a nickel terminated surface.

The $O_{5Ca}$ site vacancy, much like the (100) surface vacancy, causes a contraction around the vacancy with the neighbouring Ni atoms shortening their distance to the Ni atom directly across the vacancy by 0.2Å. This is a much larger distortion than in the case of the (100) surface and the greater movement stems from less rigidity in the $Ni_{4Ca}$ sites as opposed to the (100)-like $Ni_{5Cc}$ sites. As the $Ni_{4Ca}$ sites are able relax further the distortion across the vacancy doesn't share the same 4-fold symmetry about the vacancy as in the (100) surface, only being mirror symmetric across the centre line

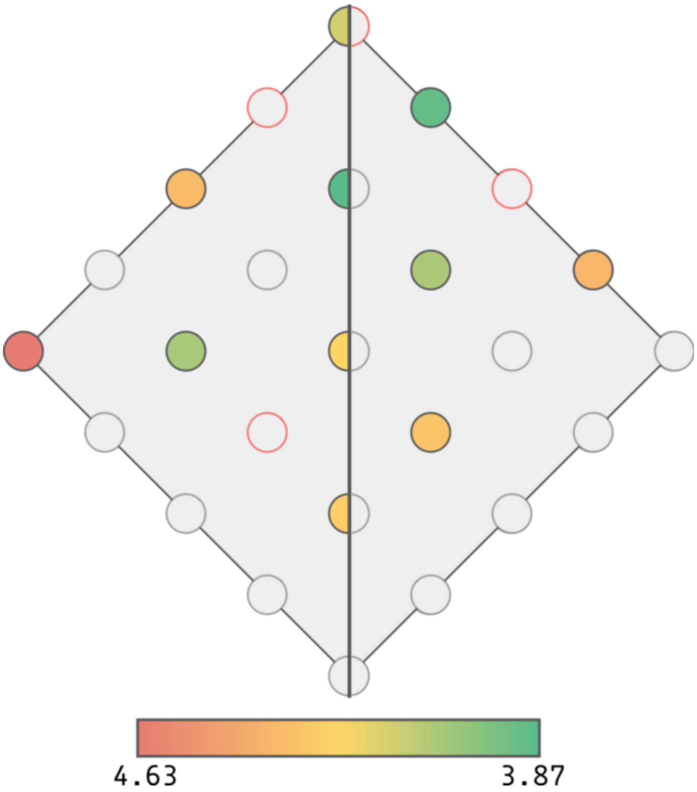

**Figure 6.5:** Oxygen vacancies on both oxygen and nickel terminated faceted NiO (111) surfaces. Left of the centre line represents the oxygen terminated surface whilst the nickel termination is shown on the right. Vacancies are colour coded by their formation energy in electron-volts with the $O_{5Ca}$ site being the most stable and the $O_{6C}$ being the least. Highlighted with red borders are the two lowest energy adsorption sites for CO on the respective termination. The proximity of the CO molecules to the favoured oxygen vacancies helps provide pathways for reduction.

of the facet. This asymmetry is also reflected in the BCT with the $Ni_{4Ca}$ sites gaining an extra 0.06 electrons over the $Ni_{5Cc}$ sites as a consequence of the vacancy.

The Ni terminated (111) faceted surface performs a very different reconstruction to accommodate the oxygen vacancy. When the $O_{4Ca}$ site is both adjoining $Ni_{5Ca}$ sites are attracted to each other shortening their separation by 0.07Å. However the distance between the $Ni_{3C}$ and $Ni_{4Cb}$ site increases by 0.03Å. This occurs due to relaxation of the $Ni_{3C}$ site into the {100} facet not containing the oxygen vacancy. The $Ni_{3C}$ also sees a larger increase to the BCT, having an extra 0.34 electrons assigned to it than the $Ni_{5Ca}$ sites, that see a similar gain to that of the $Ni_{5Cc}$ sites of the oxygen terminated surface.

The reduction energy was calculated for the oxygen terminated and nickel terminated faceted surface using Eqn. 6.5. These values are 0.61eV and 0.65eV respectively. This is a drastic drop in required energy for the reduction to occur in comparison to the (100) surface, with both surfaces requiring less than half the reduction energy of the (100) surface. The reaction is endothermic, as expected from the XPS data which only showed reduction of the surface at a set-point temperature of 773K.

At standard pressure, $T = 800K$ and $\Delta V = 0$ (constant volume) then $\Delta G$ is calculated, using Eqn. 6.3, as 0.36eV for the oxygen terminated surface. Whilst still endothermic, this value is a relatively small energy difference.

## 6.5 Re-oxidation via Exposure to Water Vapour

### 6.5.1 Transmission Electron Microscopy

Reduced NiO, from exposure to CO in the electron beam, was left in ambient environmental conditions over night. The sample was then placed back in the TEM and imaged in a vacuum. The film structure is shown in Fig. 6.6. It is clear from the image that the film has re-crystallised and no longer displays the amorphous Ni layers at the interface between film and vacuum. From the overlaying of the FFT of the surface and the FFT of the bulk like region of the film it is clear the same inter-planar distances are maintained in the two regions. This discounts the notion that the amorphous Ni layer is nickel carbide or has simply crystallised as a nickel metal layer on the surface, meaning that the surface has been re-oxidised into NiO. Of particular note is the surface geometry of the re-crystallised NiO sample with $\{100\}$ facets visible, suggesting the surface is unlikely to be OH terminated. As shown previously, in this chapter and Chapter 5, the faceted (111) surface exposes many interesting sites with enhanced catalytic properties.

### 6.5.2 Environmental XPS

To investigate the re-crystallisation and oxidation of the reduced surface, seen in the TEM images, the sample from Section 6.4.2 was introduced to 0.15mbar of $H_2O$ and studied again with XPS. Fig. 6.7 shows that at room temperature the surface already began to re-oxidise, showing a decrease in the metallic Ni2P$_{3/2}$ peak at 852.3eV as well as a decrease in relative height of the Ni2p$_{1/2}$ peak at 869.6eV. This indicates that the cause of the sample, left in atmosphere overnight, re-crystallising was water vapour. As temperature increases up to 673K the reduced NiO (111) | Nb-STO (111) sample becomes further oxidised. As seen in the faceted termination of the surface in Fig. 6.6, re-oxidation does not appear to form a OH terminated surface as the Ni2p$_{3/2}$ peak retains its multiplicity, where a single peak is characteristic of OH termination.[117] At

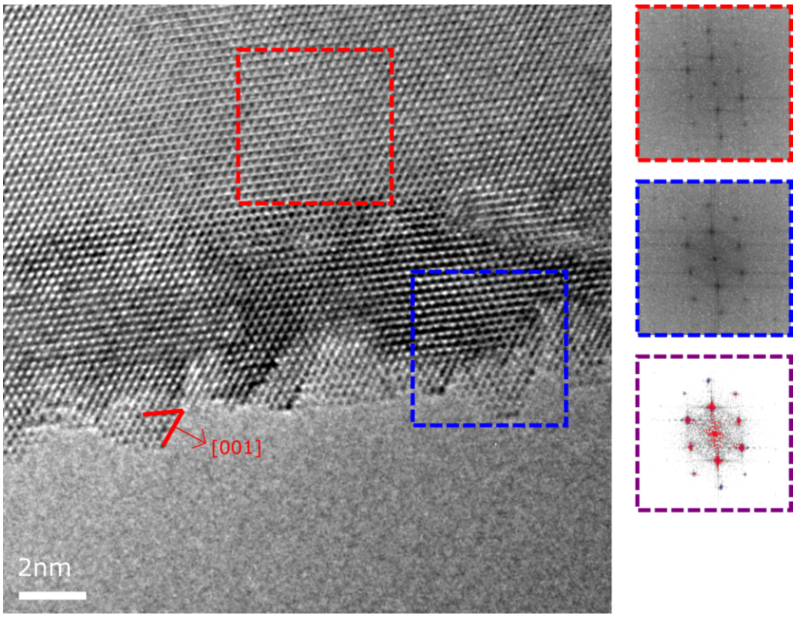

**Figure 6.6:** A TEM image of a NiO (111) | MgO (111) sample that has been re-crystallised via exposure to standard atmosphere. The sample is viewed down the $[1\bar{1}0]$ direction and shows {100} facets on the surface, with the [001] direction marked. Two regions of the film are highlighted, a bulk like area and a section of the reconstructed surface, boxed in red and blue respectively. The diffractogram of these areas are shown in the corresponding images to the side. In the third image to the side a high contrast version of the diffractograms has been produced and the white channel of each has been set transparent whilst the black channel has been changed to the colour of their border. From this it is clear that the separation between planes in each section is identical

773K the sample reduces again and this reduction at high temperature is unusual. One explanation is that residual $H_2$ is not being removed from the chamber and at 773K there is enough energy in the system for the reverse process to occur; the $H_2$ molecules reduce the surface forming $H_2O$.

### 6.5.3 Density Functional Theory

Re-oxidation of a reduced NiO surface was studied from the starting point of the oxygen vacancies discussed in Section 6.4.3. This was chosen instead of a fully reduced surface due to the limitations of the theory to correctly describe the full reduction process. Therefore the structure of the reduced surface is unable to be calculated from first principles and from TEM images shown in Fig. 6.1b and previous Scanning Electron Microscope (SEM) images of CO reduced NiO[102] the surface metallic Ni is shown to be amorphous. The oxygen vacancy surface does however provide information about the energetics behind the oxidation of the surface and as the re-crystallised surface forms {100} facets, as shown in Fig. 6.6, the structure is clearly justified.

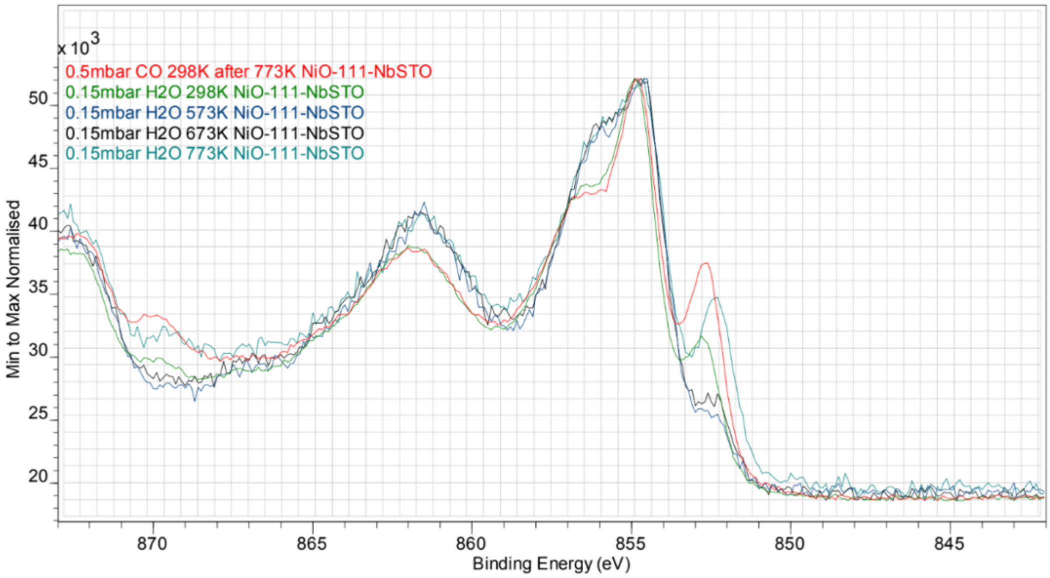

**Figure 6.7:** XPS of the temperature resolved evolution of NiO (111) in a $H_2O$ atmosphere with a 0.15mbar partial pressure. At room temperature the metallic Ni2$p_{3/2}$ peak is decreasing in counts from the fully reduced starting point. The oxidised Ni2$p_{3/2}$ peak retains its multiplicity indicating the sample is not forming OH terminated NiO.

The oxidation energy, $E_{\text{oxidation}}$, for the reaction,

$$\text{Surface}_{\text{Vacancy}} + H_2O \rightarrow \text{Surface} + H_2, \tag{6.6}$$

is given by

$$E_{\text{oxidation}} = E_{\text{surface}} + E_{H_2O} - \left(E_{\text{vacancy}} + E_{H_2}\right). \tag{6.7}$$

The values for the (100) and (111) surfaces are shown in Table 6.2. As expected the reaction is exothermic which is supported by the XPS and TEM data. As the difference between surfaces is related directly to the formation energy of the vacancy it is no surprise to see a reverse in the favourability of this reaction compared to CO induced reduction. Whilst the (100) surface is the most favourable surface for this reaction it is still extremely favourable on the two terminations of the (111) surface. Applying the same pressure, temperature and constant volume constraints as done when calculating $\Delta G$ for the reduction reaction, the reaction enthalpy was calculated for the surfaces with all maintaining a negative reaction enthalpy. This is despite the change

| | (100) | Oxygen Terminated (111) | Ni Terminated (111) |
|---|---|---|---|
| $E_{\text{oxidation}}$ | -1.99 | -1.25 | -1.29 |

**Table 6.2:** The oxidation energies of reduced NiO surfaces. All values are given in electron-volts.

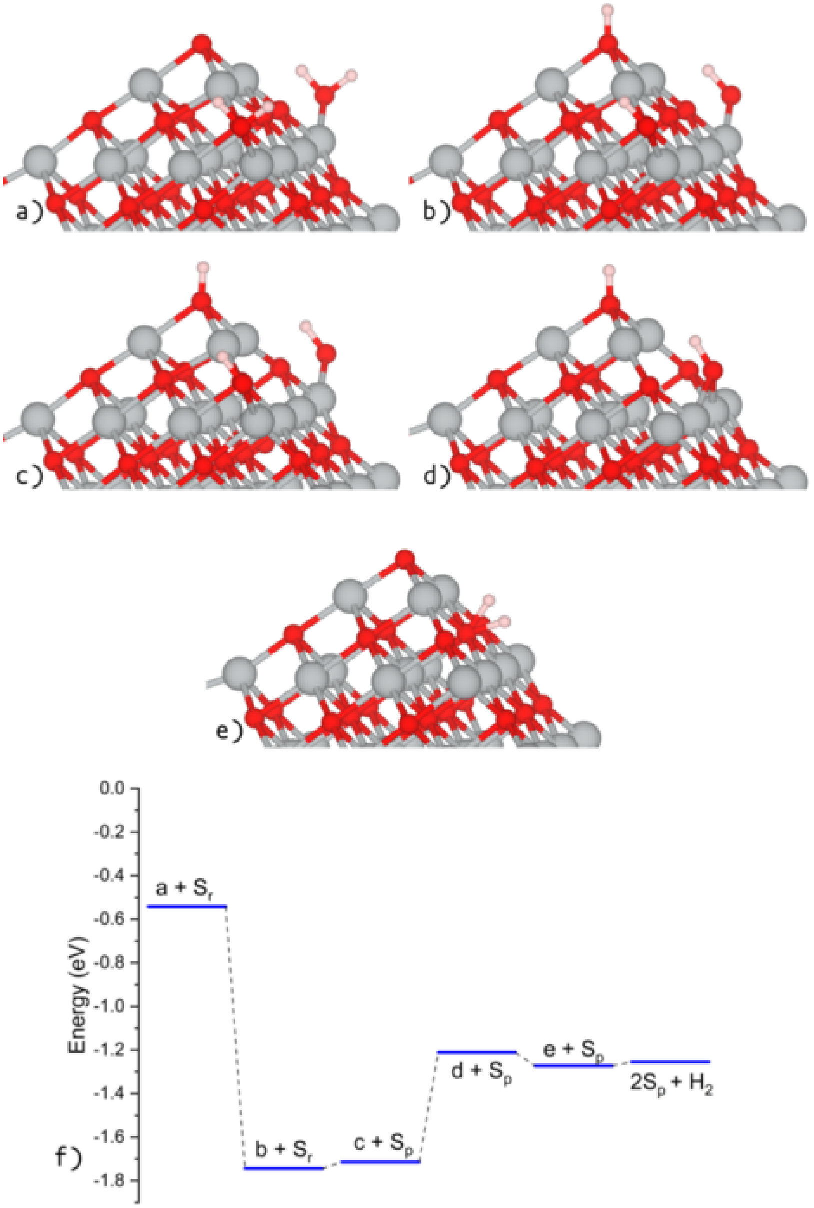

**Figure 6.8:** The geometries of steps within the re-oxidation of the reduced faceted NiO (111) surface. Nickel atoms are shown in grey whilst oxygen and hydrogen atoms are shown in red and pink respectively. The figure labels used to describe the geometries are used in f) to associate each energy level to a structure. The energy scale for f) is zeroed at the energy of a pristine surface, $S_p$, a reduced surface, $S_r$, and an isolated $H_2O$ molecule. Because of this each energy level corresponds to the labelled structure as well as an infinitely separated second surface, allowing for direct comparison between adsorption away from the vacancy and adsorption at the vacancy.

in entropy between $H_2$ and $H_2O$ being negative and divergent, increasing the reaction enthalpy as temperature increases.

Pathways for re-oxidation for the (100) surface were considered by comparing adsorption of $H_2O$ on the reduced surface to that on the pristine. Adsorption of the water molecule around or in the vacancy had positive adsorption energies of 0.01eV and 0.94eV respectively whilst the adsorption energy for the pristine surface was calculated to be -0.52eV. This large difference suggests that the molecule would prefer to adsorb away from the vacancy and have to overcome a large potential barrier to re-position the oxygen in the vacancy. One possible further pathway to oxidise the surface would be through water splitting and then migration of the hydroxide to the vacancy. However water-splitting on the (100) surface is unfavourable with an adsorption energy of 0.89eV with respect to a free $H_2O$ molecule. For the (100) surface, re-oxidising in a $H_2O$ atmosphere therefore faces significant barriers in each pathway.

Re-oxidation on a oxygen terminated (111) surface is not so difficult. Whilst the same obstacles face the adsorption around the oxygen vacancy, once a water molecule is adsorbed on the pristine surface it is able to split and migrate to the vacancy. This dissociative adsorption is known to be the case experimentally with an adsorption energy of -1.77eV[118] matching very closely the value of -1.74eV calculated for the faceted (111) surface. The pathway to re-oxidation, along with energy levels of each step is shown in Fig. 6.8. The energy levels are calculated with respect to a pristine oxygen terminated (111) surface, an oxygen terminated surface with an oxygen vacancy and an isolated $H_2O$ molecule. This assumes that as the adsorbates migrate between pristine and reduced surface they are separated such that they have no interaction with the surface they have left. Doing so allows for the comparison of energies across the entire process without having adjust for the creation of the oxygen vacancy, as the number of atoms is consistent in each step. Compared to the (100) surface the faceted (111) surface requires only 0.50eV to position the hydroxide over the vacancy and from there the step to re-oxidise is exothermic and the resultant hydrogen is very weakly bound to the surface.

The difference in how water molecules favourably and unfavourably split between the two surfaces suggests that re-oxidation, whilst a more favourable reaction on the (100) surface, is likely going to occur at a lower rate on the (100) surface compared to the faceted (111) surface.

## 6.6 Water-Gas Shift Reaction

As it has been shown that the NiO (111) surface is capable of reduction in a CO atmosphere and oxidation in $H_2O$, it is clear that this lends itself favourably as a redox catalyst to the WGSR. By introducing a previously reduced NiO (111) surface to CO and $H_2O$ together in the TEM, both at the same partial pressure as previously stated in

Section 6.4.1, the viability was of NiO as catalyst was studied. Fig. 6.9 shows the surface of the sample crystallising as it is exposed to $H_2O$ meaning that the re-oxidation rate is higher than the reduction. As time advances the sample keeps its crystalline structure however the surface is still evolving. This suggests that the NiO is indeed acting as a catalyst for the WGSR via a redox mechanism as the change in surface structure implies a constant reduction and re-oxidation.

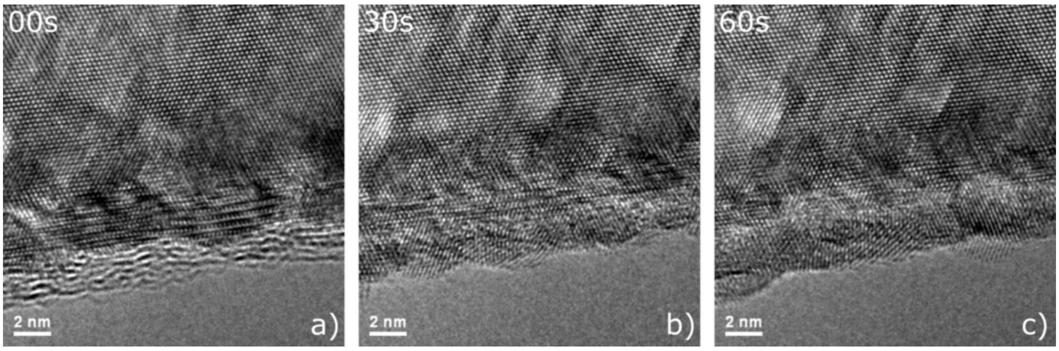

**Figure 6.9:** Evolution of NiO (111) surface in an environmental TEM. Images are snapshots from a video, viewed down the $[1\bar{1}0]$ direction, of a NiO (111) film in an atmosphere of 0.05Pa CO and 0.05Pa $H_2O$. The time intervals show that the surface, starting as amorphous and reduced as visible in a), re-crystallises as it is oxidised by the $H_2O$ shown clearly in b). Once re-crystallised the surface continues evolving, shown by the difference between b) and c), as surface oxygen are continuously removed and replaced.

The surface, as previously mentioned, for the XPS experiments was predicted to be rough with large facets dominating the surface area. As shown by the DFT calculations the reduction in CO is the largest barrier limiting NiO as a catalyst for the WGSR. As the facet size increases, the density of increased catalytic sites reduces and the potential barrier to overcome tends to the same value as for the (100) surface. This could explain the relatively high temperature required to reduce the NiO (111) sample in the XPS experiment whilst the sample viewed in the TEM was able to reduce with only the energy provided by the electron beam. To improve performance and reduce the required temperature a more ordered surface is required. The Gibbs free energy for (100) and (111) surfaces at temperatures of 300K, 400K and 800K are shown in Table 6.3 compounding this as not only do smaller facets increase the density of catalytic sites, the reaction enthalpy is reduced. At 800K, roughly the temperature reduction was observed in the XPS experiment, the reaction enthalpy for the (100) surface is 1.10eV whilst the faceted (111) surface is 0.36eV and 0.40eV for each termination. With the reaction enthalpy for a surface with large facets falling somewhere between these values an octopolar reconstructed surface would a experience similar Gibbs free energy

| | (100) | Faceted (111) | | Octopolar (111) | |
|---|---|---|---|---|---|
| | | O | Ni | O | Ni |
| $\Delta G_{300\mathrm{K}}$ | 1.30 | 0.56 | 0.60 | 0.46 | 0.37 |
| $\Delta G_{400\mathrm{K}}$ | 1.27 | 0.53 | 0.57 | 0.43 | 0.34 |
| $\Delta G_{800\mathrm{K}}$ | 1.10 | 0.36 | 0.40 | 0.26 | 0.17 |

**Table 6.3:** The Gibbs free energy of the WGSR, in electronvolts, for different NiO surfaces. Surfaces with multiple terminations are separated into two columns for oxygen and nickel terminations. The octopolar reconstruction shows very low reaction enthalpies for reduction in CO with and is comparable with the 800K faceted surfaces at temperatures as low as 400K.

between 300K and 400K. This would suggest that a NiO catalyst could promote a low temperature redox WGSR.

## 6.7 Conclusions

This chapter has shown that NiO (111) films are a viable catalyst for the WGSR in the high temperature range and possibly even for a low temperature redox mechanism. Using XPS data to confirm what was seen in an environmental TEM NiO (111) surfaces were shown to reduce in a CO atmosphere at temperatures of less than 773K. The formation of oxygen vacancies on (100) and (111) surfaces have been compared with the asymmetrical distortion on the (111) surface allowing for greater charge redistribution on the surface, leading to lower formation energies. This in turn drastically reduces the barrier to reduction potentially increasing catalytic activity. This reaction was shown to be endothermic, matching the data from the XPS and suggesting that the electron beam was driving the reaction seen in the TEM.

Re-crystallisation of a sample left in an open environment, after being reduced in CO, was captured by TEM images and confirmed by XPS. The sample re-crystallised into a faceted surface rather than OH termination leaving access to the more catalytically active three and four coordinated surface atoms. The pathway to re-oxidation was considered in DFT and it was shown that a vital step was the splitting of the water molecule, which is only possible on the (111) surface. The full re-oxidation process was shown to be exothermic supporting the experimental evidence for room temperature re-oxidation.

Furthermore the full WGSR was seen via environmental TEM to be a redox mechanism with the NiO (111) sample regaining and retaining crystallinity, when equal partial pressures of CO and $H_2O$ where introduced, whilst having an evolving surface. The surface structure is shown to play a large part in the catalytic performance for this reaction with large (100) facets being undesirable and instead smaller reconstructions, providing a greater density of low coordinated sites and better energetics for the reduction reaction, could allow NiO to be used a catalyst for a low temperature redox mechanism.

## CHAPTER 7

# CONCLUSIONS

The study of polar-oxides for heterogeneous catalysis can potentially provide novel new catalysts with active surfaces driven by the polar catastrophe. Within this work, it has been shown that NiO (111) films can be grown epitaxially on MgO (111) substrates via MBE. These films have rough surfaces that can be smoothed via *ex-situ* annealing. The annealing process also removes a second domain that is formed during the growth. The cause of this domain is likely twinning at the interface between substrate and film enhanced by intermixing. Unlike previously reported the interface of $[1\bar{1}0]$ and $[\bar{1}10]$ domains is shown to be along $\{111\}$ planes rather than $\{11\bar{2}\}$ boundaries.

NiO, grown by MBE, has been shown to follow the same faceted reconstruction at the (111) surface as MgO (111), grown via the same method. This suggests that the reconstruction is driven by the polarity of the surface rather than the chemistry of the material. The thesis has shown that the reconstruction heals the divergent surface potential via charge distribution at the surface. This has been confirmed through analysis of the charge density, using Bader volumes to assign density to atoms and then calculating the charge density in the atomic planes involved in the reconstruction. Other rock-salt structured compounds are therefore likely to reconstruct in this manner on the (111) surface. This is already known for halite,[119] for which the octopolar reconstruction was first conceived. However, for other materials with the same structure, the surface reconstructions are not as well studied and are a currently open area of research.[120] For these materials, for example cobalt (II) oxide, our research suggests that the exposure of $\{100\}$ on the (111) surface is a likely termination.

Even in the case where sharply terminated surfaces are produced, the faceted reconstruction can be accessed as shown in the case of the STEM electron beam induced facets presented in Chapter 5. This indicates that atomically sharp surfaces are stabilised via hydroxylation and the energy of the scanning electron beam is able to facilitate the breaking of the OH molecule and reconstruction to the faceted termination. The interaction of observation instrument and sample is obviously a very important relationship and further understanding of this relationship would make for a very interesting project. This thesis has also discussed methods by which to characterise the faceted, reconstructed surface and presented predictions of CO vibrational modes by which to identify the pyramidal reconstruction, which could easily be tested by Infrared-Spectroscopy analysing the surface of grown films.

Finally, it has been shown that when it comes to polar-oxides for heterogeneous catalysis the polarity is not the only factor involved. Whilst the exposure of unsaturated bonds on the surface is shown to provide an easier pathway to reduction and facilitate dissociative water adsorption, the formation enthalpy of the material is also critical. Here NiO excels against MgO, falling between the formation enthalpy for both $CO_2$ and $H_2O$. The significance of this is that both steps of the redox reaction are both exothermic as energy is realised in the reduction of the catalyst in CO and then the oxidation in $H_2O$.

This has been confirmed by the DFT calculations and supported by XPS and environmental-TEM data presented in the thesis. Ni metal layers formed by the reduction process were able to form {100} facets, the stable surface reconstruction presented earlier in the thesis, after re-introduction to open atmosphere. Also images of the surface during exposure to 0.05 Pa $H_2O$ whilst already in a 0.05 Pa CO atmosphere show re-crystallisation of the surface with only the first few layers evolving with respect to time. This, along with no suggestion of carbides in the XPS, suggests that NiO would make a robust catalyst, a feature outlined in Chapter 1 as a strong requirement.

In conclusion polar-oxides provide a viable avenue of research for heterogeneous catalysis due to their inherently low coordinated surfaces. The polarity of the materials has been shown to drive the reconstruction of rock-salt polar-oxides into extended non-polar facets, exposing more active sites with unsaturated bonds. In this thesis it was theorised that these surfaces would drive the performance of catalysts for heterogeneous reactions. This has been shown to be the case for NiO and the WGSR, whereby the polar (111) surface was up to 6 times more favourable than the non-polar (100) surface. The significance of this is that temperatures for operation of robust, non-pyrophoric redox catalysts can be reduced without the need to use rare-earth metals. Instead, just harnessing the potential of polar surfaces can lead to performance enhancement of catalytic materials.

## 7.1 Future Work

The project, in its current state, has many options for continuation as well as multiple directions for future, tangential, projects. Growth of NiO (111) films on MgO (111), or other suitable substrates, can be optimised further, whilst an *in-situ* RHEED study could provide further insight into the formation of the dual $[1\bar{1}0]$ and $[\bar{1}10]$ domains. It would be interesting to see how the intensity of the $[\bar{1}10]$ domain evolves with each atomic layer. This could provide insight into how nucleation of the domain and whether it requires enough layers of NiO deposited for interfacial mixing to occur before it can form.

A Fourier transform infrared spectroscopy study of CO on faceted (111) surfaces of NiO and MgO would also be interesting work that would be able to relate to the work presented in Chapter 5. As well as this new techniques have been developed to study the effect of the electron beam in a TEM on reactions with nanotube catalysts. A study of the dynamics of a NiO (111) surface using similar techniques to calculate the effect of the beam on the surface, perhaps with some form of molecular dynamics study, would be a good project for further understanding the film-beam interaction within electron microscopes.

Further XPS studies of the WGSR with a NiO (111) catalyst would provide good follow up data to that already collected for Chapter 6. In particular XPS data for an atmosphere that was a combination of CO and $H_2O$ would provide greater insight into the performance of NiO (111) as a catalyst for the WGSR. Also, the production, and classification, of octopolar reconstructed NiO (111) films could help reach the potential of NiO as a catalyst for said reaction. A theoretical study of the full reduction process would be very interesting however, NiO suffers greatly from the limitations of the current theory, with functionals that correctly model NiO being unable to capture the properties of Ni metal. However as functionals, like meta-GGAs, with greater performance continue to be produced this becomes more of a possibility.

## APPENDIX A

# BADER CHARGE PARTITIONING

For this appendix a working knowledge of the programming language RUST is assumed. Documentation, as well as the full source code, for the program discussed in this appendix can be found at `https://docs.rs/crate/bader` an open source documentation host for crates of the Rust Programming Language. As the code base is, at the time of writing, 4865 lines long only the important features for multi-threading and the removal of the number of basins dependency of the method presented in Ref. 59 are discussed.

Firstly the adaption of the method to improve scaling with number of Bader charge basins is presented. Voxels are operated on in order of the value of the charge density within them, with the largest values of charge density processed first. A Vec from std::collections is used to store HashMaps, also from std::collections, for each boundary voxel containing the index within the the density array of the basin maxima and weight associated with that maxima. Storing this information at the point the maxima is calculated is the advantage leveraged by this code. As each subsequent voxel only needs the weights of surrounding voxels with a higher charge density to calculate the weights of it's associated maxima the weighting of every voxel can be calculated with just one iteration over the density.

The ability to parallelise the code is complicated by this dependency on the required linear progressing through the ordered density voxels. However the only case in which voxels will be blocked from processing in parallel is when voxels in the current processing pool are within a Voronoi vector of each other. For a cell with a large number of Bader charge basins this is extremely unlikely as voxels of similar charge density will be distributed with a similar symmetry to the crystal structure.

Shown below is a simplified version of the VoxelMap structure to illustrate the locking mechanism for thread-safe concurrency.

```
// A lock guard for write access to
// VoxelMap.weight_map
pub struct Lock<'a> {
    data: &'a VoxelMap,
}
unsafe impl<'a> Sync for Lock<'a> {}
// Deref only exposes the weight_map
// field of a [`VoxelMap`].
impl<'a> Deref for Lock<'a> {
    type Target = Vec<Vec<(usize, f64)>>;
    fn deref(&self) -> &Vec<Vec<(usize, f64)>> {
        unsafe { &*self.data.weight_map.get() }
    }
}
// DerefMut only exposes the weight_map
// field of a [`VoxelMap`].
impl<'a> DerefMut for Lock<'a> {
    fn deref_mut(&mut self) -> &mut Vec<Vec<(usize, f64)>> {
        unsafe { &mut *self.data.weight_map.get() }
    }
}

pub struct VoxelMap {
    weight_map: UnsafeCell<Vec<Vec<(usize, f64)>>>,
    weight_index: Vec<AtomicIsize>,
    lock: AtomicBool,
}
unsafe impl Sync for VoxelMap {}
impl VoxelMap {
    // Stores the index of p's weight
    // contributions in weight_map into the
    // weight_index and unlocks the structure.
    pub fn weight_store(&self, p: isize, i: usize) {
        self.weight_index[p as usize].store(i as isize, Ordering::Relaxed);
        self.lock.store(false, Ordering::SeqCst);
    }
    // Locks the structure for write access.
    pub fn lock(&self) -> Lock {
        while self.lock.swap(true, Ordering::SeqCst) {}
        Lock { data: self }
    }
}
```

Once the lock is acquired the length of the returned vector is recorded and weight HashMap can be pushed to it. As the RUST compiler requires all objects only have a single owner with write access the vector must be stored in an UnsafeCell, however as we control the access through an AtomicBool we still maintain a single writer. Then the lock is released as the length of the vector is stored as the index of the HashMap for the point, p, in the charge density. A simplified example is shown below.

```
// Create a threadsafe counter
let counter = RelaxedCounter::new(0usize)
// iterate over every voxel in the charge density in parallel
(0..reference.len()).into_par_iter().for_each(|_|
{
    // get the next value in the list of
    // voxel indices sorted by charge density
    let p = {
        let i = counter.inc();
        index[i]
    };
    // for the current point get the associated
    // maxia and weights
    let (maxima, weights) = weight_method(p,
                                          &reference,
                                          Arc::clone(&voxel_map));
    // if the weights HashMap is not empty then the
    // point is a boundary and so we store it
    if !weights.is_empty() {
        let i = {
            let mut weight = voxel_map.lock();
            let i = weight.len();
            (*weight).push(weights);
            i
        };
        voxel_map.weight_store(p as isize, i);
    }
    voxel_map.maxima_store(p as isize, maxima);
});
```

## APPENDIX B

# CONVERGENCE TESTING

In this appendix the convergence of several energies, with respect to differing parameters are presented to justify plane-wave cut off, $k$-point sampling and vacuum gap for calculations performed in this thesis. The y-axis of all the figures represents the energy difference of that value compared with the value of the most converged calculation. As a result the final value plotted is always zero. The k-point and planewave convergence is calculated with respect to the number of atoms in the periodic cell where as the converged criteria for the vacuum gap is the surface energy, as described in Eqn. 3.46, and eV / molecule.

As shown in Fig. B.1 with increase in planewave cut-off the energy begins to converge, after 450 eV both NiO and MgO are below $1 \times 10^{-3}$ eV/atom. Likewise with k-points, as shown in Fig. B.2, as the k-point spacing is decreased the energy per atom converges and at a spacing of 0.5 $Å^{-3}$ it is considered converged to 3 meV per atom.

Vacuum gap size was chosen to be the smallest value at which both the surfaces and the adsorbed molecules were also below either 3 meV/$Å^3$ or 3 meV / molecule. The surfaces were incredibly stable with respect to vacuum gap whilst the molecules were more susceptible to variation in vacuum gap. This is shown in Fig. B.3 which is an example of the surfaces and molecule convergence data. At 12 Å both surface and molecule are converged to the required accuracy and as such a 12 Å vacuum gap was decided upon for all work in this thesis. For the surfaces on which molecules were to be adsorbed, Chapters 5 & 6, the vacuum gap was therefore set to 15 Å for the bare surfaces. This allowed for the adsorption of molecules, assuming a bond length of less than 1.5 Å, and upon these bare surfaces the molecules were adsorbed.

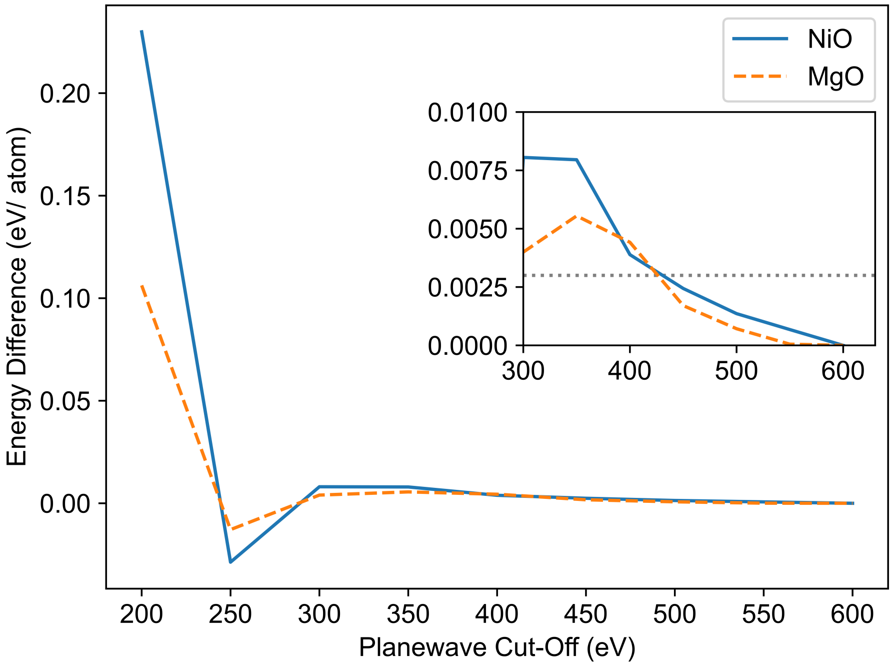

**Figure B.1:** Energy Convergence with respect to planewaves. The dotted grey line represents 3 meV energy difference to the last value. Both NiO and MgO are below this value after 450 eV planewave cut-off.

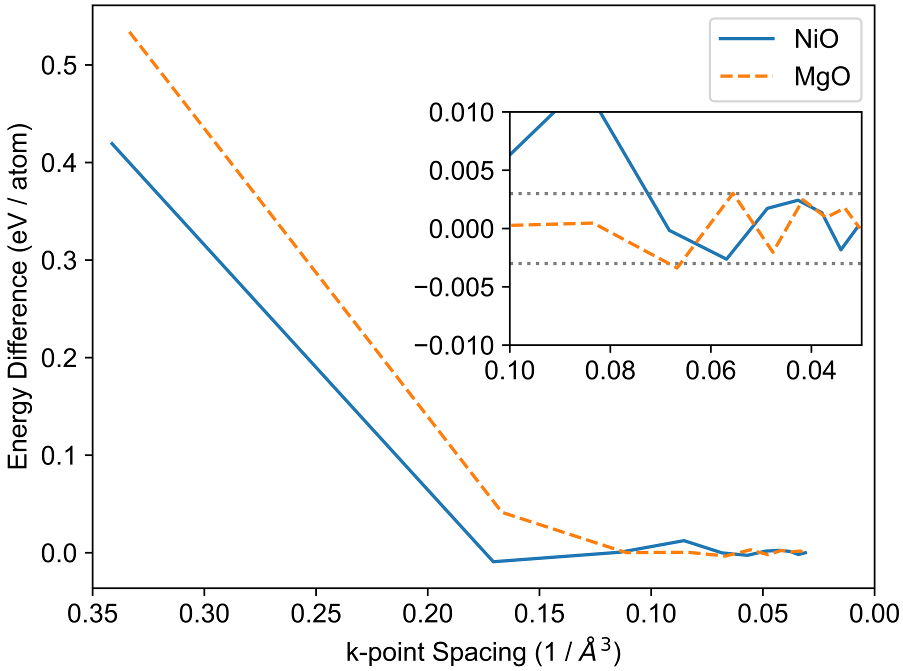

**Figure B.2:** Energy Convergence with respect to k-point spacing. The dotted grey lines represents 3 meV and -3 meV energy difference to the last value. Both NiO and MgO are between this value after a k-point spacing of 0.05 1/Å$^3$.

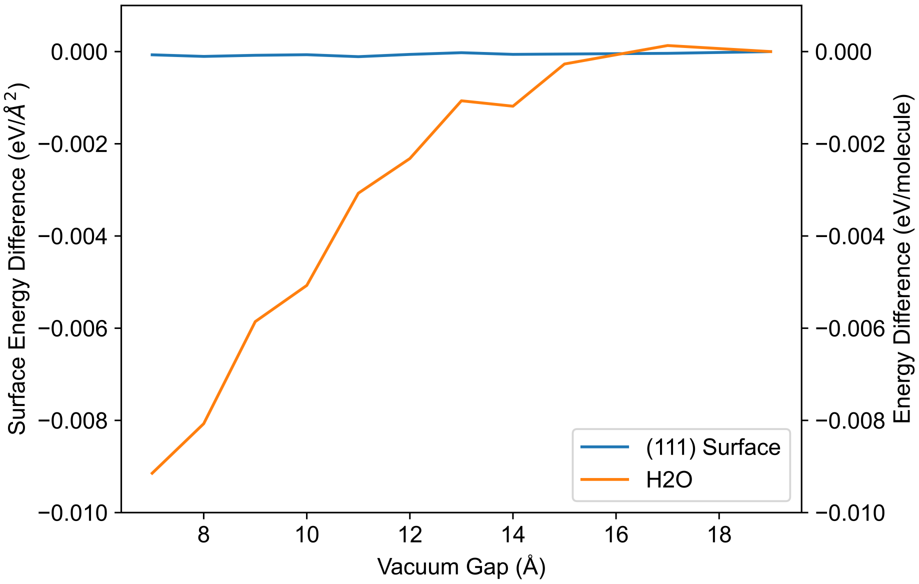

**Figure B.3:** Energy Convergence with respect to vacuum gap for the (111) surface of MgO and an isolated $H_2O$ molecule. $H_2O$ is plotted against the right hand y-axis whilst the (111) surface is plotted against the left. The scale and relative position of them both are the same.

# ABBREVIATIONS

**VASP** Vienna Ab initio Simulation Package.

**ADF** Annular Dark Field.

**AFM** Atomic Force Microscopy.

**BCT** Bader Charge Transfer.

**BF-STEM** Bright Field Scanning Transmission Electron Microscopy.

**BF-TEM** Bright Field Transmission Electron Microscopy.

**CBM** Conduction Band Maximum.

**DF-TEM** Dark Field Transmission Electron Microscopy.

**DFT** Density-Functional Theory.

**DFT+$U$** DFT with a Hubbard-like correction.

**FEL** Fast-Entry Load-Lock.

**FFT** Fast Fourier Transform.

**FIB** Focused Ion Beam.

**GGA** Generalised Gradient Approximation.

**HAADF** High Angle Annular Dark Field.

**HEG** Homogeneous Electron-Gas.

**HRTEM** High Resolution Transmission Electron Microscopy.

**KS** Kohn-Sham.

**LDA** Local Density Approximation.

**LSDA** Local Spin Density Approximation.

**MBE** Molecular Beam Epitaxy.

**MNDO** Modified Neglect of Diatomic Overlap.

**PAW** Projector Augmented Wave.

**PBE** Perdew-Burke-Ernzerhof.

**PDOS** Projected Density of States.

**PEM** Proton-Exchange Membrane.

**PIPS** Precision Ion Polishing System.

**PLD** Pulsed Laser Deposition.

**QCM** Quartz Crystal Microbalance.

**QMC** Quantum Monte-Carlo.

**redox** Reduction-Oxidation.

**RF** Radio Frequency.

**RHEED** Reflection High-Energy Electron Diffraction.

**SAED** Selected Area Electron Diffraction.

**SEM** Scanning Electron Microscope.

**SGGA** Spin Polarised Generalised Gradient Approximation.

**STEM** Scanning Transmission Electron Microscope.

**TEM** Transmission Electron Microscope.

**TISE** Time-Independent Schrödinger Equation.

**TSP** Titanium Sublimation Pump.

**UHV** Ultra High Vacuum.

**VBM** Valence Band Minimum.

**WGSR** Water-Gas Shift Reaction.

**xc** Exchange-Correlation.

**XPS** X-ray photoelectron spectroscopy.

# BIBLIOGRAPHY

[1] C. Noguera, 'Polar oxide surfaces,' *Journal of Physics: Condensed Matter* **12(31)**, R367 (2000)

[2] C. Noguera and J. Goniakowski, 'Polarity in oxide ultrathin films,' *Journal of Physics: Condensed Matter* **20(26)**, 264003 (2008)

[3] L. Nguyen, F. F. Tao, Y. Tang, J. Dou and X.-J. Bao, 'Understanding Catalyst Surfaces during Catalysis through Near Ambient Pressure X-ray Photoelectron Spectroscopy,' *Chemical Reviews* **119(12)**, 6822 (2019)

[4] D. Pingstone, 'Characterisation and growth of polar MgO(111) thin films prepared by Molecular Beam Epitaxy,' Ph.D. thesis, University of York (2019)

[5] P. W. Tasker, 'The stability of ionic crystal surfaces,' *Journal of Physics C: Solid State Physics* **12(22)**, 4977 (1979)

[6] N. W. Ashcroft and N. D. Mermin, *Solid State Physics*, (Cengage Learning1976), ISBN 0030839939

[7] C. A. Cadigan, A. R. Corpuz, F. Lin, C. M. Caskey, K. B. H. Finch, X. Wang and R. M. Richards, 'Nanoscale (111) faceted rock-salt metal oxides in catalysis,' *Catalysis Science & Technology* **3(4)**, 900 (2013)

[8] D. Wolf, 'Reconstruction of nacl surfaces from a dipolar solution to the madelung problem,' *Phys. Rev. Lett.* **68**, 3315 (1992)

[9] J. Ciston, A. Subramanian, D. Kienzle and L. Marks, 'Why the case for clean surfaces does not hold water: Structure and morphology of hydroxylated nickel oxide (111),' *Surface Science* **604(2)**, 155 (2010)

[10] W. Xing, Y. Zhang, J. Zhu and R. Yu, 'Structural and spin state transition in the polar NiO(111) surface,' *Applied Surface Science* **532**, 147427 (2020)

[11] J. Ciston, A. Subramanian and L. Marks, 'Water-driven structural evolution of the polar MgO (111) surface: An integrated experimental and theoretical approach,' *Physical Review B* **79(8)**, 085421 (2009)

[12] V. K. Lazarov, R. Plass, H.-C. Poon, D. K. Saldin, M. Weinert, S. A. Chambers and M. Gajdardziska-Josifovska, 'Structure of the hydrogen-stabilized MgO(111)(1×1) polar surface: Integrated experimental and theoretical studies,' *Physical Review B* **71(11)**, 115434 (2005)

[13] G. M. Uddin, K. S. Ziemer, A. Zeid, Y. T. T. Lee and S. Kamarthi, 'Process control model for growth rate of molecular beam epitaxy of MgO (111) nanoscale thin films on 6H-SiC (0001) substrates,' *International Journal of Advanced Manufacturing Technology* (2017)

[14] K. Refson, R. Wogelius, D. Fraser, M. Payne, M. Lee and V. Milman, 'Water chemisorption and reconstruction of the MgO surface,' *Physical Review B* **52(15)**, 10823 (1995)

[15] C. Ebensperger and B. Meyer, 'First-principles study of the reconstruction and hydroxylation of the polar NiO(111) surface,' *Physica Status Solidi (b)* **248(10)**, 2229 (2011)

[16] N. Kitakatsu, V. Maurice, C. Hinnen and P. Marcus, 'Surface hydroxylation and local structure of NiO thin films formed on Ni(111),' *Surface Science* **407(1-3)**, 36 (1998)

[17] V. Lazarov, Z. Cai, K. Yoshida, K. Zhang, M. Weinert, K. Ziemer and P. Hasnip, 'Dynamically stabilized growth of polar oxides: The case of MgO(111),' *Physical Review Letters* **107**, 056101 (2011)

[18] B. Warot, E. Snoeck, P. Baulès, J. Ousset, M. Casanove, S. Dubourg and J. Bobo, 'Formation of tetrahedral islands in epitaxial NiO layers deposited on MgO(111),' *Journal of Crystal Growth* **234(4)**, 704 (2002)

[19] V. E. Henrich, 'Thermal faceting of (110) and (111) surfaces of MgO,' *Surface Science* **57(1)**, 385 (1976)

[20] H. Onishi, C. Egawa, T. Aruga and Y. Iwasawa, 'Adsorption of na atoms and oxygen-containing molecules on MgO (100) and (111) surfaces,' *Surface Science* **191(3)**, 479 (1987)

[21] R. Plass, J. Feller and M. Gajdardziska-Josifovska, 'Morphology of MgO (111) surfaces: artifacts associated with the faceting of polar oxide surfaces into neutral surfaces,' *Surface science* **414(1-2)**, 26 (1998)

[22] C. Ratnasamy and J. P. Wagner, 'Water Gas Shift Catalysis,' *Catalysis Reviews* **51(3)**, 325 (2009)

[23] T. Thampan, S. Malhotra, J. Zhang and R. Datta, 'Pem fuel cell as a membrane reactor,' *Catalysis Today* **67(1-3)**, 15 (2001)

[24] M.W. Chase Jr., 'NIST-JANAF Themochemical Tables, Fourth Edition,' *Technical report* (1998)

[25] D. B. Pal, R. Chand, S. N. Upadhyay and P. K. Mishra, 'Performance of water gas shift reaction catalysts: A review,' *Renewable and Sustainable Energy Reviews* **93**, 549 (2018)

[26] C. A. Callaghan, 'Kinetics and Catalysis of the Water-Gas-Shift Reaction: A Microkinetic and Graph Theoretic Approach,' *Department of Chemical Engineering* **Ph. D. The**, 400 (2006)

[27] X. Qi and M. Flytzani-Stephanopoulos, 'Activity and Stability of CuCeO2 Catalysts in High-Temperature WaterGas Shift for Fuel-Cell Applications,' *Industrial & Engineering Chemistry Research* **43(12)**, 3055 (2004)

[28] Y. Li, Q. Fu and M. Flytzani-Stephanopoulos, 'Low-temperature water-gas shift reaction over Cu- and Ni-loaded cerium oxide catalysts,' *Applied Catalysis B: Environmental* **27(3)**, 179 (2000)

[29] A. Chambers, *Modern vacuum physics* (2004), ISBN 9780203492406

[30] W. Umrath, 'Fundamentals of vacuum technology,' (2016)

[31] D. B. Williams and C. B. Carter, *Transmission electron microscopy: A textbook for materials science* (2009), ISBN 9780387765006

[32] A. Chew, B. Brewster, I. Olsen and S. Ormrod, 'Improvements in the performance of turbomolecular pumps: Beyond the molecular range,' *Vakuum in Forschung und Praxis* **23(3)**, 14 (2011)

[33] M. Ohring, *Materials Science of Thin Films (Second Edition)*, (Academic Press, San Diego2002), second edition, ISBN 978-0-12-524975-1

[34] G. G. Lister, 'Review Article: Low-Pressure Gas Discharge Modelling,' *Journal of Physics D: Applied Physics* **25(12)**, 1649 (1992)

[35] S. Ino, 'Some new techniques in reflection high energy electron diffraction (rheed) application to surface structure studies,' *Japanese Journal of Applied Physics* **16(6)**, 891 (1977)

[36] P. A. Maksym and J. L. Beeby, 'A theory of rheed,' *Surface Science* **110(2)**, 423 (1981)

[37] P. J. Dobson, B. A. Joyce, J. H. Neave and J. Zhang, 'Current understanding and applications of the RHEED intensity oscillation technique,' *Journal of Crystal Growth* **81(1-4)**, 1 (1987)

[38] C. Davisson and L. H. Germer, 'Diffraction of electrons by a crystal of nickel,' *Physical Review* **30(6)**, 705 (1927)

[39] E. Abbe, 'Beiträge zur Theorie des Mikroskops und der mikroskopischen Wahrnehmung,' *Archiv für Mikroskopische Anatomie* **9(1)**, 413 (1873)

[40] L. De Broglie, 'Recherches sur la théorie des Quanta,' *Annales de Physique* **10(3)**, 22 (1925)

[41] P. D. Nellist, 'Scanning transmission electron microscopy,' in 'Springer Handbooks,' (2019), 49–99

[42] B. Fultz and J. M. Howe, *Transmission electron microscopy and diffractometry of materials* (2008), ISBN 9783540738855

[43] O. L. Krivanek, G. J. Corbin, N. Dellby, B. F. Elston, R. J. Keyse, M. F. Murfitt, C. S. Own, Z. S. Szilagyi and J. W. Woodruff, 'An electron microscope for the aberration-corrected era,' *Ultramicroscopy* **108(3)**, 179 (2008)

[44] J. M. Lebeau, S. D. Findlay, L. J. Allen and S. Stemmer, 'Quantitative atomic resolution scanning transmission electron microscopy,' *Physical Review Letters* **100(20)** (2008)

[45] K. Van Benthem and S. J. Pennycook, 'Imaging and spectroscopy of defects in semiconductors using aberration-corrected STEM,' *Applied Physics A: Materials Science and Processing* **96(1)**, 161 (2009)

[46] E. Meyer, 'Atomic force microscopy,' *Progress in Surface Science* **41(1)**, 3 (1992)

[47] G. K. Binnig, 'Atomic-force microscopy,' *Physica Scripta* **1987(T19A)**, 53 (1987)

[48] I. Newton, *Philosophiæ naturalis principia mathematica*, (Jussu Societatis Regiae ac Typis Josephi Streater. Prostat apud plures bibliopolas1687)

[49] M. J. S. Dewar and W. Thiel, 'Ground states of molecules. 38. The MNDO method. Approximations and parameters,' *Journal of the American Chemical Society* **99(15)**, 4899 (1977)

[50] M. Born and R. Oppenheimer, 'Zur Quantentheorie der Molekeln,' *Annalen der Physik* **389(20)**, 457 (1927)

[51] P. Hohenberg and W. Kohn, 'Inhomogeneous Electron Gas,' *Physical Review* **136(3B)**, B864 (1964)

[52] W. Kohn and L. J. Sham, 'Self-Consistent Equations Including Exchange and Correlation Effects,' *Physical Review* **140(4A)**, A1133 (1965)

[53] J. P. Perdew, K. Burke and M. Ernzerhof, 'Generalized Gradient Approximation Made Simple,' *Physical Review Letters* **77(18)**, 3865 (1996)

[54] P. E. Blöchl, O. Jepsen and O. K. Andersen, 'Improved tetrahedron method for Brillouin-zone integrations,' *Physical Review B* **49(23)**, 16223 (1994)

[55] V. Stevanović, S. Lany, X. Zhang and A. Zunger, 'Correcting density functional theory for accurate predictions of compound enthalpies of formation: Fitted elemental-phase reference energies,' *Physical Review B - Condensed Matter and Materials Physics* **85(11)**, 1 (2012)

[56] S. L. Dudarev, G. A. Botton, S. Y. Savrasov, C. J. Humphreys and A. P. Sutton, 'Electron-energy-loss spectra and the structural stability of nickel oxide: An LSDA+U study,' *Physical Review B* **57(3)**, 1505 (1998)

[57] A. Rohrbach, J. Hafner and G. Kresse, 'Molecular adsorption on the surface of strongly correlated transition-metal oxides: A case study for CO/NiO(100),' *Physical Review B* **69(7)**, 075413 (2004)

[58] R. F. W. Bader, 'Atoms in molecules,' *Accounts of Chemical Research* **18(1)**, 9 (1985)

[59] M. Yu and D. R. Trinkle, 'Accurate and efficient algorithm for Bader charge integration,' *The Journal of Chemical Physics* **134(6)**, 064111 (2011)

[60] A. Kerrigan, 'https://doi.org/10.5281/zenodo.4409397,' (2021)

[61] G. Kresse and D. Joubert, 'From ultrasoft pseudopotentials to the projector augmented-wave method,' *Physical Review B* **59(3)**, 1758 (1999)

[62] P. Güttinger, 'Das Verhalten von Atomen im magnetischen Drehfeld,' *Zeitschrift für Physik* **73(3-4)**, 169 (1932)

[63] W. Pauli, 'Principles of wave mechanics,' *Handbuch der Physik* **24**, 162 (1933)

[64] H. Hellmann, 'Einfuhrung in die quantenchemie (leipzig: Deuieke) feynman rp 1939,' *Phys. Rev* **56**, 340 (1937)

[65] R. P. Feynman, 'Forces in Molecules,' *Physical Review* **56(4)**, 340 (1939)

[66] W. H. Press, B. P. Flannery, S. A. Teukolsky, W. T. Vetterling and H. Gould, 'Numerical Recipes, The Art of Scientific Computing,' *American Journal of Physics* **55(1)**, 90 (1987)

[67] P. Pulay, 'Convergence acceleration of iterative sequences. the case of scf iteration,' *Chemical Physics Letters* **73(2)**, 393 (1980)

[68] K. C. Wang, J. Y. Jeng, P. S. Shen, Y. C. Chang, E. W. G. Diau, C. H. Tsai, T. Y. Chao, H. C. Hsu, P. Y. Lin, P. Chen, T. F. Guo and T. C. Wen, 'P-type mesoscopic nickel oxide/organometallic perovskite heterojunction solar cells,' *Scientific Reports* **4(1)**, 1 (2014)

[69] José A. Rodriguez, *, Jonathan C. Hanson, Anatoly I. Frenkel, , Jae Y. Kim and M. Pérez§, 'Experimental and Theoretical Studies on the Reaction of H2 with NiO: Role of O Vacancies and Mechanism for Oxide Reduction,' (2001)

[70] M. Xu, S. Yao, D. Rao, Y. Niu, N. Liu, M. Peng, P. Zhai, Y. Man, L. Zheng, B. Wang, B. Zhang, D. Ma and M. Wei, 'Insights into Interfacial Synergistic

Catalysis over Ni@TiO$_{2-x}$ Catalyst toward Water–Gas Shift Reaction,' *Journal of the American Chemical Society* **140(36)**, 11241 (2018)

[71] J. Feng, Y. Ding, Y. Guo, X. Li and W. Li, 'Calcination temperature effect on the adsorption and hydrogenated dissociation of CO2 over the NiO/MgO catalyst,' *Fuel* **109**, 110 (2013)

[72] N. C. Nelson, M.-T. Nguyen, V.-A. Glezakou, R. Rousseau and J. Szanyi, 'Carboxyl intermediate formation via an in situ-generated metastable active site during water-gas shift catalysis,' *Nature Catalysis* **2(10)**, 916 (2019)

[73] J. Hu, K. Zhu, L. Chen, H. Yang, Z. Li, A. Suchopar and R. Richards, 'Preparation and Surface Activity of Single-Crystalline NiO(111) Nanosheets with Hexagonal Holes: A Semiconductor Nanospanner,' *Advanced Materials* **20(2)**, 267 (2008)

[74] X. Cai, X. Wang, X. Guo and C. guang Zheng, 'Mechanism study of reaction between CO and NiO(001) surface during chemical-looping combustion: Role of oxygen,' *Chemical Engineering Journal* **244**, 464 (2014)

[75] J. J. Carey and K. P. McKenna, 'Does Polaronic Self-Trapping Occur at Anatase TiO2 Surfaces?' *The Journal of Physical Chemistry C* **122(48)**, 27540 (2018)

[76] G. Kresse and J. Furthmüller, 'Efficient iterative schemes for ab initio total-energy calculations using a plane-wave basis set,' *Physical Review B* **54(16)**, 11169 (1996)

[77] P. Stadelmann, 'EMS - a software package for electron diffraction analysis and HREM image simulation in materials science,' *Ultramicroscopy* **21(2)**, 131 (1987)

[78] T. Kawamura, M. Hasebe and P. Dobson, 'The origin of circular arc in rheed: 1d ordered surface,' *Journal of The Physical Society of Japan - J PHYS SOC JPN* **54**, 3675 (1985)

[79] J. Scherer, B. M. Ocko and O. M. Magnussen, 'Structure, dissolution, and passivation of Ni(111) electrodes in sulfuric acid solution: An in situ STM, X-ray scattering, and electrochemical study,' *Electrochimica Acta* **48(9 SPEC.)**, 1169 (2003)

[80] P. Kovesi, 'Good colour maps: How to design them,' (2015)

[81] M. Budde, C. Tschammer, P. Franz, J. Feldl, M. Ramsteiner, R. Goldhahn, M. Feneberg, N. Barsan, A. Oprea and O. Bierwagen, 'Structural, optical, and

electrical properties of unintentionally doped NiO layers grown on MgO by plasma-assisted molecular beam epitaxy,' *Journal of Applied Physics* **123(19)**, 195301 (2018)

[82] M. Budde, T. Remmele, C. Tschammer, J. Feldl, P. Franz, J. Lähnemann, Z. Cheng, M. Hanke, M. Ramsteiner, M. Albrecht and O. Bierwagen, 'Plasma-assisted molecular beam epitaxy of NiO on GaN(00.1),' *Journal of Applied Physics* **127**, 15306 (2020)

[83] K. Matsuzaki, V. K. Lazarov, L. Lari, H. Hosono and T. Susaki, 'Fe3O4(111) thin films with bulk-like properties: Growth and atomic characterization,' *Journal of Physics D: Applied Physics* **46(2)** (2013)

[84] S. Lany, J. Osorio-Guillén and A. Zunger, 'Origins of the doping asymmetry in oxides: Hole doping in NiO versus electron doping in zno,' *Phys. Rev. B* **75**, 241203 (2007)

[85] G. Trimarchi, Z. Wang and A. Zunger, 'Polymorphous band structure model of gapping in the antiferromagnetic and paramagnetic phases of the mott insulators mno, feo, coo, and NiO,' *Phys. Rev. B* **97**, 035107 (2018)

[86] G. A. Sawatzky and J. W. Allen, 'Magnitude and origin of the band gap in NiO,' *Phys. Rev. Lett.* **53**, 2339 (1984)

[87] J. Khler, 'Transition metal oxides. an introduction to their electronic structure and properties.(reihe: International series of monographs on chemistry, vol. 27.) von pa cox. oxford university press, oxford, 1992. ix, 284 s., geb. 37.50£. isbn 0-19-855570-9,' *Angewandte Chemie* **105(3)**, 477 (1993)

[88] A. K. Cheetham and D. A. O. Hope, 'Magnetic ordering and exchange effects in the antiferromagnetic solid solutions $mn_x ni_{1-x}O$,' *Phys. Rev. B* **27**, 6964 (1983)

[89] B. Fender, A. Jacobson and F. Wedgwood, 'Covalency parameters in mno, $\alpha$-mns, and NiO,' *The Journal of Chemical Physics* **48(3)**, 990 (1968)

[90] F. Birch, 'Finite Elastic Strain of Cubic Crystals,' *Physical Review* **71(11)**, 809 (1947)

[91] F. Wang, Y. Xu, X. Liu, Y. Liu, J. Liu and B. Teng, 'Pinpointing the active sites and reaction mechanism of co oxidation on NiO,' *Phys. Chem. Chem. Phys.* **21**, 17852 (2019)

[92] J. A. Quirk, V. K. Lazarov and K. P. McKenna, 'Electronic properties of 112 and 110 twin boundaries in anatase tio2,' *Advanced Theory and Simulations* **2(12)**, 1900157 (2019)

[93] D. Cappus, J. Klinkmann, H. Kuhlenbeck and H.-J. Freund, 'CO on NiO(100): orientation and bonding,' *Surface Science* **325(3)**, L421 (1995)

[94] S. M. Vesecky, X. Xu and D. W. Goodman, 'Infrared study of CO on NiO(100),' *Journal of Vacuum Science & Technology A: Vacuum, Surfaces, and Films* **12(4)**, 2114 (1994)

[95] Z. Dohnálek, G. A. Kimmel, S. A. Joyce, P. Ayotte, R. S. Smith and B. D. Kay, 'Physisorption of co on the MgO(100) surface,' *The Journal of Physical Chemistry B* **105(18)**, 3747 (2001)

[96] H. Jian-Wei, C. A. Estrada, J. S. Corneille, W. Ming-Cheng and D. Wayne Goodman, 'Co adsorption on ultrathin MgO films grown on a mo(100) surface: an iras study,' *Surface Science* **261(1)**, 164 (1992)

[97] B. Liu, M. Wang, S. Liu, H. Zheng and H. Yang, 'The sensing reaction on the ni-NiO (111) surface at atomic and molecule level and migration of electron,' *Sensors and Actuators B: Chemical* **273**, 794 (2018)

[98] H. Raebiger, S. Lany and A. Zunger, 'Charge self-regulation upon changing the oxidation state of transition metals in insulators,' *Nature* **453(7196)**, 763 (2008)

[99] M. Schönnenbeck, D. Cappus, J. Klinkmann, H. J. Freund, L. G. Petterson and P. S. Bagus, 'Adsorption of CO and NO on NiO and CoO: A comparison,' *Surface Science* **347(3)**, 337 (1996)

[100] C. Xu and D. Goodman, 'Structure sensitivity of oxide surfaces: the adsorption and reaction of carbon monoxide and formic acid on NiO(100) and NiO(111),' *Catalysis Today* **28(4)**, 297 (1996)

[101] G. Peng, L. R. Merte, J. Knudsen, R. T. Vang, E. Lægsgaard, F. Besenbacher and M. Mavrikakis, 'On the Mechanism of Low-Temperature CO Oxidation on Ni ( 111 ) and NiO ( 111 ) Surfaces,' **(111)**, 21579 (2010)

[102] J. Chen and P. C. Hayes, 'Mechanisms and Kinetics of Reduction of Solid NiO in CO/CO2 and CO/Ar Gas Mixtures,' *Metallurgical and Materials Transactions B: Process Metallurgy and Materials Processing Science* (2019)

[103] D. Cappus, C. Xu, D. Ehrlich, B. Dillmann, C. A. Ventrice, K. Al Shamery, H. Kuhlenbeck and H. J. Freund, 'Hydroxyl groups on oxide surfaces: NiO(100), NiO(111) and Cr2O3(111),' *Chemical Physics* **177(2)**, 533 (1993)

[104] P. A. Crozier and T. W. Hansen, 'In situ and operando transmission electron microscopy of catalytic materials,' *MRS Bulletin* **40(1)**, 38 (2015)

[105] T. C. Lee, D. K. Dewald, J. A. Eades, I. M. Robertson and H. K. Birnbaum, 'An environmental cell transmission electron microscope,' *Review of Scientific Instruments* **62(6)**, 1438 (1991)

[106] P. L. Gai and E. D. Boyes, 'Environmental High Resolution Electron Microscopy in Materials Science,' in 'In-Situ Microscopy in Materials Research,' , (Springer US, Boston, MA1997), 123–147

[107] R. Sharma and K. Weiss, 'Development of a TEM to study in situ structural and chemical changes at an atomic level during gas-solid interactions at elevated temperatures,' *Microscopy Research and Technique* **42(4)**, 270 (1998)

[108] J. T. Richardson, R. Scates and M. V. Twigg, 'X-ray diffraction study of nickel oxide reduction by hydrogen,' *Applied Catalysis A: General* **246(1)**, 137 (2003)

[109] W. L. Masterton, E.J. Slowinski, *Chemical Principles*, (Saunders College Publishing1983), ISBN 10: 0030626463

[110] A. Mansour, 'Characterization of NiO by xps,' *Surface Science Spectra* **3(3)**, 231 (1994)

[111] L.-S. Hsu and R. S. Williams, 'Electronic-structure study of the ni ga and the ni in intermetallic compounds using x-ray photoemission spectroscopy,' *Journal of Physics and Chemistry of Solids* **55(4)**, 305 (1994)

[112] R. Furstenau, G. McDougall and M. Langell, 'Initial stages of hydrogen reduction of NiO (100),' *Surface science* **150(1)**, 55 (1985)

[113] P. Weightman, 'X-ray-excited auger and photoelectron spectroscopy,' *Reports on Progress in Physics* **45(7)**, 753 (1982)

[114] A. M. Ferrari, C. Pisani, F. Cinquini, L. Giordano and G. Pacchioni, 'Cationic and anionic vacancies on the NiO(100) surface: DFT+U and hybrid functional density functional theory calculations,' *Journal of Chemical Physics* **127(17)** (2007)

[115] Q. Xu, S. Cheah and Y. Zhao, 'Initial reduction of the NiO(100) surface in hydrogen,' *The Journal of Chemical Physics* **139(2)**, 24704 (2013)

[116] S. Park, H. S. Ahn, C. K. Lee, H. Kim, H. Jin, H. S. Lee, S. Seo, J. Yu and S. Han, 'Interaction and ordering of vacancy defects in NiO,' *Physical Review B - Condensed Matter and Materials Physics* **77(13)**, 1 (2008)

[117] M. A. Peck and M. A. Langell, 'Comparison of Nanoscaled and Bulk NiO Structural and Environmental Characteristics by XRD, XAFS, and XPS,' *Chemistry of Materials* **24(23)**, 4483 (2012)

[118] W. Zhao, M. Bajdich, S. Carey, A. Vojvodic, J. K. Nørskov and C. T. Campbell, 'Water Dissociative Adsorption on NiO(111): Energetics and Structure of the Hydroxylated Surface,' *ACS Catalysis* **6(11)**, 7377 (2016)

[119] K. Saiki, A. Goda and A. Koma, 'Growth of Polar NaCl(111) Surface on GaAs(111) Substrates,' *Japanese Journal of Applied Physics* **36(Part 2, No. 1A/B)**, L55 (1997)

[120] N. Ma, H. Xie, T. Yang, C. Shi, D. Zhao, C. He, E. Liu and N. Zhao, 'Surface reconstruction of CoO (111) and its effects on the formation of oxygen vacancy and OER activity,' *Surface Science* **711** (2021)